Steering of Thermoplastic Composite Tapes using Hot Gas Torch-assisted Automated Fiber Placement

Aadhithya Rajasekaran

A Thesis in
The department
of
Mechanical, Industrial and Aerospace Engineering

Presented in the Partial Fulfillment of the
Requirements for the Degree of Master of Applied Science (Mechanical Engineering)
at Concordia University
Montreal, Quebec, Canada

November 2022

©Aadhithya Rajasekaran, 2022

CONCORDIA UNIVERSITY

SCHOOL OF GRADUATE STUDIES

This is to certify that the thesis

Prepared by: Aadhithya Rajasekaran

Entitled: Steering of Thermoplastic Composite Tapes using Hot Gas Torch-assisted Automated Fiber Placement

and submitted in the partial fulfillment of the requirements of the degree

Master of Applied Science (Mechanical Engineering)

complies with the regulations of the University and meets the accepted standards with respect to originality and quality.
Signed by the final Examining Committee:

_____ Chair
Dr. Rajamohan Ganesan

_____ Examiner
Dr. Rajamohan Ganesan

_____ Examiner
Dr. Pantcho P. Stoyanov

_____ Supervisor
Dr. Farjad Shadmehri

Approved by _____
Dr. Martin D. Pugh
Chair, Department of Mechanical, Industrial and Aerospace Engineering

_____
Dr. Amir Asif
Dean, Gina Cody School of Engineering and Computer Science

Date: 24/11/2022

Abstract

Steering of Thermoplastic Composite Tapes using Hot Gas Torch-assisted Automated Fiber Placement

Aadhithya Rajasekaran

In-situ manufacturing of thermoplastic composites using Hot Gas Torch (HGT)-assisted Automated Fiber Placement (AFP) has the potential to produce laminates in an efficient manner by avoiding a secondary process, like autoclave consolidation. One of the advantages of HGT-assisted AFP technique is its capability to steer fiber path and to manufacture Variable Angle Tow (VAT) laminates which have shown to have improved mechanical performance. This study investigates the process parameters that affect steering of carbon fiber reinforced thermoplastic tapes (AS4/polyether ether ketone (PEEK)) using a HGT-assisted AFP machine. The effect of the steering radius, laydown speed, number of repasses and substrate angle on the geometry and bond strength of steered tape was investigated through observation and testing. Through geometrical analysis, it was found that with a decrease in the steering radius of the tape there was a decrease in the tape width and an increase in the tape thickness. A significant reduction in the steering induced defects was observed at higher laydown speeds where the defects were intermittent unlike in the case of lower laydown speeds. Performing a repass over the steered tape smoothed some of the tape defects caused by steering. Currently there is no standard method for testing the bond strength of the steered in-situ consolidated composite tapes with its substrate. Hence, a novel mechanical test, inspired by the lap shear test, was devised and used to study the bond strength between the steered tape and the substrate and the results were compared with autoclave treated samples which served

as a reference. Furthermore, the bond strengths of the steered tapes were found to be functions of the laydown speed and substrate angle.

This work also analytically predicts the onset of fiber buckling in the steered tapes to serve as a first approximation or a rule of thumb to understand from which radius fiber buckling can be expected. Timoshenko's *Bar on an elastic foundation* forms the basis for the analytical model, where the bar represents the fiber and the elastic foundation the matrix. Various models that were derived from this idea were studied, and the analytical models that were similar to current problem of fiber buckling were adopted. These analytical models considered a plane stress approach to model the fiber buckling observed during the bending of Elastic Memory Composites (EMC). The steering a of CF/PEEK tape using a HGT-assisted AFP is essentially the bending of a plane (the tape) by external moments, which causes the fibers along the inner-edge of the tape to buckle under compression. The analytical prediction of the critical steering radius showed a good correlation with the experimental observations.

Acknowledgements

First of all, I would like to thank my supervisor Dr. Farjad Shadmehri for his support and guidance throughout my thesis. I would have never accomplished this thesis without his calm mentorship and support.

I would like to thank Dr. Daniel Iosif Rosca and Minh Duc Hoang for always being available to assist in conducting my experimental trials. The time and assistance they provided, even during the pandemic, was instrumental for my thesis.

I would also like to thank all my fellow CONCOM graduate and PhD candidates for their friendship and support. Discussing our individual topics and problems helped me gain clarity in my own.

Most of all, I would like to express my unending gratitude to my family. My parents, without their countless sacrifices, none of this would have been possible. My sister Aparna and my brother-in-law Venkatesh, who opened their home to me and supported me throughout my study. My sister Aarthi and brother-in-law Ram, whose guidance helped me through difficult times. Thank you.

Dedication

To my family.

List of Publications

Journal Paper:

1. Steering of carbon fiber/PEEK tapes using Hot Gas Torch-assisted automated fiber placement. Rajasekaran, A. & Shadmehri, F. Journal of Thermoplastic Composite Materials (2022) doi:https://doi.org/10.1177/08927057211067962.

Conference Paper:

1. Modified Lap Shear Test for Automated Fiber Placement (AFP) of Steered Thermoplastic Composite Tape. Rajasekaran, A. & Shadmehri, F. Proceedings of the American Society for Composites — Thirty-fifth Technical Conference, 2020.

Contents

List of Figures

List of Tables

Chapter 1

Introduction

1.1 Background

Carbon fiber composite materials have been widely adopted in industries like, aerospace, automobile, ship building *etc.* In particular, the aerospace industry has seen an exponential increase in the use of composite materials over the past few decades. As evidence of this, the recent Boeing 787 aircraft uses over 50% composite materials by weight (See Figure 1.1)[1]. This increase in the use of composites is because of its high strength-to-weight ratio and its natural resistance against corrosion [2]. The high strength-to-weight ratio of composites is because of the high anisotropy provided by the fibers. This allows engineers to strengthen components only in the direction they experience the maximum stress without adding much material in the other directions. Fibers are excellent at this role, they perform extremely well under tension and can also resist compression very well with help of the matrix which prevents it from buckling.

However, the same anisotropic nature of the fibers also results in the complex coupling of the stresses and strains [3]. Such a coupling between normal and shear stresses with normal and shear strains is unique to composite materials and very different from how isotropic materials behave. While this elastic coupling can be predicted mathematically, it is difficult to get a intuitive understanding of how a composite material would respond different types of loads. To avoid such coupling effects, most of the initially designed

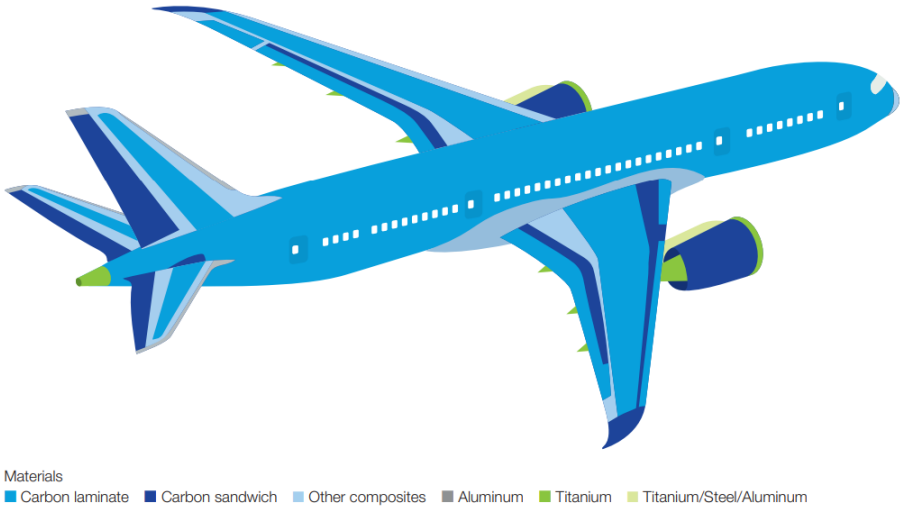

Figure 1.1: Use of composite material in the Boeing 787 [1]

laminates were made to be quasi-isotropic in nature by restricting the fiber angles to 0°, 90° and ±45°. With a better understanding of the mechanical behaviour of composite materials, symmetric and balanced laminates with angles like ±30°, ±60° and even ±55°, in the case of pressure vessels, began to be used.

Such conservative designs did not fully utilize the ability of the carbon fibers, which can be placed even along a curved path and not just at certain angles [4]. For example, holes for fasteners on plate is an area of stress concentration that often leads to crack initiation under stress. Carbon fiber composites can theoretically be used to remove such stress concentrations by being steered along the radius of the hole. Figure 1.2 illustrates such a theoretical optimization of the fiber angles for a hole under tension by Setoodeh *et al.*, using the cellular automata technique [4]. However, despite such avenues for optimization, conservative designs were still widely used because traditional manufacturing techniques, like hand layup, were not conducive to placing fibers along a curve. Furthermore, compared to their isotropic metal counterparts, composites still provided a better strength-to-weight ratio.

With the advent of new automated manufacturing techniques *viz.*, Automated Fiber Placement (AFP), Automated Tape Laying (ATL), Dry Fiber Placement (DFP)and Continuous Tow Shearing (CTS), engineers now have the ability to steer the carbon fiber composite tapes along the required path. Such laminates in which the fibers are laid

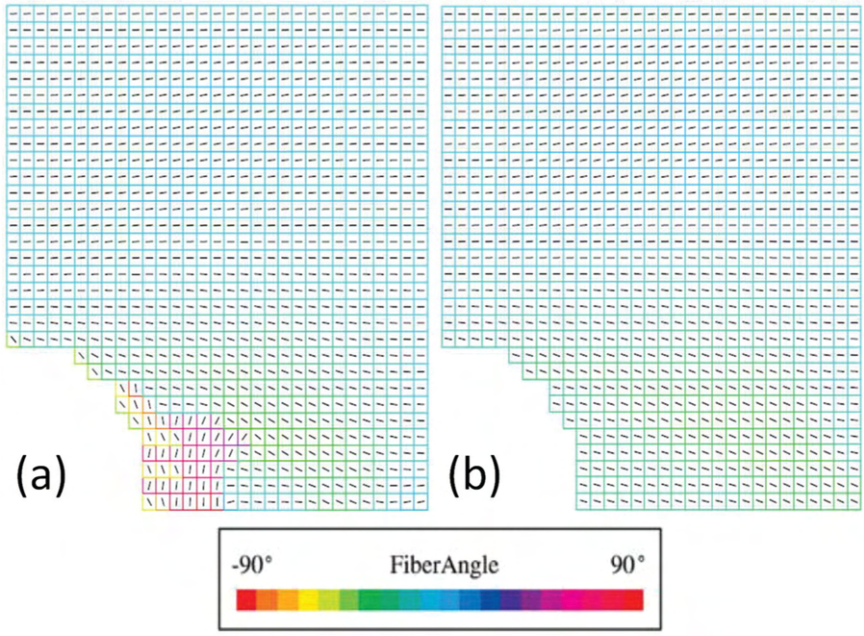

Figure 1.2: Optimum Fiber Angle distribution of a hole in tension

down on curved path are called Variable Angle Tow (VAT) laminates. Apart from being able to reduce stress concentrations VAT laminates have several other advantages. Studies that were performed on the use of VATs have reported improved in-plane stiffness, buckling performance, first-ply failure and bending performance [5–7]. However, there are some inherent defects associated with manufacturing of VAT laminates including tow buckling, tow folding, gaps, overlaps *etc.*, which mainly affect adversely the mechanical performance of these laminates [5, 8, 9].

1.2 Motivation

Thermoset prepreg fiber placement is most widely used to produce VAT laminates. The steering radius of these tapes are restricted due to the resin/matrix of the prepreg tape confining the fibers and preventing it from following the guide curve without any buckling or stretching [8, 10]. The ability of thermoset composite tapes to produce VAT laminates and the influence of defects on part performances have been explored extensively in several studies [5–8, 11–14]. However, the thermoset fiber placement process is not in-situ, *i.e.*, the curing of the resin does not take place simultaneously as the tape is laid down but requires an energy and time consuming secondary process of curing in an autoclave. In

comparison to thermoset fiber placement, the number of studies on the production of VAT laminates using in-situ consolidation of thermoplastic prepreg tapes are very limited [9, 15, 16].

Aiming to fill this gap in literature, the overall objective of this thesis is defined as follows,

To investigate the ability of the Hot Gas Torch-assisted Automated Fiber Placement process to steer Carbon Fiber/PEEK composite prepreg tapes, and analytically predict the onset of fiber buckling.

The objective is of two parts, an experimental investigation and an analytical prediction. The first part of the objective is achieved by studying the effect of the steering radius, laydown speed and re-consolidation pass (referred to as "repass" in the thesis) on the dimensional variation of the steered tape and the bond consolidation of the steered tape. Furthermore, a novel mechanical test was proposed and used to study the effect of steering radius, laydown speed and substrate angle on the bond strength of the steered tape. The second part of the objective is achieved by adopting analytical models that were developed to model fiber buckling in Elastic Memory Composites (EMC), and using them to predict the critical steering radius at which fiber buckling occurs and its wavelength.

1.3 Thesis Outline

This thesis report has been divided into several chapters and have been structured as follows. First, in Chapter 2, a literature review on the topics related to this thesis has been presented. In this, an overview of fundamentals such as the, difference between thermoset and thermoplastic polymers, and the working of various automated composite manufacturing techniques, has been given. Following that, the various studies that have investigated VAT laminates and the their manufacturing have been outlined.

In Chapter 3, the experiments performed to study the ability of the HGT-assisted AFP to steer CF/PEEK tapes have been detailed. First, the initial trials performed to choose some initial parameters like HGT temperature, gas flow rate and consolidation pressure

have been described. Following that, the steps involved sample evaluation techniques *viz.*, geometrical analysis, optical microscopy and mechanical testing, are explained. For the mechanical testing, a new modified lap shear test was devised, and its method has been presented in detail. Then, the results of these evaluations have been presented.

In Chapter 4, the analytical derivations based on Timoshenko's Bar on an Elastic Foundation has been shown [17]. Following that, the results of the analytical derivations have been adopted and applied to the current problem of fiber buckling. The critical steering radius and wavelength have been calculated and presented.

In Chapter 5, the conclusion of the thesis along with, the improvements that can be made, and the future work that can be performed on this topic have been discussed. After Chapter 5, the referees cited in this thesis have been listed. Finally, the appendix containing the computer code used to perform the analytical calculations has been shown.

Chapter 2

Literature Review

In this chapter, a detailed literature review has been presented on the topics related to fiber steering. In Section 2.1, the nature of thermoset and thermoplastic polymers has been explained. Following that, in Section 2.2 the various automated composite manufacturing processes have been discussed and in Section 2.2.1 the working of Hot Gas Torch-assisted Automated Fiber Placement process has been explained in detail. In Section 2.3, the various studies on the manufacturing of Variable Angle Tow (VAT) laminates using AFP processes have been presented. Following that, in Section 2.4 the difficulties encountered in various studies while performing fiber steering due to steering induced defects has been presented. In Section 2.5, the studies performed on fiber steering of thermoplastic composites using in-situ consolidation have been reviewed and presented. Furthermore, the knowledge gap in this topic is highlighted and how this work aims to help fill said gap has been stated in this section. In Section 2.6, the various standard tests available to measure the bond strength of Fiber Reinforced Plastics (FRP) have been explored and the need for new test to measure the bond strength between a steered tape and its substrate has been highlighted. Finally, in the conclusion (Section 2.7), salient points of this detailed literature review have been summarized.

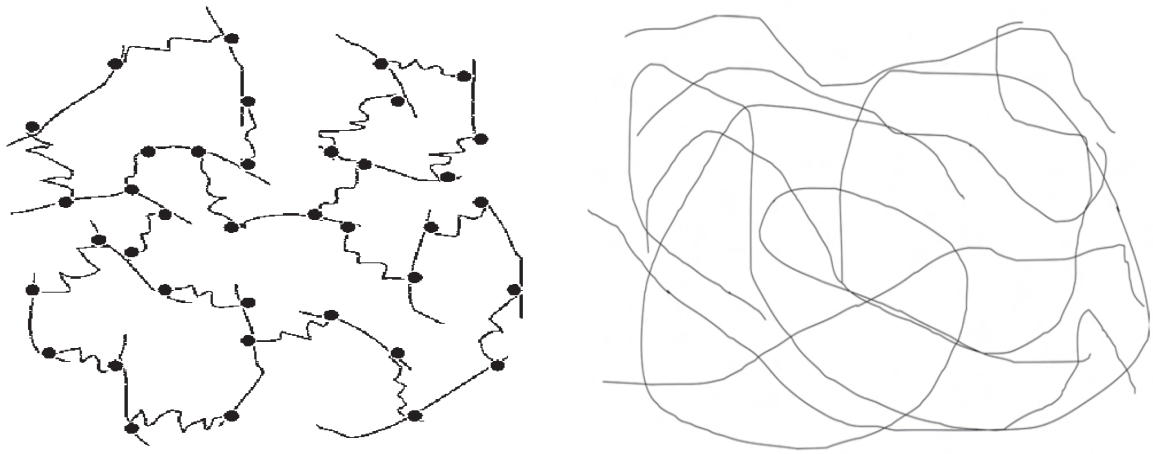

(a) Curing agent linking thermoset polymer chains (b) Long thermoplastic polymer chains

Figure 2.1: Thermoset and thermoplastic polymer schematic[18]

2.1 Thermoplastic and Thermoset Polymers

Thermoset polymers are characterized by having short carbon-carbon (C-C) links, around 20-30 C-C links in the case of epoxy. Due to these short carbon chains they are generally in liquid form at room temperatures and have a low viscosity. This low viscosity is the key advantage of thermoset polymers, as it allows them to be pumped and introduced to the fibers easily [18]. However, since thermoset polymers are in liquid state at room temperature they require a curing agent to bond the short polymer chains together and make them solid. To become solid, millions of such links are required and this process takes hours, even days in some cases, and is usually performed in a vacuum to avoid any unwanted reactions with air. This curing process significantly adds time and complexity to the manufacturing process of thermoset polymer composites. Figure 2.1 shows a schematic of thermoset polymer molecules linked together by a curing agent.

In contrast, thermoplastic polymers like PEEK have very long (several hundreds or thousands) C-C links. This prevents them from moving freely, hence, they are generally solids at room temperature and have a very high viscosity even at high temperatures. On the other hand, they solidify rapidly when cooled, thus, reducing the processing time to the order of seconds. It is this characteristic of thermoplastic polymers, like PEEK, that allows them to be consolidated in-situ. Other advantages of thermoplastic over thermoset are that they can be reheated and reshaped to repair defects or even

be recycled completely, they have extremely long shelf lives and composites made using thermoplastics have a higher fracture toughness.

2.2 Automated Fiber/Tape Placement

Automated composite manufacturing is an additive manufacturing techniques in which composite prepreg tapes are used as material. The laminates are manufactured by a robotic arm which adding the prepreg composite tapes tow-by-tow to form a layer and repeats this process to build the complete laminate. The techniques used to perform automated composite manufacturing can be classified into two types, *viz.*, Automated Fiber Placement(AFP) and Automated Tape Layup(ATL). There are several variations in the AFP and ATL processes but all of them have some common key components,

1. Robotic arm or Gantry
2. Tape placement head
    (a) Tape or fiber feeding system
    (b) Consolidation roller
    (c) Heating System
    (d) Tape cutter
3. Control software

Figure 2.2 shows the common components used in AFP and ATL processes. In general, a tape placement head is mounted on to a robotic arm so that it can be moved along the required path to perform the tape laydown. A spool of prepreg tape or dry fibers is fed under controlled tension to the tape placement head at the required rate which depends on the speed at which the tape laydown is performed. As the tape is fed the backing tape is removed, and the tape is adhered on to the mould or substrate via the tackiness of the tape in case of thermoset composite tape or in-situ consolidation in case of Thermoplastic composite tape(See Section 2.2.1). This adhesion is performed uniformly by applying

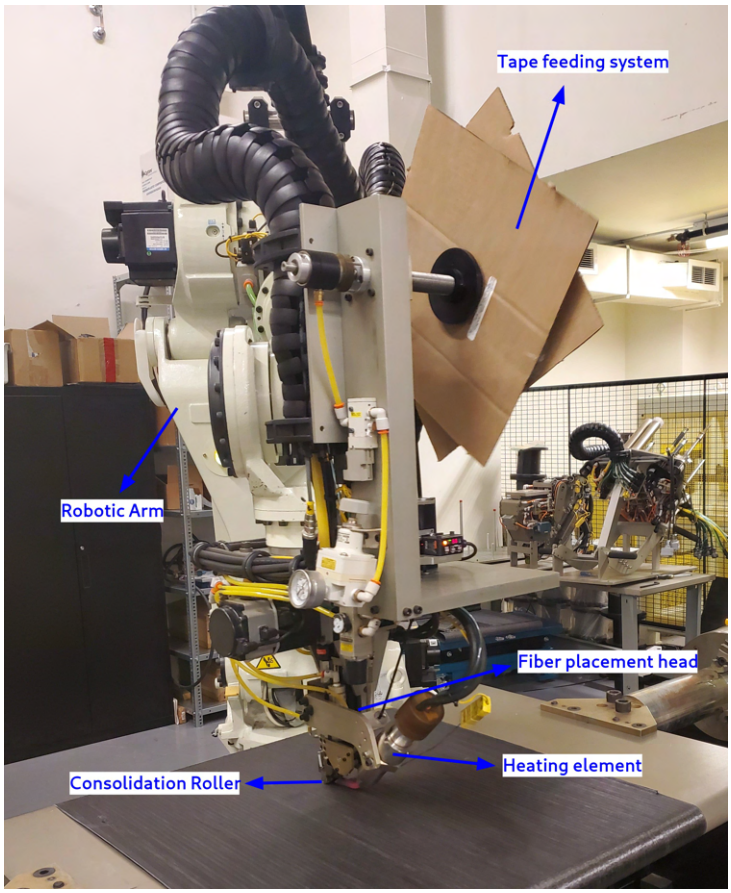

Figure 2.2: Key components of AFP and ATL processes

Figure 2.3: Automated Tape Layup (Photo credit: mtorres) [19]

heat and pressure using a heating element and consolidation roller. The consolidation roller can be of different sizes and materials as required by the specific application. The heating element helps to bond the tack well to the mould or substrate. In case of in-situ consolidation, the heating element is replaced with a high energy heat source like a Hot Gas Torch (HGT) or Laser. Once the robot has completed laying down the tape along the defined path, the tape is then cut before moving to the next path. The control software helps the operator to configure all the process parameters, *viz.*, temperature, consolidation pressure, laydown speed *etc.* They also allow the operator to define the fiber angles of the different layers or even a specific path the robot head should trace. Figures 2.2, 2.3 show a laminate being manufactured using the AFP and ATL processes. Both ATL and AFP processes can be used with thermoset and thermoplastic composites. The difference between the ATL and AFP process is in the width of the tapes used. In the ATL process, the tape widths ranging from 75 to 300mm are used [19]. However in the AFP process, the conventional tape widths used are 3.2, 6.4 and 12.7mm respectively [20]. These are much smaller compared to the tape widths used in the ATL process. The choice between ATL and AFP process comes down to the complexity of the part to be manufactured. While the ATL process is more time efficient by using larger tapes, it can only be used for a limited number of very simple shapes. Furthermore, both thermoset and thermoplastic composites used in the ATL process are finally cured or melted in the autoclave after the layup process. However, in the AFP process, thermoplastic composite tapes can be consolidated in-situ using a high-enery heat source.

2.2.1 Hot Gas Torch-assisted Automated Fiber Placement

The HGT-assisted AFP process is an in-situ manufacturing process where a thermoplastic composite tape is consolidated on to a substrate as the tape is being laid down. Figure 2.4 shows this process close-up with labels for the components used to perform this process. Thermoplastic composite prepreg tapes like, Carbon Fiber(AS4)/PEEK, are used as the feed material in this process. The tapes are stored in spools on top of the fiber placement head as shown in Figure 2.2. This tape is then fed under a controlled tension to the

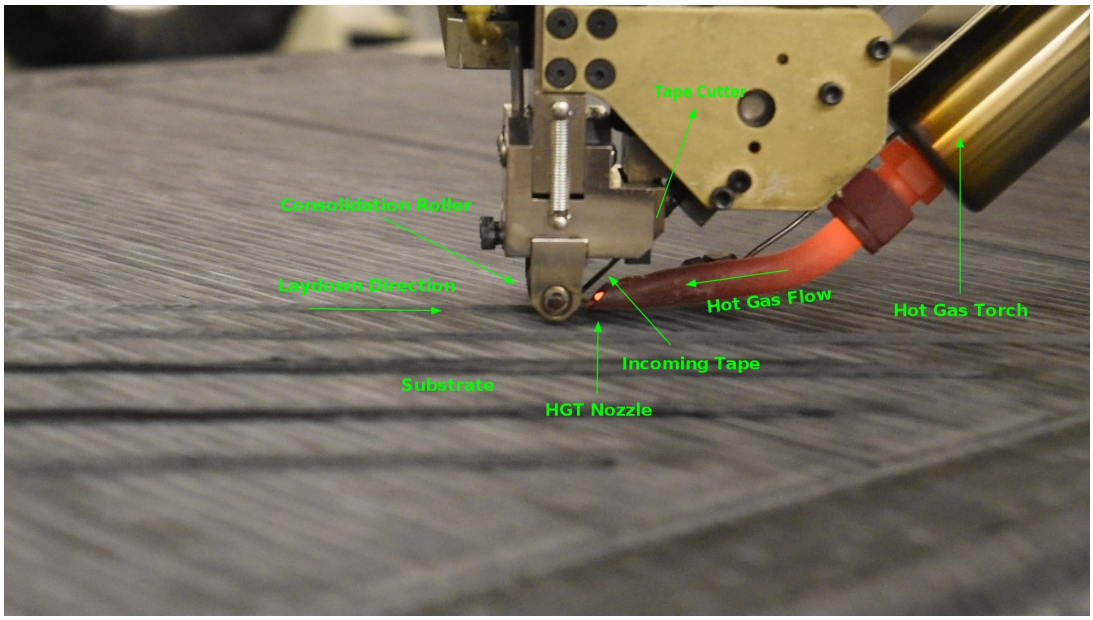

Figure 2.4: Hot Gas Torch AFP process

fiber placement head using a servo motor. There are sensors to ensure the tape is being continuously fed to the fiber placement head and to detect any splices in the tape. The robot is stopped if the spool runs out or if any splice in the tape is found, to prevent the head from tracing the path without laying down any material. As the tape goes through the fiber placement head it passes through the cutter before going to the hot gas torch and consolidation roller. This allows the robot to automatically cut the tape once the end of the defined path is near before proceeding to the next.

Advanced thermoplastic composites have high melting points and viscosity in general. For example, PEEK has a melting point of $343°C$ and viscosity of $1000Pa.s$ @ $400°C$. To reach such high temperatures in a very short time, the gas is pumped from a cylinder and sent to the torch where it is heated up to temperatures ranging from $750°C$ to $950°C$. The HGT uses nitrogen gas since it is fairly inert at high temperatures, thus, preventing oxidative degradation [21, 22]. The hot gas then flows through a nozzle at the required flow rate and impinges directly on the prepreg tape from a very close distance to melt the thermoplastic resin (See Figure 2.4). The melted tape is then consolidated on to the substrate by applying pressure pneumatically through a steel consolidation roller at the nip point. A high temperature with adequate consolidation pressure is essential to form a good bond for two main reasons. First, to develop good intimate contact with the

substrate and prevent the fibers from springing back or pulling up after the rollers passes [23, 24]. Second, to reduce the amount of void formations that can occur in between two layers [23, 24].

The control software for HGT AFP allows the operator to specify all the required process parameters *viz.*, HGT flow rate, HGT temperature, laydown speed and consolidation force. For simple laminates software also allows operator to directly define the number of layers of the laminate and the fiber angles for each layer. For more complex shapes, the user can define the required guide curves and boundaries using a CAD software like Solidworks. The Solidworks model is then imported to the software and the laminate is defined in the form of tows for the AFP robot to manufacture it. This head assembly of tape feed, HGT and consolidation roller, is moved by the robot arm along the paths defined by the control software to build and consolidate the required laminate tape by tape.

2.3 Variable Angle Tow (VAT) Laminates

An important aspect of AFP and ATL processes is their ability to steer the fibers along the required path and manufacture Variable Angle Tow laminates (VAT). This allows engineers to design laminates that are tailored to the specific stress field experienced by an object. Such a design was not always possible with the traditional fiber angle approach. Variable Angle Tow laminates are used to streamline the stiffness of a component as by placing fibers along the direction of maximum stress [4–7]. A simple example of this is the use of VAT laminates to reduce the stress concentration around the hole in a panel, which was explored in a study by Setoodeh *et al.*, [4](See Chapter 1). A similar optimization was also explored by IJsselmuiden [25] in his thesis where he used a three step approach to determine the fiber paths needed to reduce the stress concentrations around a hole (See Figure 2.5). A study performed by Gürdal *et al.*, [5] investigated the effect of VAT laminates on the in-plane stiffness and the buckling response of the laminate. They found that unlike simple angle-ply laminates, either the buckling load

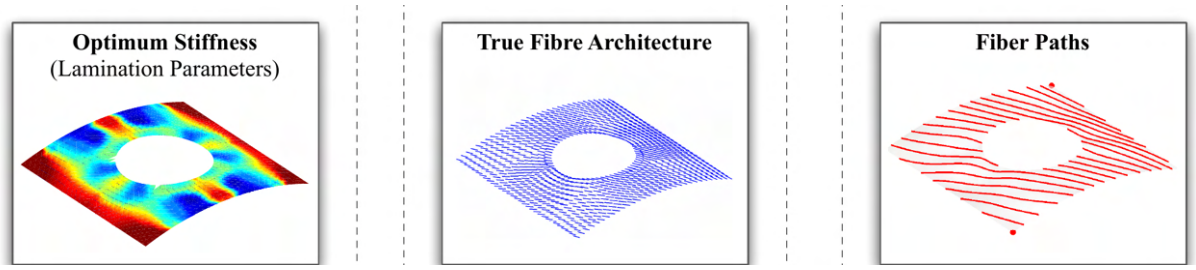

Figure 2.5: Optimizing the fiber paths around a hole [25]

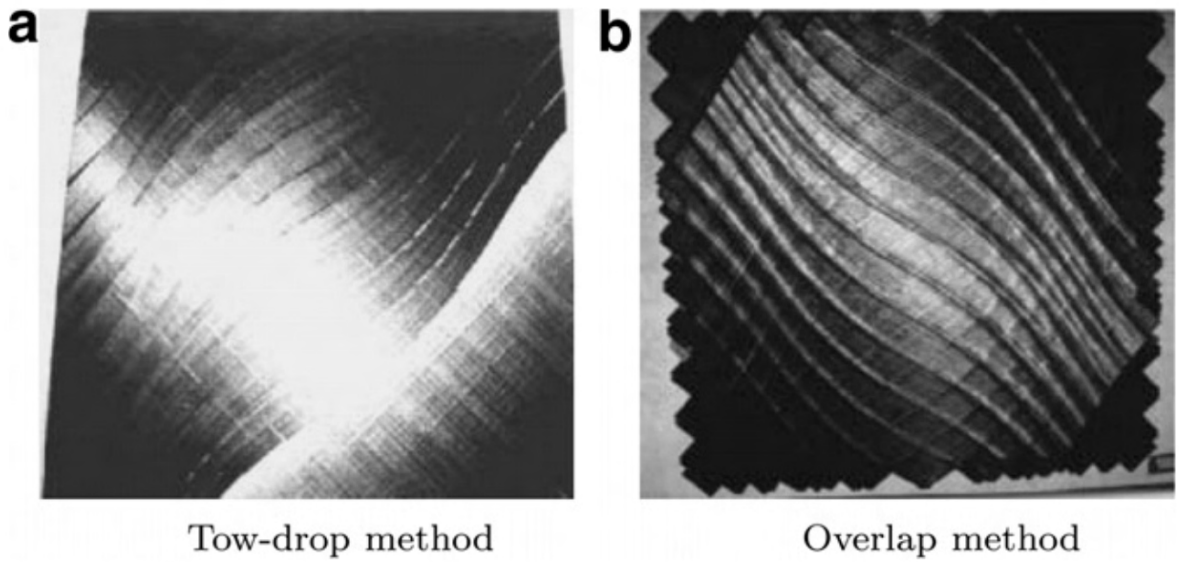

Figure 2.6: Two types of steered VAT laminates [6]

or in-plane stiffness of a VAT laminate can be increased without adversely affecting the other property [5]. This study demonstrated the flexibility available to a designer when using VAT laminates to tailor the laminate for high plane stiffness or buckling load as per their requirement. Such theoretical optimizations can now be realized using automated fiber placement techniques.

Several studies have been performed to test whether VAT laminates improves mechanical performance when compared to traditional fiber angle laminates. A study performed by Lopes *et al.*, explored the improvements in first ply failure of a VAT laminate under compressive load [6]. They performed an FEA analysis using ABAQUS for VAT laminates designed using two different techniques *viz.*, two drop and tow overlaps (See Figure 2.6) and compared it to laminates made using straight fibers. They found that, under compression, the first ply failure in the two-drop method was improved by 24.8% and a remarkable 33.9% in the case of tow-overlap [6]. Laminates with $\pm 45^{\circ}$ plies perform bet-

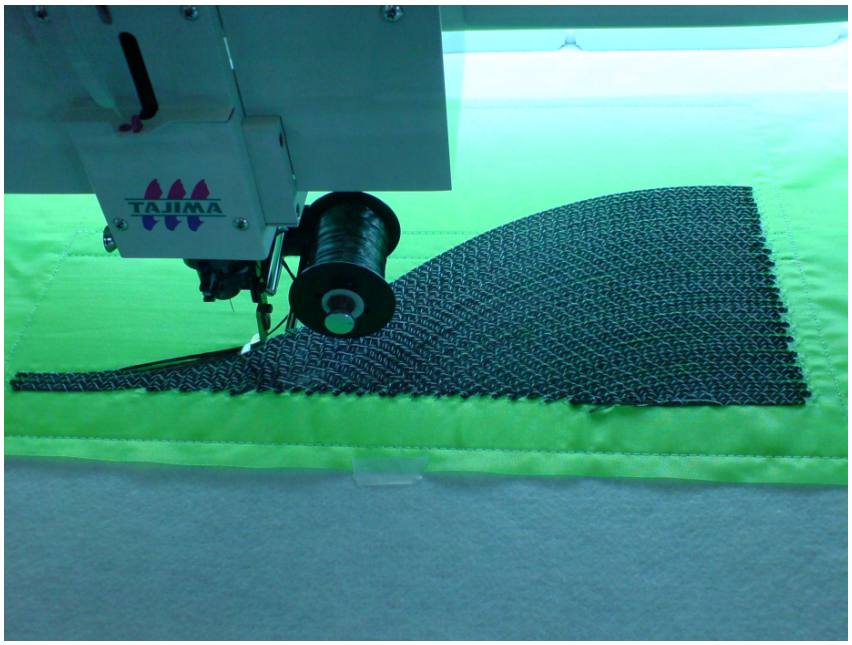

Figure 2.7: Dry fiber placement using stitching[26]

ter when it comes to initial buckling loads in comparison with 0°/90° cross-ply laminates. However, cross-ply laminates perform better after buckling with high post buckling loads. To improve this, Weaver *et al.*, tried using fiber steering to combine the advantages of both ±45° and 0°&90° plies and creating a laminate that has both high initial buckling and post buckling loads [26]. A stitching type dry fiber placement machine was used to steer the fibers by Weaver *et al.*, [26] which were then infused with resin and cured in an autoclave. After performing mechanical tests and an FEA analaysis, they found that the ratio of post-buckled to pre-buckled stiffness of the VAT laminate was 0.92, which was much higher when compared to a ratio of 0.72 for a quasi-isotropic laminate. A thesis by Blom *et al.*, [10] explored the use of VAT laminates to improve the fundamental frequency of conical and cylindrical shells. An AFP process with thermoset prepreg was used by Blom *et al.*, [10] to manufacture the VAT laminates. The use of a tailored VAT laminate increased the fundamental frequency of conical and cylindrical shells by 30% in comparison with a baseline quasi-isotropic laminate. The buckling performance of cylindrical shells was also explored by Blom *et al.*, [10] in this thesis and there was an 18% increase in the buckling load for the VAT laminate compared to the baseline laminate. Another study performed by Rouhi *et al.*, [7] also showed that a cylinder produced by steering

the fibers can improve the bending-induced buckling performance by up to 18%. Overall, these studies show the VAT laminates deliver on the promise of a more optimized laminate without an increase in weight. However, there are also several challenges that are faced during the manufacturing of VAT laminates due to several process induced defects *viz.*, tow buckling, tow folding, gaps and overlaps. These defects have discussed in detail in Section 2.4.

2.4 Fiber Steering Induced Defects

Fiber steering has several inherent defects which primarily stem from trying place a straight rectangular prepreg composite tape along a curved path. The way the defects manifests can change between processes but the type of defects are common across different manufacturing processes. The commonly encountered defects during fiber steering are,

- Tape/Fiber Buckling
- Tape folding
- Gaps
- Overlaps

Tape/Fiber buckling occurs due to the bending of a flat rectangular tape along a curved path. The bending causes compression along the inner edge of the tape due to which, beyond a certain critical radius, the tape buckles. The way this buckling manifests depends on the manufacturing technique used to steer the composite tape. In the case of thermoset AFP, the tapes buckle out-of-plane, while in thermoplastic in-situ AFP the fiber buckling occurs in-plane. Fiber buckling can cause the laminate to lose some of its stiffness since the load carrying fibers have buckled [8, 10]. The mechanism of tape/fiber buckling has been explained in Chapter 4. Tape folding is another defect that is caused by the bending of the rectangular tape along a curved path. This occurs at a much smaller steering radii, where the outer edge of the tape folds over itself because of the excessive

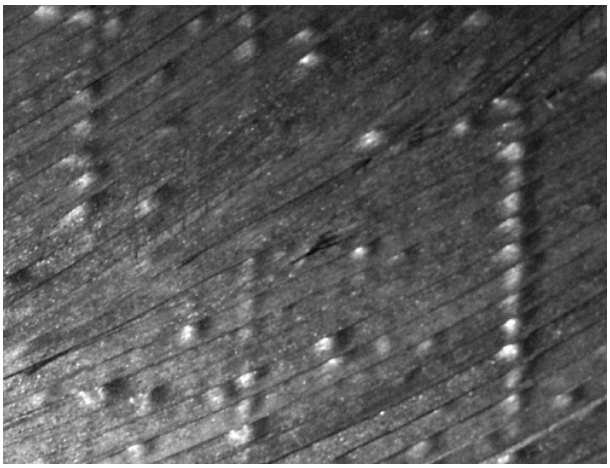

Figure 2.8: Tape buckling of steered thermoset prepreg [10]

tension it experiences [9]. This results in poor bonding between lamina, and can act as a point for crack initiation or delamination. Gaps and overlaps occur when laminates are constructed using fiber steering. While the robot head can accurately trace the curved path the prepreg tapes cannot. This results in gaps and overlaps between adjacent tapes when a laminate is built. Gaps are a source of resin rich areas, and overlaps result in laminates with inconsistent thickness [6].

The studies discussed in Section 2.3 experienced some or all of these defects [6, 7, 10]. A notable exception to this was the study by Weaver *et al.*, [26] where they used a stitching type dry fiber placement. The defects of gaps and overlaps was observed by Lopes *et al.*, [6] when fabricating a rectangular laminate plate using fiber steering. In their study, two laminates were designed using both, gaps and overlaps, and compared with each other (See Figure 2.6). The laminate designed with overlaps showed better performance with respect to first ply failure under compression. In the study by Blom *et al.*, [10] the defect of tape buckling was encountered by them when thermoset tapes were steered using automated fiber placement to create conical and cylindrical shells, as shown in Figure 2.8. Another study by Wu *et al.*, [8] studied the design and manufacturing of VAT laminates for a cylindrical shell with continuously varying fiber angles. Defects such as tape tape buckling, gaps and overlaps were also encountered by Wu *et al.*, [8] in their study. The effect of gaps and overlaps on the buckling performance of rectangular VAT laminates under compression was studied by Marouene *et al.*, [11]. They found

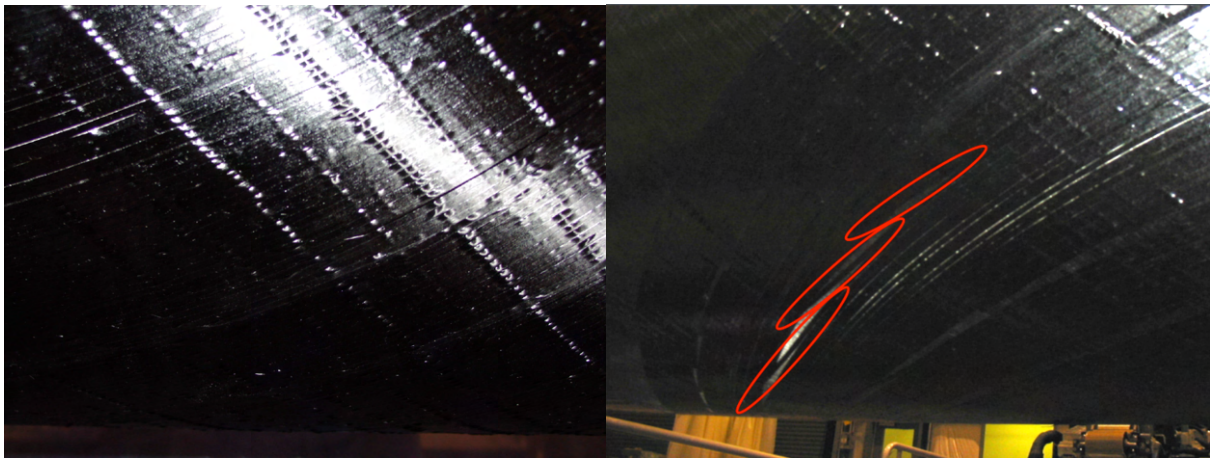

(a) Tape buckling (b) Gaps duing fiber steering

Figure 2.9: Defects during fiber steering [8]

that the panel with complete overlaps had 40% more pre-buckling stiffness and 69% more post buckling stiffness when compared to the VAT panel with gaps. It should also be noted that both the panel with gaps and the one with overlaps performed better that the baseline quasi-isotropic panel [11]. Bakshi *et al.*, studied the steering induced defects of a thermoset AFP process and the process parameters that affect it [27]. They found that the temperature and compaction force have a large effect on the formation of defects in steered thermoset tape. By increasing the temperature and compaction force to $250^{\circ}C$ and $222.4N$ respectively, they were able to achieve a higher level of intimate contact and steer a $6.35mm$ wide thermoset tape up to $889mm$ without defects [14]. This is an improvement when compared to the $1778mm$ steering radius reported by Blom *et al.*, for a $6.35mm$ wide tape [10]. Bakshi *et al.*, also observed that the out-of-plane buckling of thermoset tapes is time dependent and can grow worse after a few seconds [27]. Apart from the most common out-of-plane buckling, Bakshi *et al.*, also observed defects such as blisters, fiber shearing, in-plane buckling, and tow pull up, as show in Figure 2.10.

Apart from AFP using thermoset prepreg, there are other automated methods of manufacturing thermoset VAT laminates *viz.*, Filament winding, Dry Fiber Placement and Continuous Tow Shearing(CTS). Filament winding a type of dry fiber placement can be used to produce variable angle laminates, but it is usually restricted to closed shapes such as pipes and pressure vessels[28]. Dry Fiber Placement(DFP) avoids the

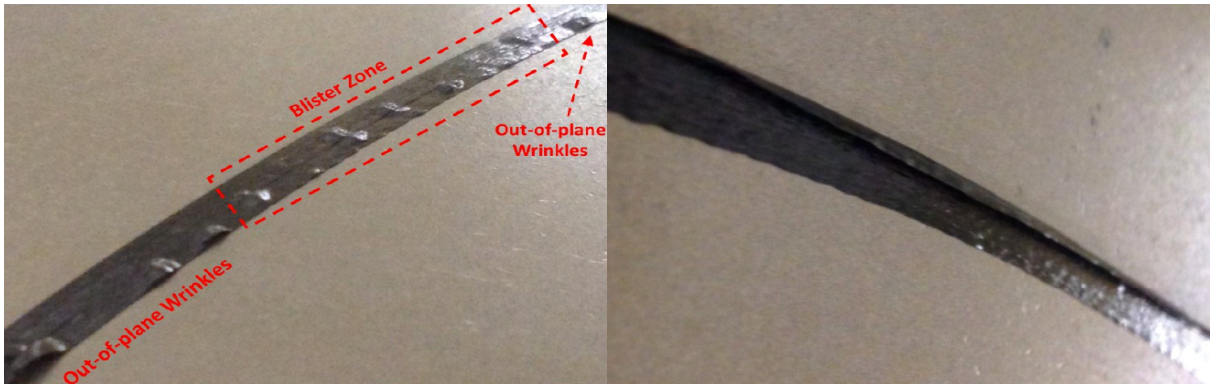

(a) Buckling and blisters (b) Tow pull up

Figure 2.10: Steering induced defects on thermoset prepreg tape [27]

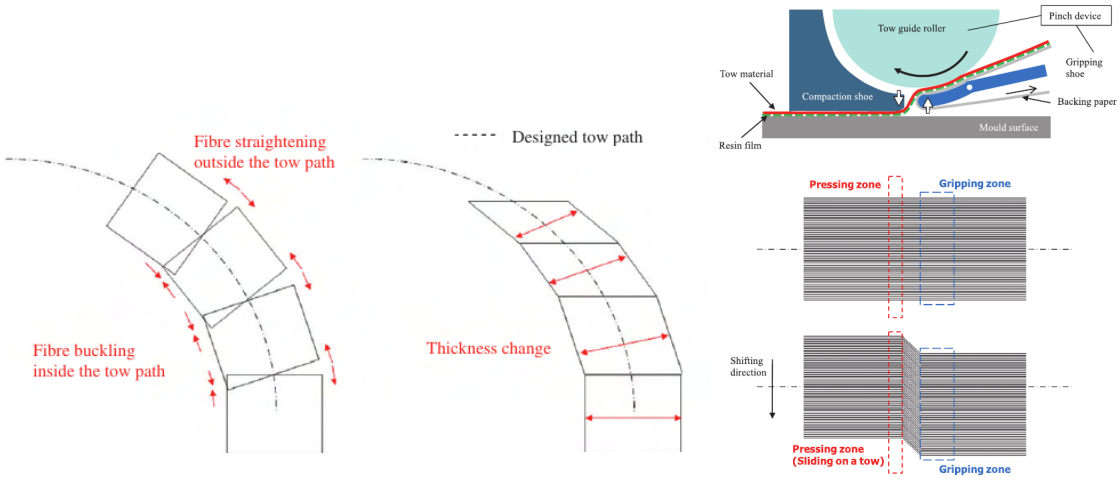

(a) Following a curve by continuously shearing (b) CTS schematic

Figure 2.11: Continuous Tow Shearing (CTS) [30]

defects observed in the thermoset prepreg tape placement such as tow kinking and tape folding as the fibers are not confined by the resin allowing them to bend and shear to conform more accurately to the guiding curve [29]. Due to this reason radius of $400mm$ is achievable using this process [15]. To secure the fibers in position, binder and/or veil (thermoplastic-based or epoxy-based) may be added to the dry fiber tape which will be melted during deposition and will fix the fibers in place. However, DFP requires additional steps of resin infusion and autoclave curing, thus, increasing the time required for the process.

Continuous Tow Shearing(CTS) is a novel method proposed by Kim *et al.*, for the purpose tow steering [30]. It is a modification of the dry fiber placement process where it

uses the ability of dry fibers being able to shear to conform to a curve without buckling or stretching, as shown in Figure 2.11a [30]. In CTS, the head was designed with a compaction shoe and gripping shoe. The gripping shoe along with the tow guide roller acts as a pinching device. When performing the layup, the dry fibers are affixed firmly by the compaction roller on the substrate while the pinching device holds also the tape at a distance of $7mm$. The pinching device then shifts along with the head which moves to follow the designed curve, thus, shearing the fibers in between, as shown in Figure 2.11b [30]. Thus, the dry fibers are made to conform to the curve by shearing in small increments all along the curve. Due to this mechanism the speed of the head is very slow, around $3mm/s$, which increases the process time. The CTS technique works best with dry fibers, however, the resin can also be infused in-situ to the tape by heating with a hot roller and then infusing it into the fibers using the tow guide roller and compaction shoe. Such a tape may be considered semi-impregnated and has the advantages of both prepreg and dry fibers. Since the resin layer is below the dry fibers, it is sticky enough to be affixed firmly on to the substrate while being dry enough to allow the fibers to shear without any buckling [30]. While the use of the resin film does improve the process efficiency it still results in a poor infusion leaving a lot of regions with dry fibers. Continuous Tow Shearing (CTS) is a promising new method to steer thermoset composite tapes without defects. However, it is has the drawbacks of being very slow and poor in-situ resin infusion which may require an additional step of resin infusion after the fibers are steered which will further increase the process times. Furthermore, CTS has been demonstrated to work well along flat substrates, however, its ability to steer over curved surfaces is unknown.

2.5 Thermoplastic fiber steering

So far, numerous studies which have explored fiber steering using thermoset composites, including a novel method like CTS, have been discussed. However, all these studies and processes have one common shortcoming. The thermoset tape placement process is not in-situ, *i.e.*, the curing of the resin does not take place simultaneously as the tape is laid

down. It requires an additional energy and time consuming secondary process of curing in an autoclave. However, the number of studies on the production of VAT laminates using in-situ consolidation of thermoplastic prepreg tapes is very limited [9, 16]. In-situ manufacturing techniques, like Hot Gas Torch-assisted AFP, use thermoplastic composite prepreg as material and consolidate the composite tape directly on to the substrate by melting the thermoplastic resin using a high energy heat source and applying pressure through a roller. The working of a HGT-assisted AFP has been explained in Section 2.2.1. Like thermoset AFP processes, thermoplastic AFP processes also have the ability to steer composite prepreg tapes. In a study by Lamontia *et al.*, they manufactured several components like pipes, panels, rings etc by using in-situ consolidation of AS4-PEEK tapes with a hot gas torch [16]. They also briefly explored the ability of the HGT-assisted AFP to steer AS4-PEEK tapes and succeeded in placing tows with a minimum radius of $1270mm$ without any noticeable defects due to steering. A study by Clancy *et al.*, investigated the ability of a Laser Assisted Tape Placement (LATP) process to steer CF-PEEK tapes and the influence of the process parameters on the bond strength [9]. The LATP process is very similar to the HGT-assisted AFP process with the main difference being the heat source, a schematic of the process has been shown in Figure 2.12 The process parameters considered by them were the steering radius of the tape and laydown speed. They succeeded in producing steered tapes up to a minimum radius of $400mm$ with minimal or equal number of defects in comparison with the thermoset counterparts. Due to defects such as buckling and tape shearing (See Figure 2.13), they found significant variation in the width and thickness of the steered tape when compared to a straight tape [9]. The bond consolidation between the tape and the substrate was studied with the help of a microscope. The microscopy showed good bond consolidation overall except at the edges which suffered due to the buckling and tape folding defects [9]. A novel peel test was devised to test the bond strength of the steered tape with the substrate (See Figure 2.14). Such a test was necessary due to a lack of standard tests to test the bonding between a steered composite tape and its substrate. However, the quantitative results of the mechanical testing were not conclusive as the failure modes

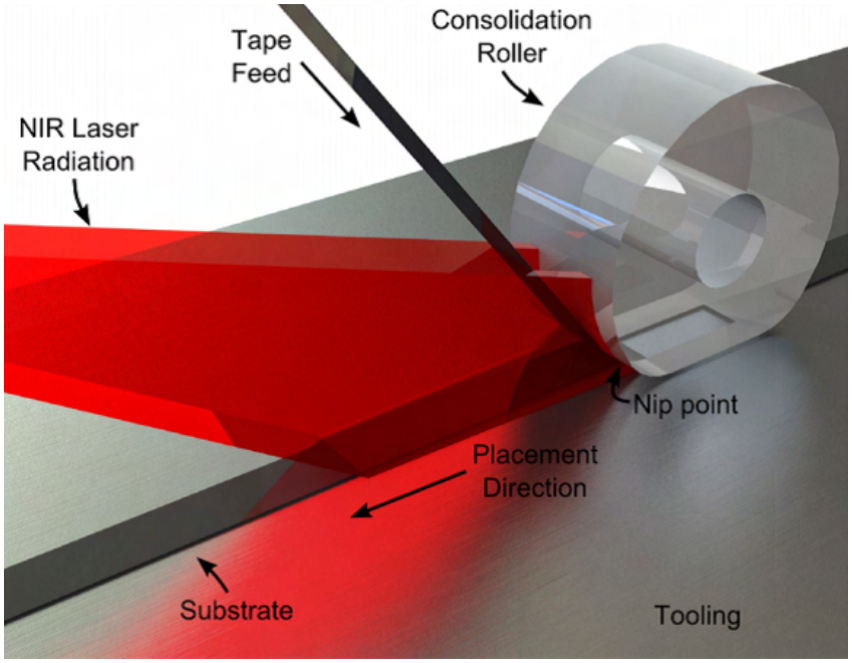

Figure 2.12: Laser Assisted Tape Placement (LATP) schematic [31]

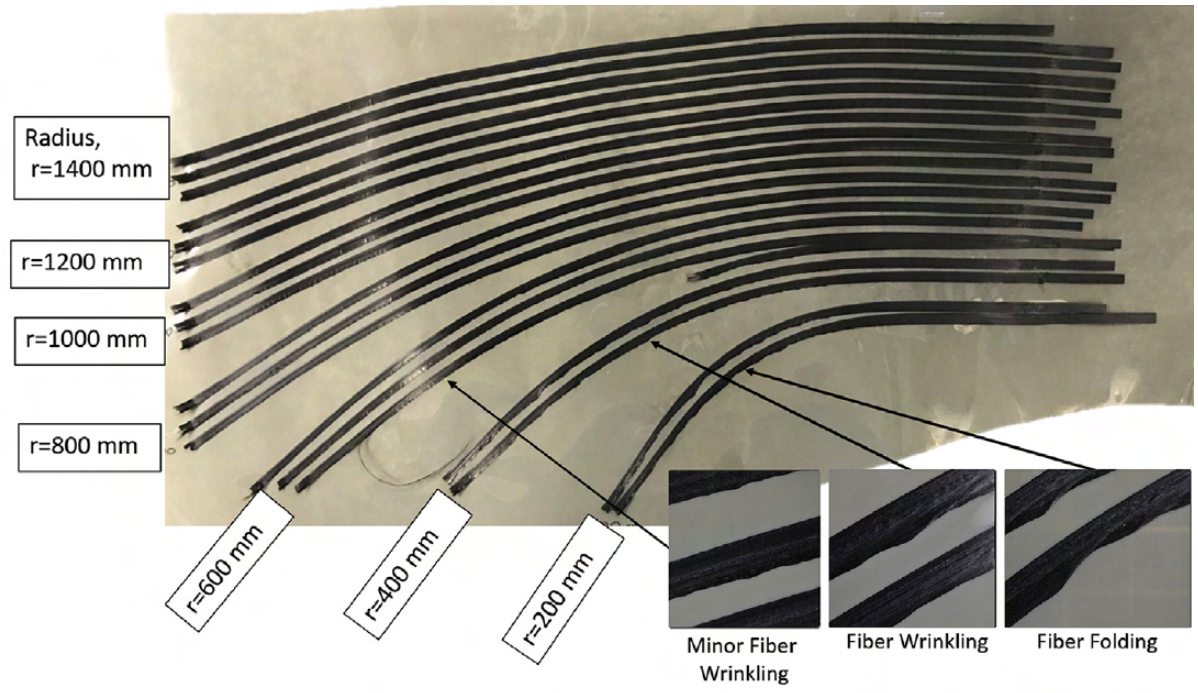

Figure 2.13: Defects due to fiber steering with LATP process [9]

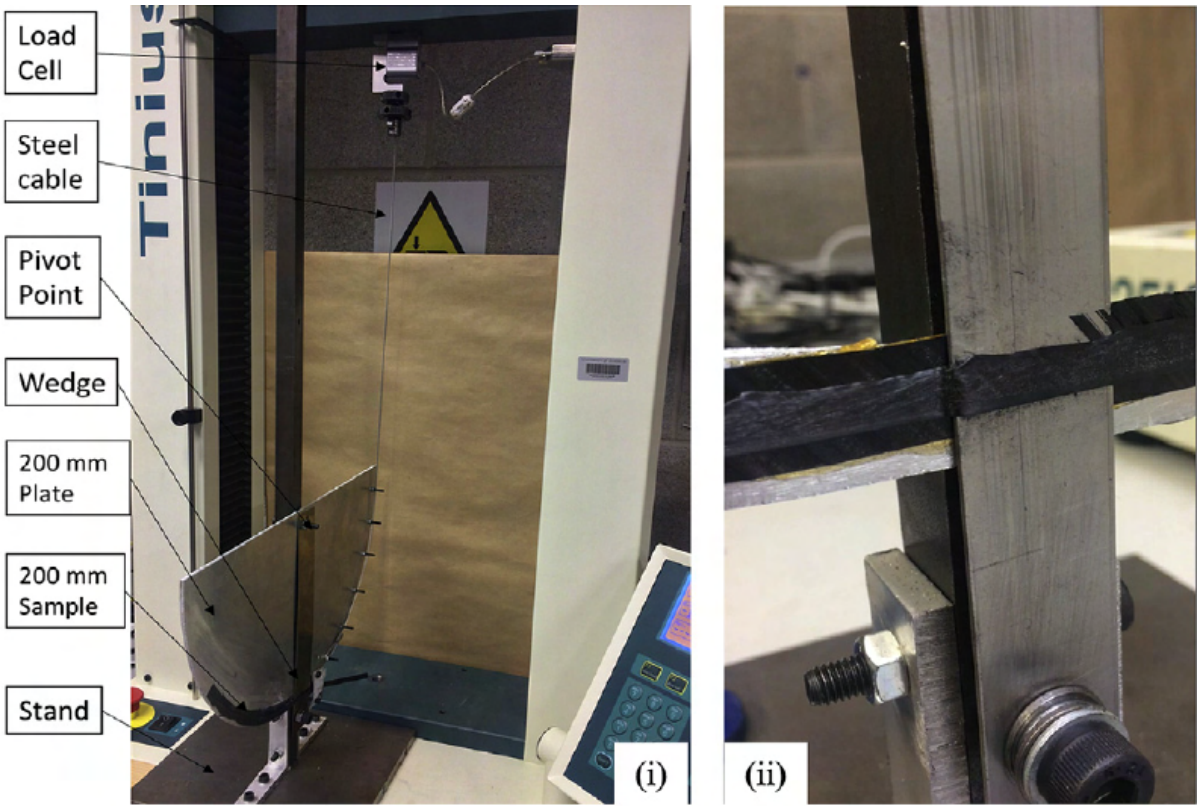

Figure 2.14: Novel wedge peel test by Clancy *etal.* [9]

of the peel test were not as expected. While the quantitative values were unreliable from the mechanical testing they qualitatively concluded from the trends observed that peel strength decreases with increasing laydown speed while it increases with increasing steering radius [9].

This thesis work aims to fill the knowledge gap of fiber steering using in-situ consolidation of thermoplastic composite tapes. Specifically, the ability of the Hot Gas Torch-assisted Automated Fiber Placement process to steer Carbon Fiber/PEEK composite prepreg tapes has been investigated. This investigation consists of two parts. First, effect of process parameters, *viz.*, steering radius, laydown speed and number of repass on the tape geometry and bond consolidation was investigated. Second, a modified lap shear test was devised to test the bond strength of steered CF/PEEK tapes and the effect of steering radius, laydown speed and substrate angle on the bond strength was studied. The need for a specially devised test is because of the lack of a standard test that can be directly applied to quantify the bond strength of steered thermoplastic composite tape. The various standard tests that are available to measure bond strength and the need for

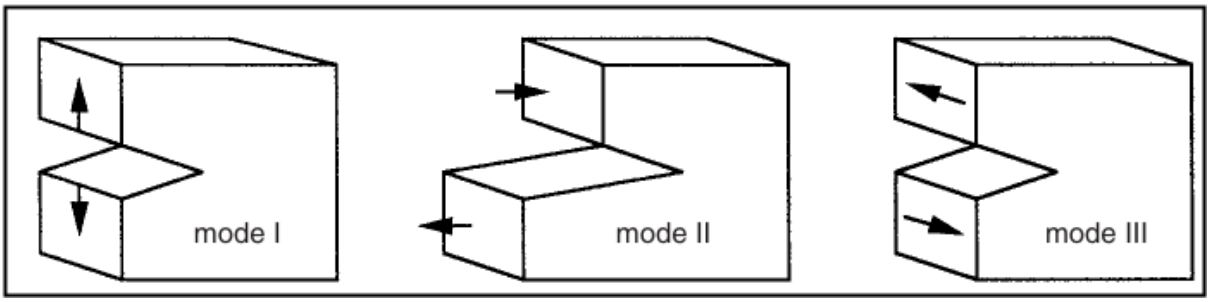

Figure 2.15: Schematic representation of interlaminar fracture modes [32]

a new test has been discussed in detail in Section 2.6.

2.6 Mechanical Testing

There are different types of tests that can be used to measure the bond strengths in composites *viz.*, delamination tests, peel tests and shear tests. Delamination tests help determine the inter-laminar fracture toughness, while peel type tests provide peel strength of the tape and shear tests measure the inter-laminar shear strength. These different types tests have been studied in order to find the most suitable one to measure the bond strength between a steered tape and its substrate, while also showing the effects of different process parameters.

2.6.1 Delamination tests

The most common type of tests are delamination tests, which are used to measure the inter-laminar fracture toughness in composite laminates [32]. There are three modes of failure in delamination tests as shown in Figure 2.15. Currently, for composite laminates, tests have been standardized for mode I and mode II type of failure. The ASTM standard D5528 prescribes using the Double Cantilever Beam (DCB) method to measure the mode I fracture toughness (G_{Ic}) of unidirectional laminates [33]. The schematic of a DCB test specimen is shown in Figure 2.16. The two laminate used is unidirectional and symmetric with even number of laminae to achieve mid-plane separation. An initial delamination is introduced between the two laminates using a thin non-stick film. The thickness of this film is restricted to a maximum of $13\mu m$ to prevent any resin rich areas that can

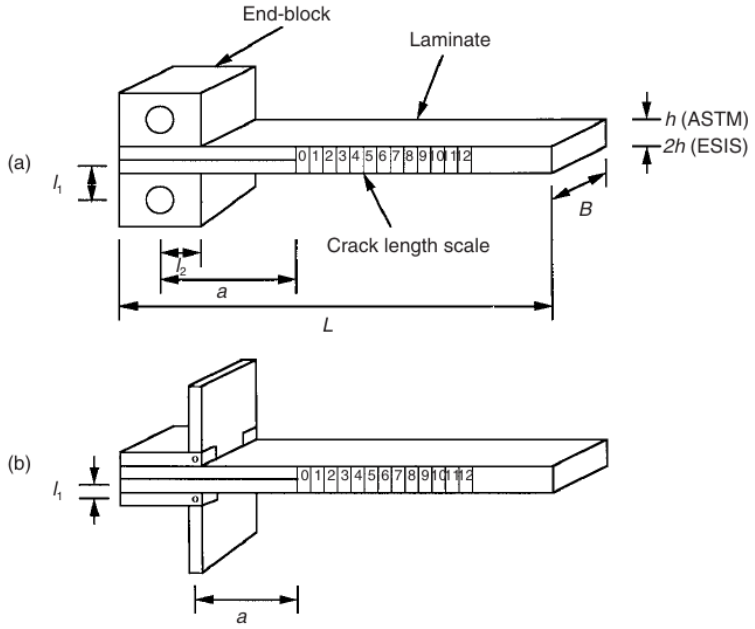

Figure 2.16: DCB test specimen schematic [32]

alter the initial inter-laminar toughness. End blocks or piano hinges are bonded carefully to the end of the specimen where the crack has been introduced. A scale is pasted on the laminate to track the propagation of the delamination front through the laminae. A tensile load is applied to the load blocks and the two laminates are slowly pulled apart at a rate ranging between $0.5 - 5mm/min$. The testing apparatus not only records the load and displacement but also uses an auxiliary camera system to track the corresponding propagation of the delamination front. The inter-laminar fracture toughness (G_{IC}) is not directly measured by the testing apparatus and needs to be calculated using the recorded data. There are three ways to calculate the G_{Ic} *viz.*, Modified Beam Theory (MBT), Compliance Calibration (CC) and Modified Compliance Calibration. All three methods produce results of G_{Ic} within 3% of each other, making them equally valid. However, the ASTM standard recommends the MBT method to calculate G_{Ic} as it is the most conservative of the three methods [34]. The expression to calculate G_{Ic} according to MBT is,

$$G_{Ic} = \frac{3P\delta}{2B(a + \Delta)} \tag{2.1}$$

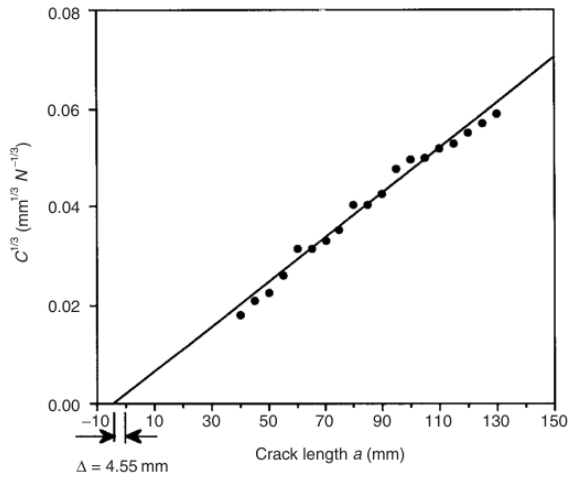

Figure 2.17: Determination of Δ for the Modified Beam Theory (MBT)

Where, G_{IC} is the inter-laminar fracture toughness, P is the applied load, δ is the displacement of the load point, B is the width of the test specimen, a is the delamination length and Δ is the delamination length correction that is used to account for any rotation that occurs at the delamination front. This Δ for the MBT can be calculated by plotting the cube root of the compliance ($C^{1/3}$) of the specimen against the delamination length a. (See Figure 2.17).

Pure mode I or mode II rarely occurs in inter-laminar failures for composites, it is usually a combination of mode I and mode II failure types. The ASTM standard prescribes a Mixed Mode Bending (MMB) test (D6671) to measure both mode I and mode II fracture toughness of unidirectional composite laminates [34]. Figure 2.18 shows a schematic of an MMB test. The specimen preparation for an MMB test is identical to a DCB test, only the test jig differs. The MMB test takes elements of the DCB test and short beam shear to induce delamination by both mode I and II. During the test, a downward force is applied to the end of the lever located on the opposite end of the initial crack. This downward force pulls the upper end block upwards by lever action while simultaneously a downward force is applied by the roller placed between the crack and lever end (See Figure 2.18). The specimen is supported by the base from the bottom through the end block and an additional roller. As the downward force is applied the specimens begins to delaminate slowly, and the load, displacement and crack propagation

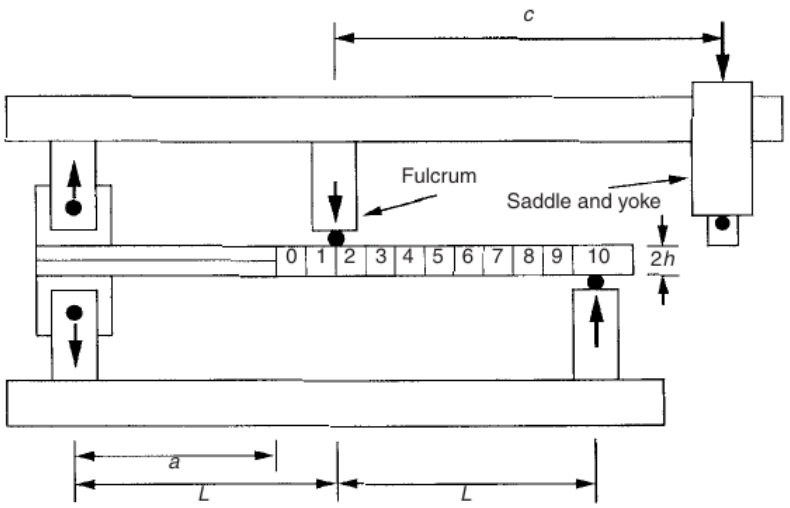

Figure 2.18: Mixed Mode Bending (MMB) test schematic

are recorded. The mode mixture can be varied by changing the distance c, which is the location of the top roller with respect to the lever end. The expressions used to calculate mixed mode inter-laminar toughness (G_{Ic} and G_{IIc}) are,

$$G_{Ic} = \frac{P^2(3c - L)^2(a + \Delta)^2}{16BL^2E_{1f}I}, \qquad c > L/3 \tag{2.2}$$

$$G_{Ic} = 0, \qquad c < L/3 \tag{2.3}$$

$$G_{IIc} = \frac{3P(c + L)^2(a + 0.42\Delta)^2}{64BL^2E_{1f}I} \tag{2.4}$$

Where, G_{Ic} is the mode I interlaminar fracture toughness, G_{IIc} is the mode II interlaminar fracture toughness, P is the applied load, B is the width of the specimen, c is the distance of the central roller from the load block, L is the half-span length of the MMB apparatus, I is the moment of inertia of one half of the delaminated specimen, a is the delamination length, and Δ is the delamination length correction that is used to account for any rotation of the delamination front. Δ is given by the expression [35],

$$\Delta = h\sqrt{\frac{E_{11}}{11G_{13}}\left(3 - 2\left(\frac{\Gamma}{1 + \Gamma}\right)^2\right)} \tag{2.5}$$

$$\text{where,} \quad \Gamma = 1.18\frac{\sqrt{E_{11}E_{22}}}{G_{13}} \tag{2.6}$$

Where, h is the half-thickness of the specimen, E_{11} is the longitudinal modulus of elasticity measured in tension, E_{22} is the transverse modulus of elasticity, and G_{13} is the out-of-plane shear modulus which can be assumed to be equal to the in-plane shear modulus, G_{12}, for a unidirectional composite.

Both DCB and MMB tests were standardized only for unidirectional laminates. This was because early testing showed that achieving mid-plane for non-unidirectional laminates would be very difficult [36–40]. This was due to the branching of the delamination front away from the mid-plane and into the off-axis plies, thus, corrupting the data obtained to calculate the fracture toughness. Several attempts were made to prevent the crack from jumping between plies, while there was some success the problem could never be fully eliminated [41–46]. This issue precludes it from being used as a measure of bond strength between a steered layer and its substrate. Another issue with using DCB and MMB tests for VAT laminates is that they will also have other steering defects such as gaps and overlaps. It will be difficult to measure the effects of the process parameters due to the interference caused by such defects.

2.6.2 Peel Type Tests

Peel tests are generally used to measure the peel strength of adhesive tapes. These test can be modified to be used with composite tapes [47, 48]. There are several peel tests provided by the ASTM standard: 90° peel test (D6862), T-peel test (D1876) and floating roller peel test (D3167) [49–51]. The schematic of the 90° and T-peel tests have been shown in Figure 2.19. The key difference between them is that the 90° peel test uses the jaws of a Universal Testing Machine (UTM) to peel the tape off a horizontal platform that moves in sync with the testing head. While the T-peel test uses the two jaws of a UTM to peel off two pieces of tape that have been adhered together. Both these tests provide the peel strength of the adhesive in kN/m. However, in 90° peel test the user has the option of choosing the substrate on which the adhesive is tested, making it much more versatile.

Another type of peel test which can be used for composites is the ASTM standard

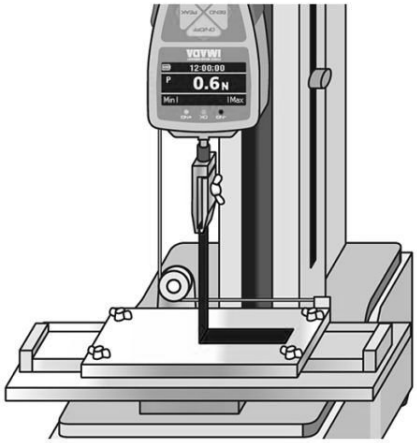

(a) 90° peel test (Imada Inc.)[52]

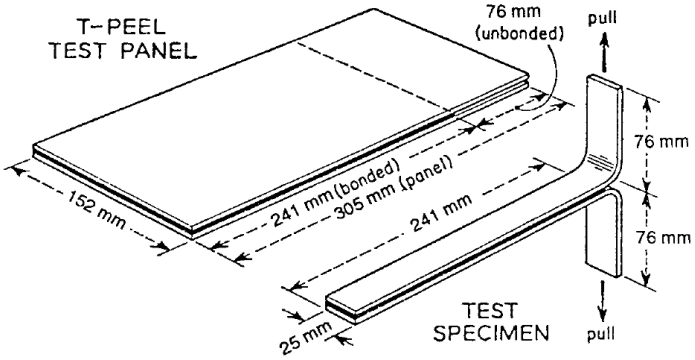

(b) T-peel test [50]

Figure 2.19: Peel tests schematic

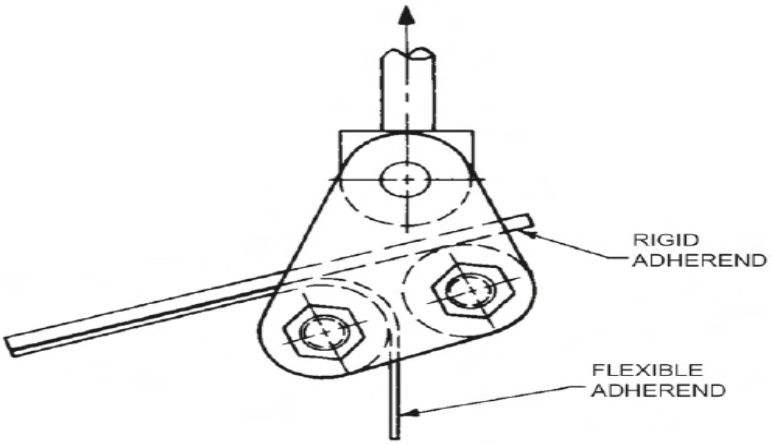

(a)

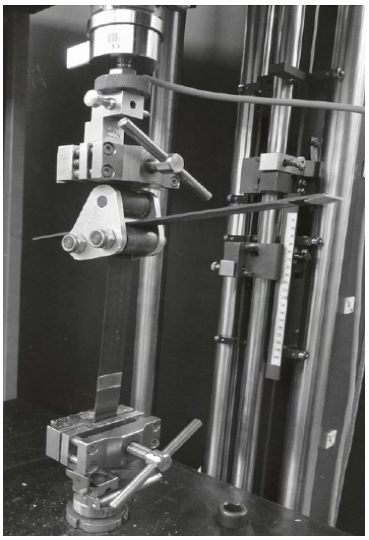

(b)

Figure 2.20: Floating roller peel test [53]

D3167 Floating roller peel test is generally used to measure the strength of the adhesives used for metal bonding. Figure 2.20 shows the floating roller peel test's schematic and setup. Although these tests have been designed specifically for adhesive tapes and adhesive bonded metal joints, they can be adapted to be used with composite tapes or bonded laminates. The test specimen for the floating roller peel test consists of one rigid adherent bonded to a flexible adherent. The flexible adherent is peeled off the rigid adherent through the floating roller by applying a tensile load (See Figure 2.20). This arrangement allows the flexible adherent to be peel at less sharper angle when compared to the 90° or T-peel tests. This allows the user to test very strong adhesives while avoiding any unwanted failure of the flexible adherent. De Freitas *et al.*, successfully demonstrated that the floating roller peel test can be used to measure the peel strength of composite-aluminum and composite-composite joints [48, 53]. While the 90° peel, T-peel and floating roller peel tests can be modified to be used with bonded laminates it is not straightforward to use them to measure the bond strength between a steered tape and substrate manufactured by the HGT AFP process. The primary reason is that these tests require at least one flexible layer that can be peeled. CF/PEEK tapes which are consolidated in-situ are brittle and not flexible enough to be peeled from the substrate without breaking using these standard tests.

A solution to perform peel tests on tapes or laminates consolidated by the AFP process is to use a wedge to aid in the peeling of the tape from the substrate. A study done by Hulcher *et al.*, [54] showed that wedge peel tests shows a similar data trend in comparison to standard DCB tests and they measured an average wedge peel strength of 3.4 N/mm. The test was performed on a two ply system instead of using unidirectional laminates like the standard DCB tests (See Figure 2.21). This method was also successfully applied by Comer *et al.*, [55] to measure peel strength of a CF/PEEK two ply system manufactured by LATP process and reported a highest peel force of 4.1 N/mm. Unfortunately, this test method has not been a reliable quantitative measure of the bond strength as it provides us with several peaks or initiation values in the load displacement curve, unlike the DCB test which shows only one initiation value per specimen (See Figure 2.21). For this reason

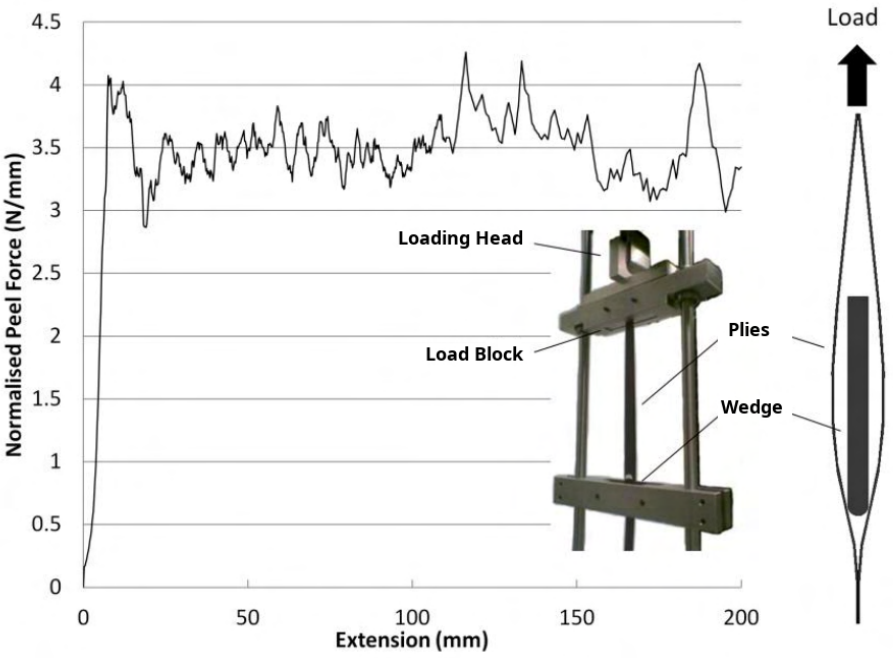

Figure 2.21: Wedge peel test for unidirectional plies by Comer *et al.*, [55]

this test method has usually been used as a qualitative reference like in the case of Khan *et al.*, where they used this method and a short beam test to get a complete measure of the inter-laminar bond strength of CF/PEEK laminate manufactured by an HGT AFP [56].

The two ply wedge peel test can be adapted to be used with steered tapes manufactured by the AFP process. The important point in this type of adaptation is to ensure that wedge and tape are always perpendicular while the tape is being peeled. This requires a special rotating apparatus to maintain the perpendicularity between the tape and the wedge. Clancy *et al.*, recently used one such adaptation of the wedge peel test to measure the bond strength of steered tape that was consolidated in-situ by the LATP process [9] (See Figure 2.14). They tested several samples that were manufactured with different steering radius and different laydown speeds. However, many samples tested failed by an undesirable failure mechanism either by slicing or tearing, so the results obtained were subject to only a qualitative analysis. They observed a trend where the bond strength of the steered tape decreased with increasing laydown speed. Several studies adopting the wedge peel test has shown us that, while the wedge peel test can give a good qualitative analysis of the bond strength it cannot be used reliably as a quantitative

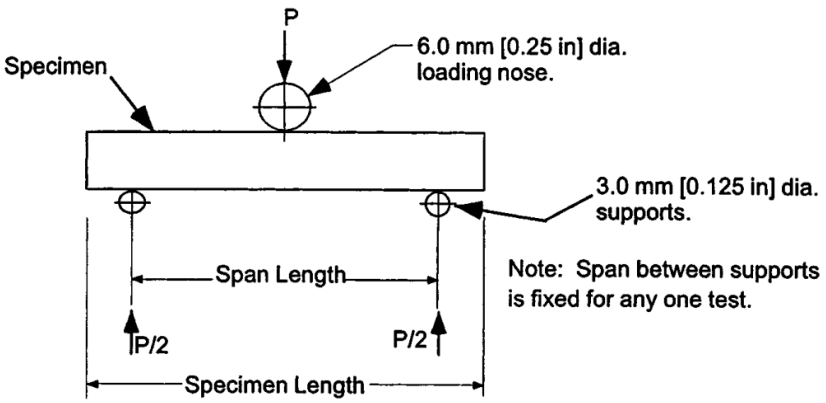

(a) Short beam shear test schematic

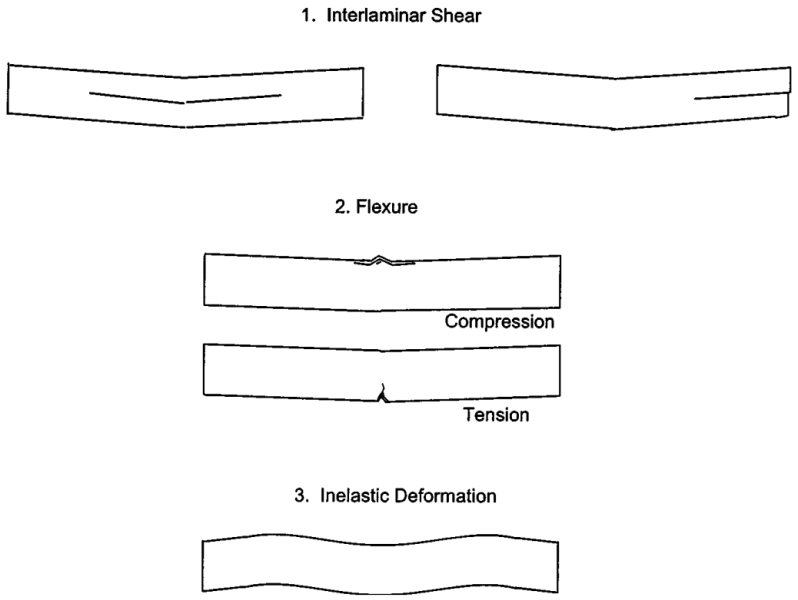

(b) Short beam shear test failure modes

Figure 2.22: Short beam shear test [57]

measure of it.

2.6.3 Shear Type Tests

There are three standard shear type tests that can be used to measure the bond strength of a composite laminate *viz.*, Short beam shear test (ASTM D2344), Double notched shear test (ASTM D3846) and the Lap Shear test (ASTM D5868) [51, 57, 58].

The Short Beam Shear (SBS) test, shown in Figure Figure 2.22, is designated by ASTM as D2344. It is a type of 3-point bending test that is used to measure the Short-beam strength of the laminate [57]. This test was designed to be used for composite

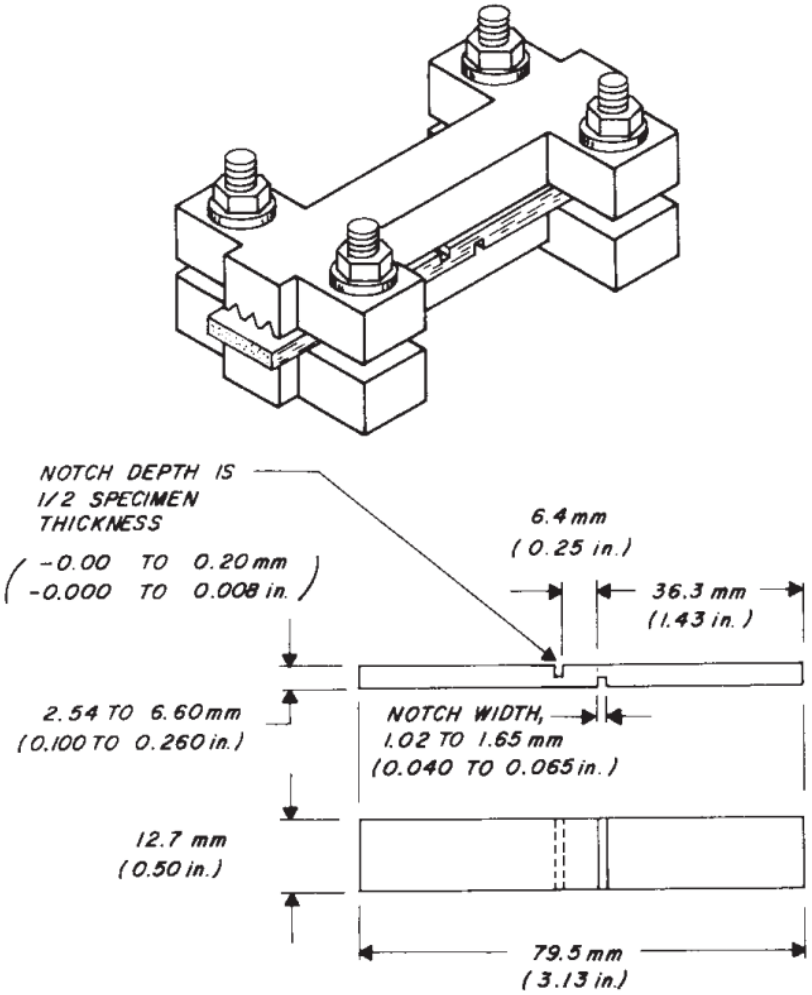

Figure 2.23: Double-notched in-plane shear test [58]

laminates with symmetric and balanced plies. It should be noted that this test is not restricted to unidirectional plies and can also be used with multidirectional plies, provided the laminate is symmetric and balanced with at least 10% of 0° plies. The short beam shear tests can also be used as a measure of Inter-Laminar Shear Strength if the failure mode is a clear mid-plane failure due to shear. It is difficult to achieve such a clear mid-plane failure due to the large stress concentration around the loading rollers which can initiate failures due to compression or tension (See Figure 2.22b). Therefore, the ILSS obtained through this test is called *Apparent Inter-Laminar Shear Strength* and is generally used for qualitative comparison. Moreover, in use with VAT laminates, the issue of interference of other steering induced defects such as gaps and overlaps, mentioned in Section 2.6.1, still exists.

(a) Lap Shear test specimens (b) Lap Shear test

Figure 2.24: Lap Shear Test for unidirectional composite [59]

The ASTM D3846 double-notched in-plane shear test is used to measure the in-plane shear strength of flat laminates [58]. The schematic of the specimen used in this test is shown in Figure 2.23. Two notches or cuts are made $6.4mm$ apart on opposite faces of the test specimen. The notches are made deep enough to reach the mid-plane of the specimen. The test specimen is then placed in a jig, as shown in Figure 2.23, to prevent any unwanted twisting or bending during loading. Finally, a compressive load is applied to the specimen till the area between the notches fails by shear. This test can be used with both unidirectional and multidirectional composite laminates. Moreover, owing the special jig used to constrain the test laminate, this test doesn't have the strict requirement of using symmetric and balanced laminates like the short beam shear test (D2344). As this test requires a laminate to be manufactured and then the specimen cut and sized from that laminate, it has the same issue of interference due to gaps and overlaps when used with a VAT laminate. The design of this test specimen can be modified and be used with individual tapes. Stokes *et al.*, used such a modification to measure the shear strength of tapes laid down using an LATP process [31]. However, such a modification was used with straight tapes and does not lend itself well to be used with steered tapes.

The lap shear test is another type of shear test that can be used as a quantitative

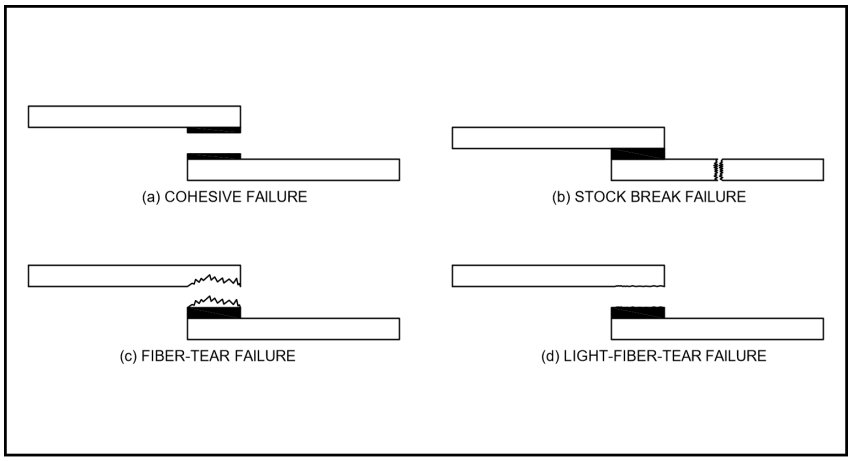

Figure 2.25: Failure modes for Lap Shear Test [51]

measure of the inter-laminar bond strength. The lap shear test - D5868 is prescribed by ASTM to measure the strength of the adhesive used to bond two Fiber Reinforced Plastic (FRP) laminates or an FRP laminate with a metal plate [51]. This test can be adapted easily to be used with laminates manufactured in-situ by the AFP process. The standard's sample preparation requires two $101.6\,mm$ $(4\,in)$ by $25.4\,mm$ $(1\,in)$ rectangular FRP laminates bonded by an adhesive over an area of $6.45\,cm^2(1\,sq.in)$. This type of samples can be manufactured by using an AFP with the only difference being that the bond between the two carbon fiber reinforced thermoplastic laminates is consolidated in-situ by using hot gas torch or a laser. The failure methods that can be observed by adapting this method are very similar to the standard failure criteria, the overlapping failure modes between the two are illustrated in Figure 2.25. The desired failure mode for a successful a lap shear test are either a cohesive mid-plane failure or a Light Fibre Tear (LFT). This method was adopted in a study by Qureshi *et al.*, [59] (See Figure 2.24) to measure the bond strength between a CF/PEEK laminate manufactured by an HGT AFP and a laminate of the same material which was manufactured in an autoclave. The reference used in this study was two laminates processed in the autoclave to form a lap joint. They reported a lap shear strengths in the range of $9 - 14\,MPa$ depending on the tool temperature with the reference lap shear strength being $25.7\,MPa$. The important thing to be noted from the study is that all the samples manufactured by the HGT AFP failed by Light Fiber Tear, a desired failure mode. Due to the nature of the lap joint this

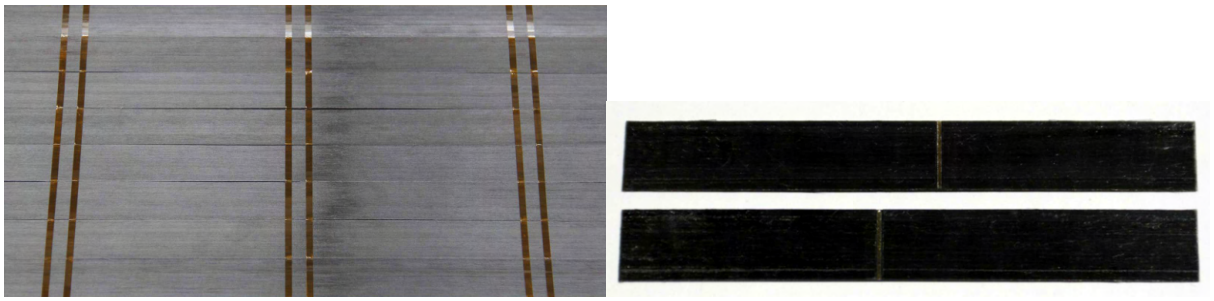

(a) Limiting gauge area by spacing polyimide tapes $6mm$ apart

(b) Lap Shear test specimen

Figure 2.26: Stokes-Griffin's unidirectional 2-ply Lap Shear test [31]

test can also be easily adapted to test the bond strength between individual CF/PEEK tapes. However, to achieve the desired failure mode, great care is required in preparing the lap joint of individual CF/PEEK tapes. With only one or two tapes to withstand the tensile load applied during a Lap Shear test, the area of the lap joint must be reduced to ensure the desired failure mode. Stokes Griffin *et al.*, [31] achieved this by placing two polyimide tapes $6\,mm$ apart on the substrate and then consolidated the second layer on top of this (See Figure 2.26a). The polyimide tapes ensured that the composite tape would bond to the substrate only within a length of $6mm$. To get a lap joint, the tapes were precision cut on the top and bottom up to the polyimide tape (See Figure 2.26b). They reported lap shear strengths (LSS) in the range of $25 - 40MPa$.

There are several testing methods to choose from, each with its own advantages and scope of application. However, most of these methods cannot be directly used to measure the bond strength between a steered CF/PEEK tape laid down using an HGT AFP on a CF/PEEK substrate. Standard delamination methods like DCB cannot be used for individual steered tapes and even when used with laminates made of steered tapes it will suffer from the delamination front branching away from the mid-plane. The consolidated CF/PEEK tapes are not flexible enough to be peeled off by using the standard peel tests. A workaround for this it to use a modified peel test that uses a wedge to aid in the peeling of the tape. However, peel tests or wedge peel tests tend to provide multiple peaks for each individual sample without providing one clear failure point for each sample like the lap shear test. Moreover, as observed by Clancy et al., when used with steered tapes it does not result in a desirable failure mode [9]. Shear type tests seemed to be best suited to

measure the bond strength of a tape steered using an HGT AFP. The short beam shear tests requires the use of a symmetric and balanced laminate. This is difficult achieve using steered tapes and the test can't be easily modified to be using with individual tapes. The in-plane shear test doesn't require symmetric and balanced laminates and can be modified to be used with individual tapes. However, that is true only in the case of straight tapes and not steered tapes. Of the available testing methods the lap shear test is the most promising for this specific application. However, even the lap shear test cannot be used directly without any modifications. Thus, a new mechanical test, inspired by the lap shear test, has been developed and proposed to measure the bond strength of steered CF/PEEK tapes on a CF/PEEK substrate (See Chapter 3).

2.7 Knowledge Gap and Thesis Objective

In this chapter, various studies on fiber steering and the manufacturing of Variable Angle Tow (VAT) laminates have been reviewed and presented. From these studies, the clear knowledge gap in understanding of the ability of in-situ AFP processes to steer thermoplastic composite tapes has been shown. The main objective of this work is to help fill this knowledge gap by investigating the ability of HGT-assisted AFP process to steer CF/PEEK composite tapes. To aid in this investigation a mechanical test is required to help measure the bond strength of the steered CF/PEEK tape with its substrate. To choose the most suitable test for this task, various standard mechanical tests have been reviewed and presented. However, it was found that none of these standard tests can applied directly to a steered CF/PEEK tape and that new test was required. So, another aim of this thesis is to propose a new mechanical test to evaluate bonding between the steered tape and the substrate. A further objective is to study the applicability of available analytical buckling solutions in the literature to predict critical steering radius of Carbon fiber/PEEK tape.

Chapter 3

Fiber Steering using HGT-assisted AFP Process

In this chapter, the various trials and experiments performed to investigate the ability of the HGT-assisted AFP process to perform fiber steering has been detailed. In Section 3.1, the materials and the manufacturing setup used in this work to perform fiber steering has been described. Following that, in Section 3.2 the initial trials used to help design the experiment which investigates the effects of different process parameters on fiber steering have been described. In Section 3.3, the design of the experiment has been summarized. Following that, in Section 3.4, the techniques used to evaluate the quality of the steered tapes, *viz.*, Geometrical Analysis, Microscopic Analysis and Mechanical Testing, have been described. Of particular note in this section is the autoclave procedure used to re-consolidate the steered tapes to serve as a reference for mechanical testing (See Section3.4.3.1). In Section 3.5, the results of the evaluation of the samples by various techniques has been reported and discussed. Finally, Section 3.6 describes the salient points of the various experiments and summarizes the effects of the different process parameters on steering of CF/PEEK tapes using HGT-assisted AFP process [60].[1]

[1]The content in this chapter has been published in a journal by the author.

3.1 Materials and Manufacturing Setup

This work used the HGT-assisted AFP to perform the in-situ consolidation of carbon fiber/PEEK composite tape. The thermoplastic AFP head system supplied by Trelleborg is mounted on to a Kawasaki articulated arm robot which has 6 axis and $125kg$ payload. A flat aluminum mandrel was used to perform all the trials. The carbon fiber (AS4)/PEEK (APC-2) tape provided by Solvay is used in this study. It has a width of $6.35mm$ $(0.25in)$, a thickness of $0.163 \pm 0.017mm$, a fiber volume fraction of 60 and a glass transition temperature of $143°C$ $(289°F)$. Roughness (arithmetic mean deviation from the mean (Ra)) of the tape perpendicular to fiber direction after processing with no repass and one repass was measured to be $40.7 \pm 3.57\mu m$ and $6.2 \pm 0.41\mu m$, respectively [61]. Nitrogen was used as the hot gas in the HGT-assisted AFP process as it does not cause any unwanted chemical reactions even at high temperatures. A steel compaction roller with a diameter of $12.7mm(0.5in)$ and a width of $17.78mm(0.7in)$ was used in this study as it can withstand very high temperatures without degrading or experiencing large dimensional changes.

3.2 Initial Trials

Initial trials were performed to help design the experiment and decide some common process parameters *viz.*, HGT temperature, compaction force. Two layers of CF/PEEK tapes were wrapped around a cold aluminum mandrel at a speed of $10.16cm/s$ $(4in/s)$ to serve as a substrate for fiber steering. A substrate prepared by the HGT-assisted AFP process was chosen because fiber steering would likely be performed on a substrate that was laid down by the same manufacturing process. Moreover, the end result might be affected by the use of a flat PEEK substrate or CF/PEEK laminate prepared in an autoclave, since, the roughness of these surfaces compared to the HGT-assisted AFP substrate is very low [61]. However, with only two layers, after a few hours, a lot of warping and waviness was observed. The number of substrate layers was increased to four layers to eliminate any warping or waviness on the surface before doing the steering

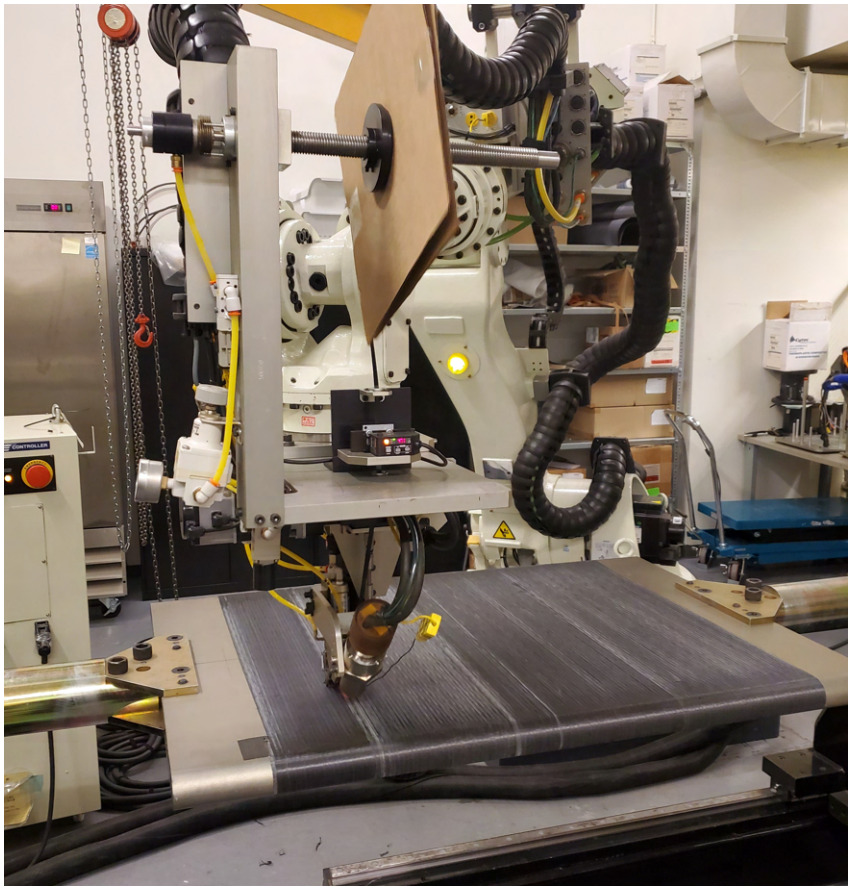

Figure 3.1: Hot Gas Torch-assisted Automated Fiber Placement

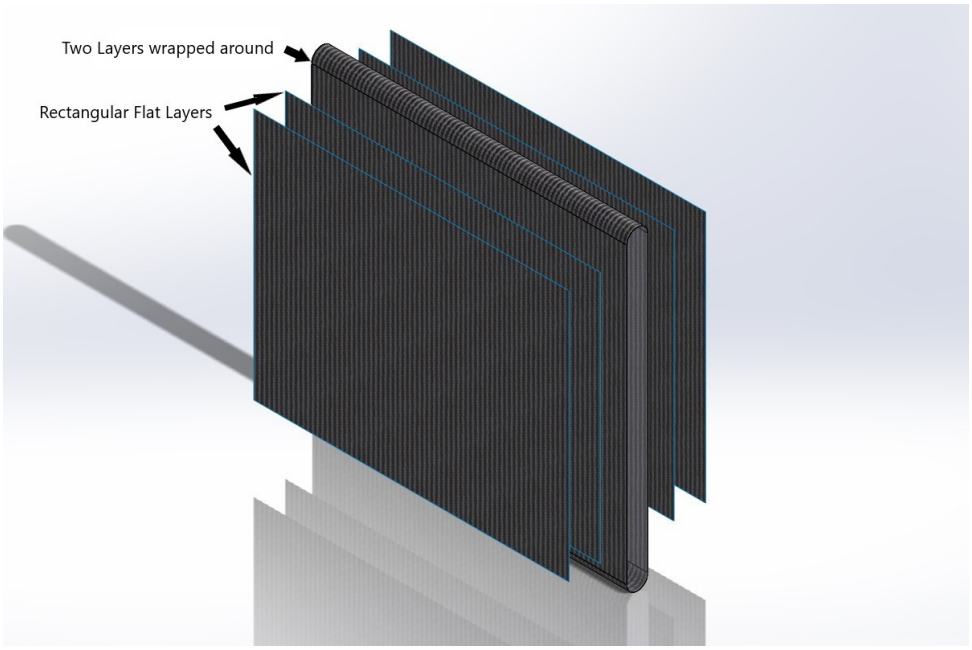

Figure 3.2: Substrate preparation schematic

of the tape. Since a substrate of poor quality can adversely affect its bond with a steered tape. The third layer was laid down in a rectangular region on top of the two layers on both faces of the mandrel. A repass was performed after the third layer to reduce the waviness of the substrate. However, it was found that a pressure of $266.89N(60lbs)$ was too excessive and only exacerbated the waviness. So, another rectangular region of substrate was laid down on both faces to form the fourth layer (See Figure 3.2). And then, final repass was performed but with a much lower force of $44.48N(10lbs)$. The resulting substrate was much smoother and very little warping and waviness was observed. The schematic of the substrate preparation is shown in Figure 3.2. All four layers were not wrapped around to facilitate the easy removal of the completed sample from the mandrel without causing any damage to the mandrel's surface.

From previous studies by Clancy *et al.*, [9] it was understood that the larger radii are usually handled well by the AFP process, as the deviation from the linear path is more gradual when compared to the smaller radii. For this reason, the larger radius was initially restricted to $800mm$. In a previous study performed with an LATP process, it was found that the smallest radii that could be achieved without serious buckling and tape folding was $400mm$. To understand the lower limit of fiber steering using an HGT-assisted AFP process, the smaller radii were extended up to $100mm$ with smaller subdivisions between the final three radii ($200mm$, $150mm$ and $100mm$) tested.

The guide curves for different radii were prepared on a Solidworks model of the flat aluminum mandrel. The guide curve was designed for the following radii, $800mm$, $700mm$, $600mm$, $500mm$, $400mm$, $300mm$, $200mm$, $150mm$ and $100mm$. For each radii three guide curves were designed to ensure that the results are repeatable and in case there is a splice in feed spool which can stop the tape laying process. All the samples were designed with an initial straight portion of up to $200mm$ before it was steered to the designed radii. This was to allow a comparison of results between steered tapes and straight tapes.

The samples were then laid down at a speed of $5.08cm/s$ ($2in/s$), with the Hot-Gas (nitrogen) at a temperature of $850°C$ with a flow rate of 60standar litre per minute($slpm$) and a compaction force of $177.93N$ ($40lbs$). These initial process parameters were chosen

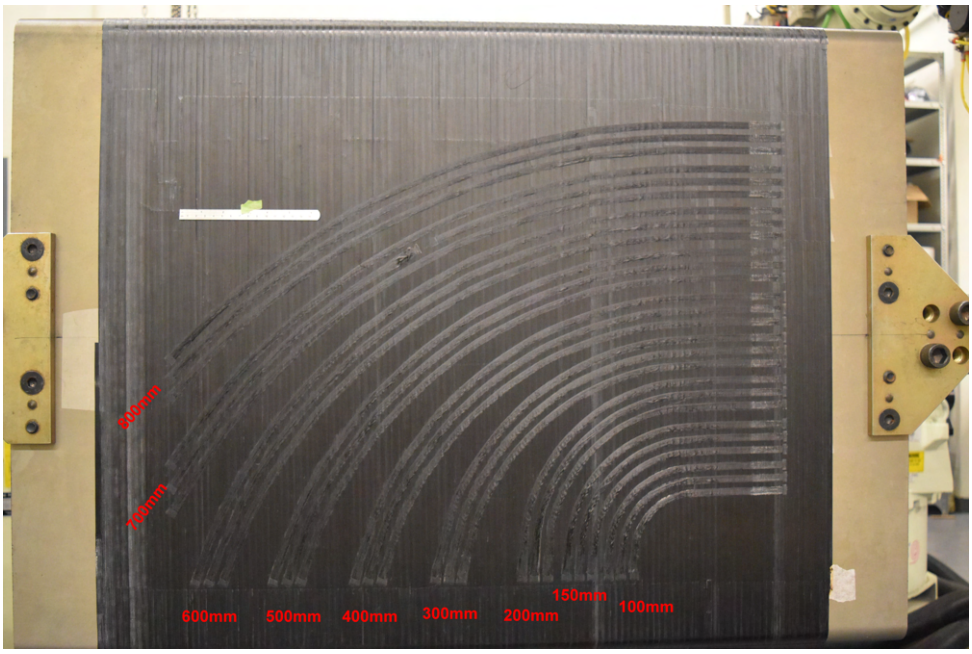

Figure 3.3: Initial steering trial

by referring to various works performed using this particular HGT-assisted AFP [23, 61–63]. This initial trial did not provide satisfactory results as the quality of the samples produced were poor. Almost all the samples suffered due to an issue with the fiber being pulled up after the roller passed over it. This indicated that the issue would be with the process parameters and not the process of steering itself. The trial was then repeated with an increased compaction force of $266.89N$ ($60lbs$) and a higher temperature of $875°C$. The issue of fiber pull-up was solved by the increased compaction force and HGT temperature.

By observing the steered tapes it was found that tapes from $200mm$ had severe fiber buckling and tape folding. Due to this the steering radius was restricted to a lowest of $200mm$ during the main experiment. Moreover, some fiber buckling was also noticed at the radius of $800mm$, hence, the largest radii in the main experiment was increased to $1000mm$. The quality of the tapes didn't vary much at a difference of $100mm$, so the difference between the steering radii was increased to $200mm$ in the subsequent experiment. At a radius of $400mm$, the tapes showed signs of both buckling and minor tape folding. Hence, this radius was chosen to be used for experiments with varying laydown speed and number of repass as their effects on these defects can be easily observed. The final experiment design which was derived from these initial trials is given in Section 3.3.

Table 3.1: Design of experiment

Sample no	Radius(mm)	Laydown Speed (cm/s)	No. of repass
1 - 15	1000, 800, 600 , 400, 200	5.08	0
16 - 30	400	2.54, 5.08, 7.62, 10.16, 12.7	0
31-39	600, 400, 200	5.08	0, 1, 2

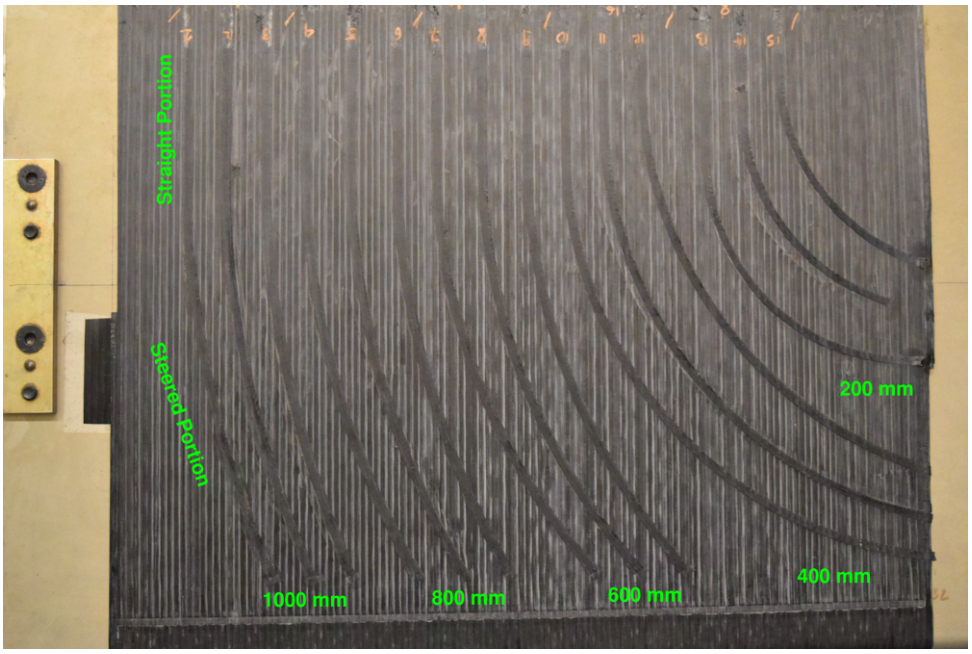

Figure 3.4: Tapes with different steering radii

3.3 Design of Experiment

The parameters investigated in this study are the steering radii, laydown speed and number of repass. Steered tapes with different radii from $1000mm$ to $200mm$ were manufactured while the laydown speed of $2.54cm/s$ and 0 repass were kept as constants to understand the effect of steering radii on the geometry and consolidation. Similarly, for laydown speeds varying from $2.54cm/s$ to $12.7cm/s$ ($1in/s$ to $5in/s$) the steering radius of $400mm$ was chosen to be constant. And the effect of repass was studied on samples with three different steering radii while keeping the laydown speed at $5.08cm/s$ ($2in/s$). Table 3.1 summarizes all samples that were manufactured for testing the effects of different process parameters.

All the samples were designed with an initial straight portion before it was steered at a radii as shown in Figure 3.4. This was to ensure good consolidation with the substrate

and to compare the results of analysis performed on the steered tapes with the straight tapes that were laid down with the same process parameters.

3.4 Sample Evaluation

3.4.1 Geometrical Analysis

A geometric analysis was carried out on the steered tape to understand how the width and the thickness of the steered tape change in comparison to a straight tape that was laid down with identical processing parameters. Furthermore, measurements were taken to study the percentage of length of the steered tape affected by steering induced defects such as tape buckling and tape folding.

The average width for the straight portion of the tape was obtained by taking 30 measurements from the three instances in total using a 'Mitutoyo' digital Vernier caliper. Similarly, the average thickness was obtained using a 'Mitutoyo' digital micrometer by taking 30 measurements from the three instances. This was repeated for every sample of different radius, laydown speed and number of repass.

Initially, the thickness measurements were taken along with the substrate thickness. Then the average thickness of the substrate alone was measured and found to be $0.6399 \pm 0.0249mm$. This average substrate thickness was obtained by taking 50 measurements at random locations of the substrate. The thickness of the steered layer alone was obtained by subtracting the average thickness of the substrate from it. To calculate the percentage of the tape affected by steering induced defects total arc lengths were calculated from the Solidworks design file and the defective arc lengths were measured by small differential lengths of 2mm using the Vernier Caliper, in cases where the final measurement was less than 2mm the exact measure was taken.

3.4.2 Microscopic Analysis

Optical microscopy was performed to see the effect of steering, steering induced defects and process parameters on the bond quality and fiber distribution. Samples were cut into

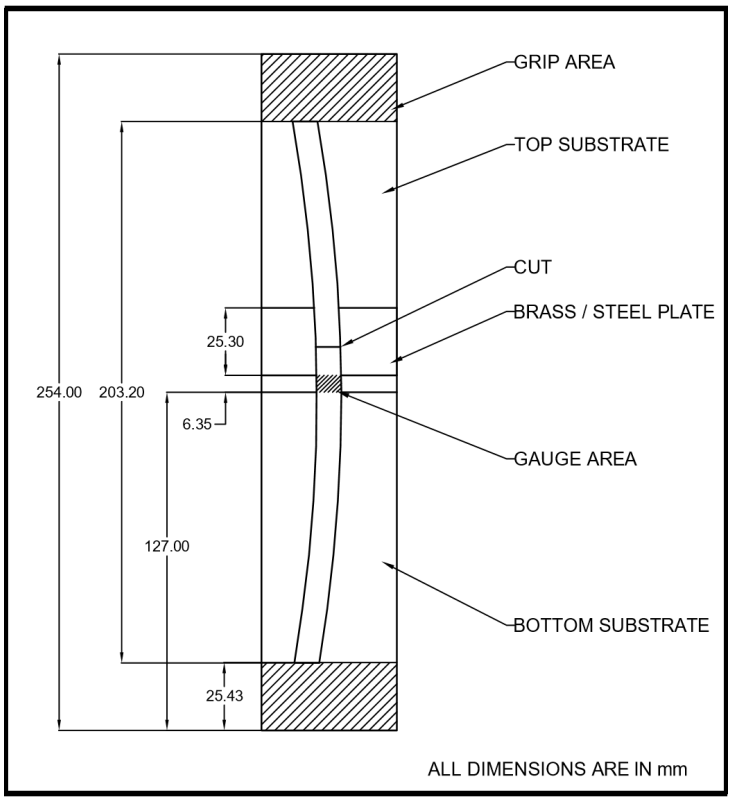

Figure 3.5: New shear type mechanical test schematic

equal widths using a diamond edge saw. They were placed in a holder and thin epoxy resin(DER 324) supplied by Anamet was added until the samples were just submerged. The resin was let to cure for 24 hours at room temperature and then was post cured at $100°C$ for 1 hour. Samples were then sanded to expose the composite laminate's cross-section and to obtain a translucent finish. They were then polished using 9μm and 3μm fine papers and diamond suspensions to obtain the clear transparent finish required for microscopy.

3.4.3 Mechanical Testing using a novel shear type test

A specially devised mechanical test was used to test the bond strength between the steered tape and a flat substrate prepared using the HGT-assisted AFP. This test is devised based on the Standard lap shear test (ASTM D5868-01) which is primarily for unidirectional Fiber Reinforced Plastic(FRP) laminates [51]. The new test was devised to be used for a single tape that were steered on a flat substrate. The gauge area of the proposed mechanical test is approximately $60mm^2(0.093in^2)$ when compared to the recommended

gauge area of $645.16mm^2(1in^2)$ ASTM D5868-01 standard. The reason for selecting a smaller gauge area is to avoid the undesired stock-break (fiber breakage) failure mode. The gauge area was calculated such that the resulting failure mode would be Light-Fiber-Tear(LFT) or Cohesive failure as shown in Figure 2.25 [64]. While a smaller gauge area can result in larger standard deviations, it still provides repeatable results.

Flat substrate panels of were manufactured using the HGT-assisted AFP with the configuration of $[0_4]$. These panels were then cut into $127mm$ X $50.8mm$ pieces. Two of these pieces were then affixed on the mandrel using double-sided tape to form a $254mm$ X $50.8mm$ substrate for a single sample. To limit the length of the gauge area to $6.35mm$ $(0.25in)$ a $25mm$ wide and $0.125mm$ thick brass plate was placed to prevent the steered tape from sticking to the substrate. The brass plate was held in place using duck tape on the sides of the substrate. Bonding the brass plate to substrate with an adhesive is not advised as the adhesive would melt under the high temperature of the HGT and will affect the bond between the tape and substrate. This was also the reason why polyimide tape was not used like in the study by Stokes-Griffin et al. [31] using a LATP machine. The Hot Gas Torch cannot direct the heat to a very narrow area like a laser, thus it requires more temperature resistant materials like brass or steel to be used as a barrier.

The CF/PEEK tape is then steered over the substrate at the desired radius and speed. For a low speed like $2\,in/s$ the tape can start within the bounds of the substrate and still reach the desired speed of $2\,in/s$ at the gauge area. However, if higher speeds are required, some testing is needed to see how long it takes for the robot arm to accelerate to the required speed and the substrate should be placed on the mandrel so that the required speed is reached at the gauge area as shown in Figure 3.6a.

After steering, the tape over the brass plate is cut so that bond strength at the gauge area can be tested by applying a tensile load. Figure 3.5 and 3.6 show the schematic and preparation of the sample for the specially devised mechanical test which is tested under tensile load using a Universal Testing Machine(UTM).

The sample is then removed from the mandrel using a thin wedge. Care must be taken to not damage the sample during this step. It is recommended to arrest the movement of

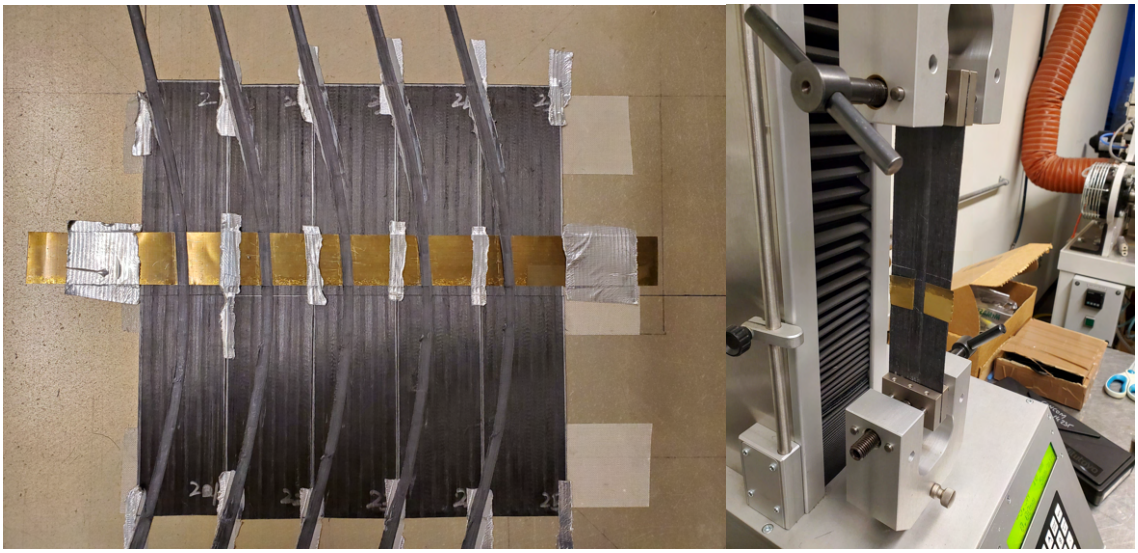

(a) Sample Preparation (b) UTM Testing

Figure 3.6: Novel shear type mechanical test

the samples after removal using some tape so that it doesn't twist or fold and damage the fibers across the split of the substrate. Since steering of fibers results in a change in width of the tape depending on the radius used, it is important to measure the width of the tape and calculate the area to get a true measure of the bond strength. Approximating the gauge area as two trapeziums reduces the chance of errors during area calculation significantly. Tabs may be prepared and bonded to the substrate if required. Since the substrate in this case is only 4 layers thick, the eccentricity of the gauge area is very small (about $0.05mm$) and hence, the sample is assumed to fail under pure shear.

Finally, we perform a tensile test on the Universal Testing Machine. Five samples were prepared for each set of AFP process parameters in this study. The shear type test will result in a sharp failure point if the failure modes are light fiber tear(LFT) or cohesive. Stock-break failure mode will result in the fibers of the tape breaking, this may result in multiple failure points depending on how even the break is. The stock break failure mode indicates that the gauge area was not properly restricted during the manufacturing of the sample or that the sample's fibers were damaged during removal or transport.

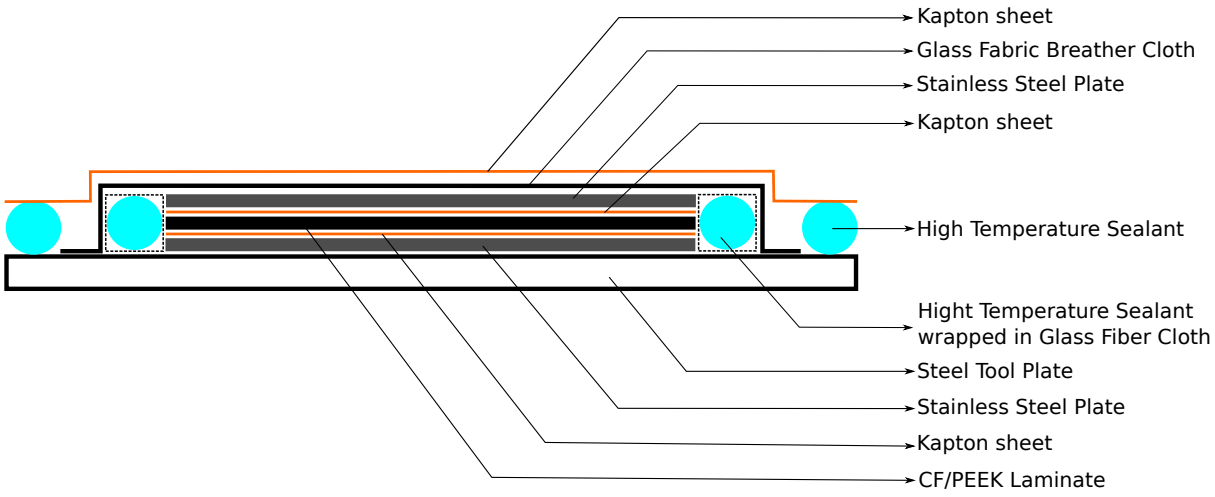

Figure 3.7: Vacuum Bag Scheme used for Reference Samples

3.4.3.1 Reference Sample Manufacturing

To function as a reference for bond strength evaluation through mechanical testing, some samples were manufactured first by using the HGT-assisted AFP process and then re-consolidated in an autoclave. Flat substrate panels were made using the HGT-assisted AFP process according to the procedure described in Section 3.4.3 and cut to size. On this substrate both straight and steered tapes were laid down and the gauge area was limited to a height of $6.35mm$ like all other samples. Since these samples will be re-consolidated in an autoclave before testing, laying down only a single tape, straight or steered, will be insufficient and result in an undesired failure mode (fiber breakage). After some trial and error it was found that a total of six tapes will be safe and reliably result in the desired failure mode (cohesive failure, see Section 3.4.3). The samples were then prepared to be placed in the autoclave by vacuum bagging them. The complete vacuum bag scheme is shown in Figure 3.7 and the various steps involved in this vacuum bagging process have been shown in Figures 3.8 and 3.9.

First, a sheet of Kapton®film was fixed in place using polyimide tape on the steel tool plate. Then, the caul plates that were sized to the laminate being consolidated was placed on top of the Kapton®film. The caul plates were cleaned thoroughly with acetone under a fume hood and then allowed to dry completely before placing them on the Kapton®film. The caul plates were then covered with another film of Kapton®that were sized exactly

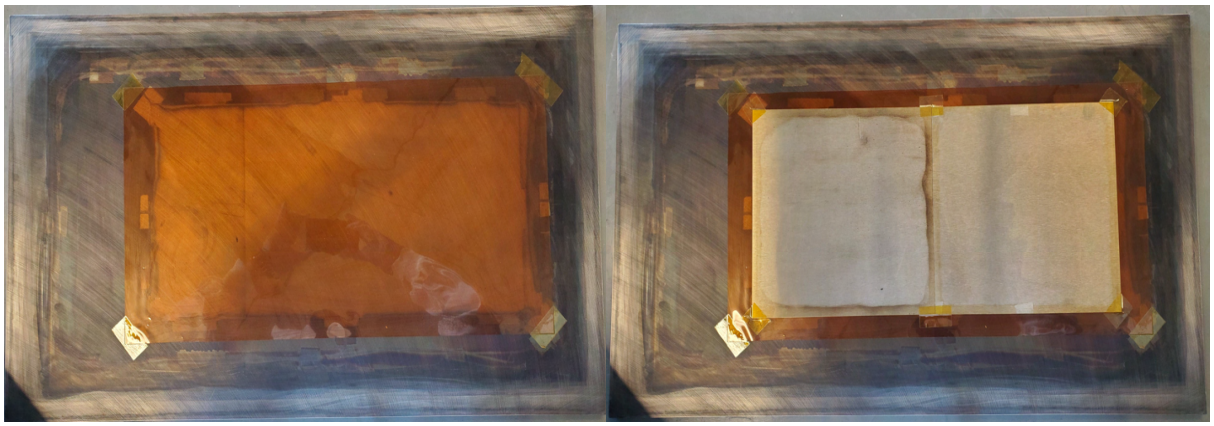

(a) Layer 01 - Kapton®sheet (b) Layer 02 - Stainless steel caul plates

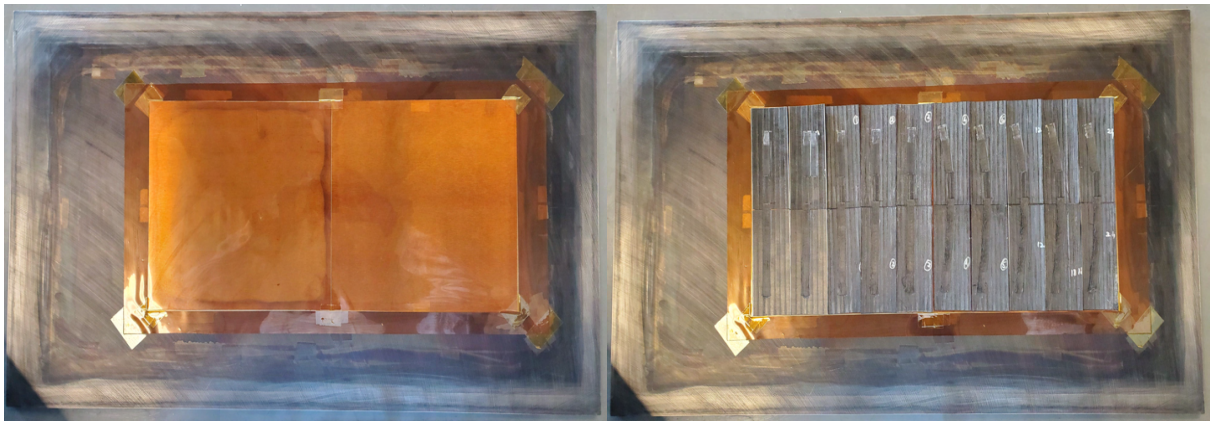

(c) Layer 03 - Kapton®sheet (d) Layer 04 - Test samples

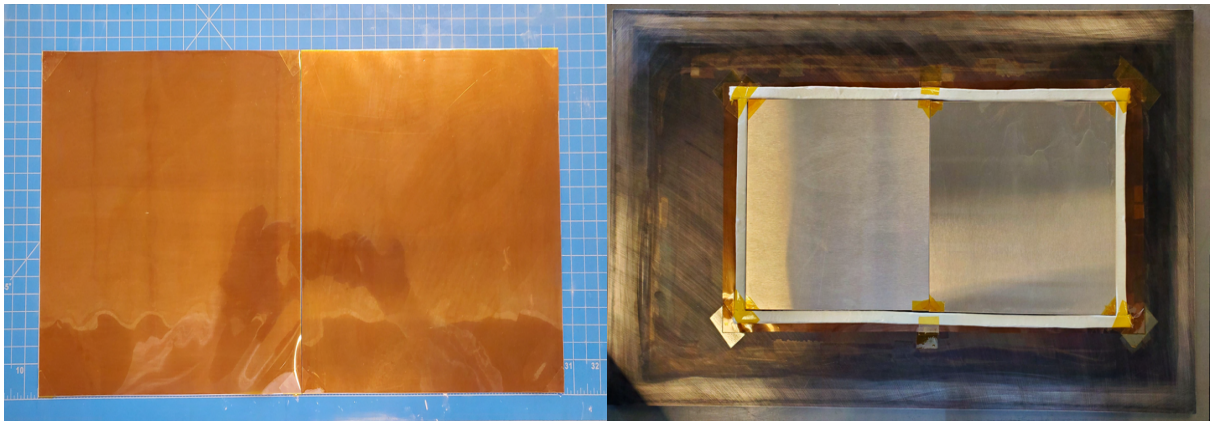

(e) Layer 05 - Kapton®sheet (f) Layer 06 - Stainless steel caul plates

Figure 3.8: Layup procedure for thermoplastic autoclave process-1

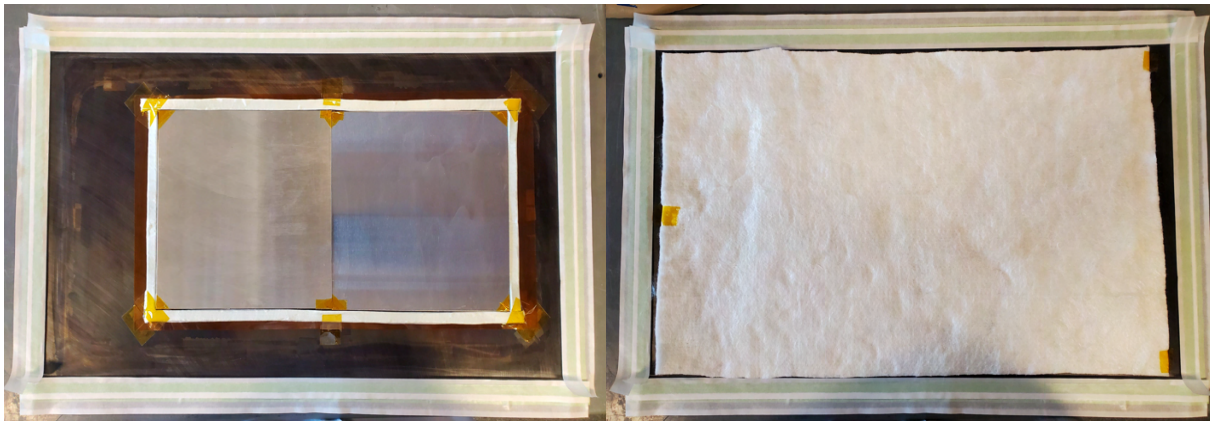

(a) Double selant tape and Dam around layup (b) Glass Fiber breather cloth

(c) Kapton®sheet fitted with vaccuum ports (d) Steel frame to ensure proper seal

Figure 3.9: Layup procedure for thermoplastic autoclave process-2

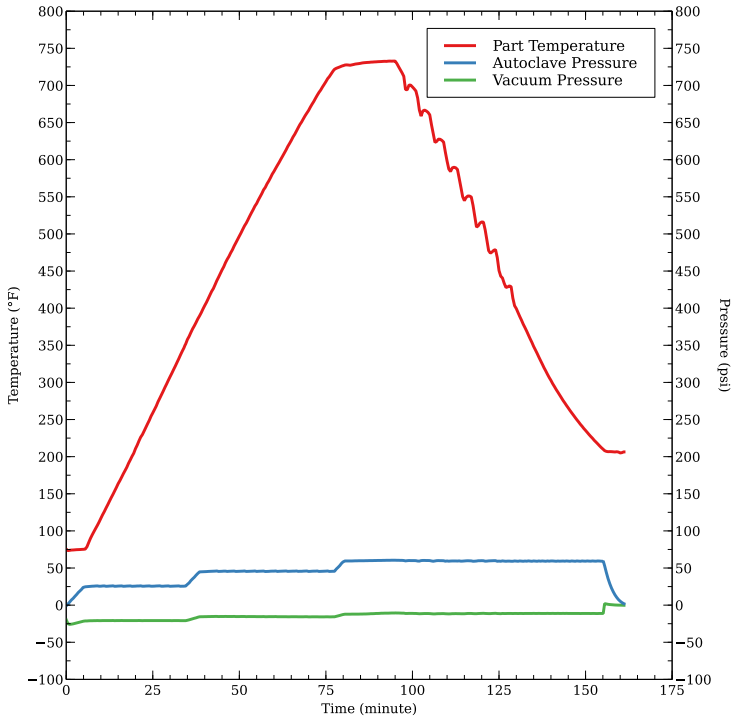

Figure 3.10: Autoclave Thermal Cycle

to fit over the caul plates. This film was coated twice using a Frekote®770-NC release agent to facilitate easy removal of the laminate after consolidation in the autoclave. Ten samples were processed at once by placing them next to each other as shown in Figure 3.8d. Thin strips of Kapton®HN general-purpose polyimide film were used to prevent the two halves of each substrate from fusing together. Another pair of caul plates were prepared and fixed with Kapton®film (See Figure 3.8e). This layer was also coated with release agent as it will be in direct contact with the laminate. The samples were then sandwiched between these Kapton®covered caul plates as shown in Figure 3.8f. Dams were built around the layers using sealant tape that was covered with woven glass fiber cloth to prevent any resin from flowing out (See Figure 3.8f).

Two strips of Airtech's A-800-3G sealant tapes were placed along every edge of the steel tool plate such that were no gaps or leaks along the entire perimeter. Two strips are required since it was found in a previous trial that, at high temperatures, one strip was not sufficient to maintain the vacuum. Care was taken to ensure that the perimeter of the tool plate was entirely clean of any sealant residue from previous trials or experiments. A glass fiber breather cloth was then placed on top of the layup sequence while taking care that it doesn't overlap with the sealant tapes (See Figure 3.9b). The base of the vacuum ports were placed on top of the breather cloth at a sufficient distance away from the tapes to prevent large wrinkles from forming on top of the sealant once the vacuum is applied. Holes were punched according to placement of the vacuum ports in a Kapton®film large enough to cover the whole tool plate. This film was then adhered to the tapes along the entire perimeter while avoiding the formations of any bubbles or wrinkles. The protective films were left on the adhesive tapes until this step to prevent any dust from sticking to the adhesive and thus compromising the vacuum due to poor adhesion. The vacuum ports were then mated with their base with and tightened securely. To withstand the high temperatures, a soft graphite layer acts as the sealant for the vacuum ports instead of rubber.

A steel frame was placed directly on top of the adhesive tape to prevent any leaks by continually applying pressure on them, as shown in Figure 3.9d. Such a frame was

required because, while the adhesive tapes were rated up to $400°C$ they still degrade to a certain extent when used at these temperatures. Since PEEK requires a high processing temperature of $391°C(735°F)$, care was taken so that everything used in the vacuum bagging process was able to withstand that temperature. The sample was then placed in the autoclave and a vacuum of $-81.273kPa(-24inHg)$ was applied to it. The autoclave was then run up to a maximum temperature of $399°C(750°F)$ at a pressure of $413.7kPa(60psi)$ for a dwell time of $20min$ and then cooled down. The thermal cycle used in the autoclave has been shown in the Figure 3.10.

3.5 Results and Discussion

3.5.1 Visual Inspection

Steering a flat thermoplastic prepreg tape can result in some inherent defects such as, buckling along the inner edge due to compression and tape folding along the outer edge due to excessive tension. A visual inspection was carried out to observe such defects caused by steering and to assess the quality of the samples manufactured using different process parameters.

3.5.1.1 Effect of steering radius

From visual observation of sample number 1 to 6(Table 3.1) it was clear for radii equal to or larger than $800mm$ no steering induced defects like buckling and tape folding were observed. At these radii the deviation from a straight path is not large enough to produce defects like tape folding due to tension and/or tape buckling due to compression at the edges of the tape. Observation of sample number 7 to 9 (Table 3.1) with a steering radius of $600mm$ showed some minor tape buckling on the inner radius of the tape while no tape folding on the outer edges of the tape was observed as shown in Figure 3.11a.

Sample number 10 to 12 (Table 3.1) with a steering radius of 400 mm the tape buckling was prominent and observed all along the steered regions of the samples. Some hints of tape folding was also observed on the outer edge of the tape at this radius, shown in

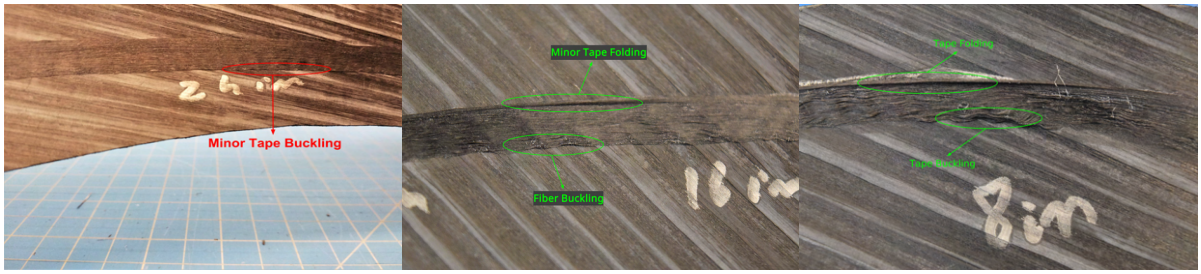

(a) Minor defects at 600mm steering radius (b) Defects at 400mm steering radius (c) Defects at 200mm steering radius

Figure 3.11: Visual inspection of different steering radii

Figure 3.11b. Sample number 13 to 15 (Table 3.1) with the smallest radius of 200mm suffered from both tape buckling at the inner radius and tape folding of the outer radius as shown in Figure 3.11c.

3.5.1.2 Effect of laydown speed

To understand the effects of laydown speed on the steering of AS4/PEEK tape, different speeds from $2.54cm/s$ $(1in/s)$ to $12.7cm/s$ $(5in/s)$ (Table 3.1) were tested on a steering radius of $400mm$. This was because the tape with $400mm$ steering radius showed both continuous fiber buckling and some hints of tape folding. By varying the laydown speed at this radius it would be easier to observe how it affects the steered tape. The temperature and compaction force were kept constant at $875°C$ and $266.89N$ $(60lbs)$ respectively. Observation of sample number 19 to 21 and 21 to 24, with laydown speeds of $5.08cm/s$ $(2in/s)$ and $7.62cm/s(3in/s)$ respectively, showed continuous tape buckling and some hints of tape folding. This was consistent with the observation made for the samples with $400mm$ steering radius in Section 3.5.1.1. However, a significant change to this trend was observed in samples with laydown speeds higher than $7.62cm/s$ $(3in/s)$. Sample number 24 to 27 and 27 to 30, with laydown speeds of $10.16cm/s(4in/s)$ and $12.7cm/s$ $(5in/s)$ respectively, showed only intermittent tape buckling and no tape folding. In case of the laydown speed $12.7cm/s$ $(5in/s)$ it was found that 14.26% of the tape was affected by buckling defects. While in the case of $10.16cm/s(4in/s)$ only 6.2% of the tape was affected by buckling. This is very different when compared to cases at lower speeds with continuous buckling (*e.g.*, Steering radii from $400mm$) where close to 100% of the tape is

(a) Intermittent defects at 4in/s (b) Intermittent defects at 5in/s (c) Poor quality at laydown speed of 1in/s

Figure 3.12: Samples with different laydown speeds steered at $400mm$

affected by buckling. This effect was probably due to the resin not having enough time to melt completely and to bond with the substrate allowing the fibers to shear and not to buckle. Figures 3.12a and 3.12b show the intermittent defects observed.

On the other hand, the low speed of $2.54cm/s(1in/s)$ produced very poor results. This was probably because of the combination of a high temperature of $875°C$ and low speed of $2.54cm/s(1in/s)$ which allowed a large amount of heat to be transferred to the tape. Due to this, the resin melted completely and its viscosity was also reduced to the extent that the fibers had less support during the steering process and were allowed to roll up along the tape width as shown in Figure3.12c. Furthermore, some matrix degradation could have happened due to exposure to high temperature in a longer period of time which led to some matrix poor areas.

3.5.1.3 Effect of repass

Repass was considered as a separate processing parameter to see if it can ameliorate defects caused by the steering of the tape. Observation showed that a repass is very effective in smoothing over any fiber pull up caused by the buckling of the steered tape. However, it must be noted that repass failed to completely smooth over the tape folding observed in the radii of $400mm$ and $200mm$ and may have even caused the folded tape to break at certain locations. Figures 3.13a, 3.13b and 3.13c show the effect of repass on the radius of $200mm$.

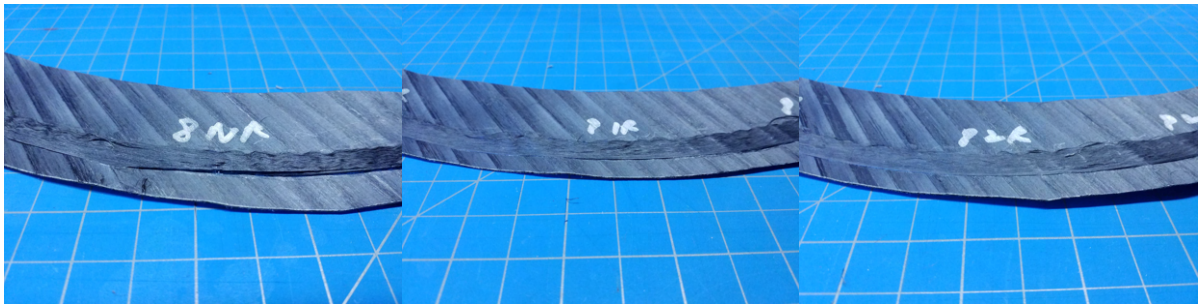

(a) 200mm steering radius with no repass (b) 200mm steering radius with 1 repass (c) 200mm steering radius with 2 repasses

Figure 3.13: Visual inspection of the effect of repass

Table 3.2: Effect of steering radius on the geometry of the tape

Measurement	Radii (mm)	Straight (mm)	SE(±)}	Steered (mm)	SE(±)
Width	1000	9.511	0.045	9.149	0.031
	800	9.532	0.031	9.276	0.020
	600	9.625	0.028	9.300	0.023
	400	9.590	0.026	9.114	0.031
	200	9.653	0.017	8.787	0.048
Thickness	1000	0.117	0.001	0.151	0.002
	800	0.103	0.002	0.138	0.002
	600	0.099	0.002	0.143	0.001
	400	0.106	0.001	0.160	0.002
	200	0.101	0.001	0.188	0.003

3.5.2 Geometrical Analysis

3.5.2.1 Effect of Steering Radius

The summary of the results obtained by measuring the width and thickness of the steered tape in comparison with the straight tape is shown in Table 3.2. The width and thickness of the straight portion of the tapes remained almost constant. The width of the steered portion was found to be consistently lower than straight portion. A similar observation was made in a previous study by Clancy *et al.*, [9]. This is primarily due to the steering which causes the fibers in the tape to move more closer to and even slip on top of each other. This causes the width of the tape to be lesser than what it would be when the tape was laid down in a straight line. Figure 3.14 shows two distinct regions of variation in the width and thickness of the tape. The first region is for samples with steering

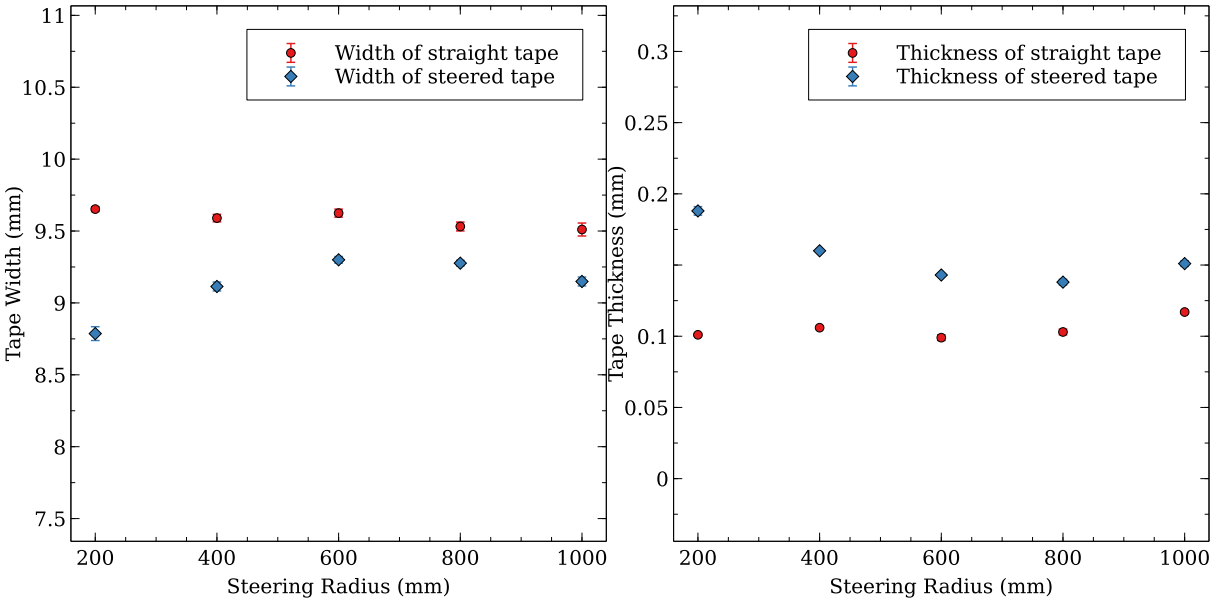

(a) Tape width vs Steering radius

(b) Tape Thickness vs Steering radius

Figure 3.14: Effect of steering radius on the geometry of the tape

radii of 1000mm, 800mm and 600mm (sample number 1 to 9 in Table 3.1) where the widths and thicknesses of these radii remain very close to each other. A second trend observed in the samples 10 to 15 (Table 3.1) with sharper steering radii of 400mm and 200mm. In the latter case, the widths of the steered tapes is further reduced (Figure 3.14a) and their thicknesses increase more sharply (Figure 3.14b) because of the tape buckling and tape folding that occurred at these radii. Analysis of the cross-sectional area of tapes (multiplication of width by thickness) shows a general trend on the effect of steering. Comparing the straight tapes cross-sectional areas with those of steered ones under same process conditions shows that steering increases the tape cross-sectional area. The smaller the steering radii the bigger the increase in the cross-sectional area would be. This trend may be attributed to the defect (void, buckling and tape folding) formation during steering.

3.5.2.2 Effect of Laydown Speed

The summary of the results obtained by measuring the widths and thicknesses of tapes with varying laydown speed is shown in Table 3.3. The width of the both the straight and the steered tape reduces as the laydown speed of the AFP increases. This is because the

Table 3.3: Effect of laydown speed on the geometry of the tape

Measurement	**Speed (cm/s)**	**Straight (mm)**	**SE(±)**	**Steered (mm)**	**SE(±)**
Width	12.17	8.548	0.052	8.048	0.051
	10.16	8.731	0.046	8.145	0.046
	7.62	8.910	0.040	8.461	0.039
	5.08	9.604	0.034	9.263	0.061
Thickness	12.17	0.158	0.006	0.213	0.006
	10.16	0.120	0.003	0.158	0.007
	7.62	0.115	0.005	0.158	0.008
	5.08	0.117	0.004	0.157	0.005

resin has less time under the consolidation roller to be squeezed and spread in the width direction. Steering also further decreases the width of the laid down tape. However, in the study by Clancy *et al.*, [9] on steering of thermoplastic tape with a Laser-assisted ATP, the width of the straight tape remained unchanged upto a laydown speed of $16.67cm/s$. For the steered portion of the tape the width of the tape remained almost constant until the laydown speed of $10cm/s$ but had a sharp decrease at the speed of $16.67cm/s$ [9]. The thickness almost remains a constant for the straight region despite the width of the tape reducing with increasing speed but there is a 35% increase at the speed of $12.7cm/s$ ($5in/s$). The thickness of the steered layer is higher than the straight portion at every speed. The variation of the thickness along each of the steered samples is very similar to the straight samples with a sharp increase at the laydown speed of 5in/s. This observation for the steered portion is consistent with the study by Clancy *et al.*, [9]. The variation of width and thickness are visualized in the graphs shown in Figure 3.15.

3.5.2.3 Effect of Repass

During the trials where the laydown speed and steering radius were varied, it was observed that the fiber pull-up due to the buckling of the tape occurred in some of the cases. Repass was applied to the steered tape to see if it could ameliorate these steering induced defects. The repass was done at same HGT temperature and consolidation force (*i.e.*, $875°C$ and $266.89N$). The results of the geometrical analysis done on samples that underwent repass are summarized in Table 3.4. The first repass increases the width and reduces

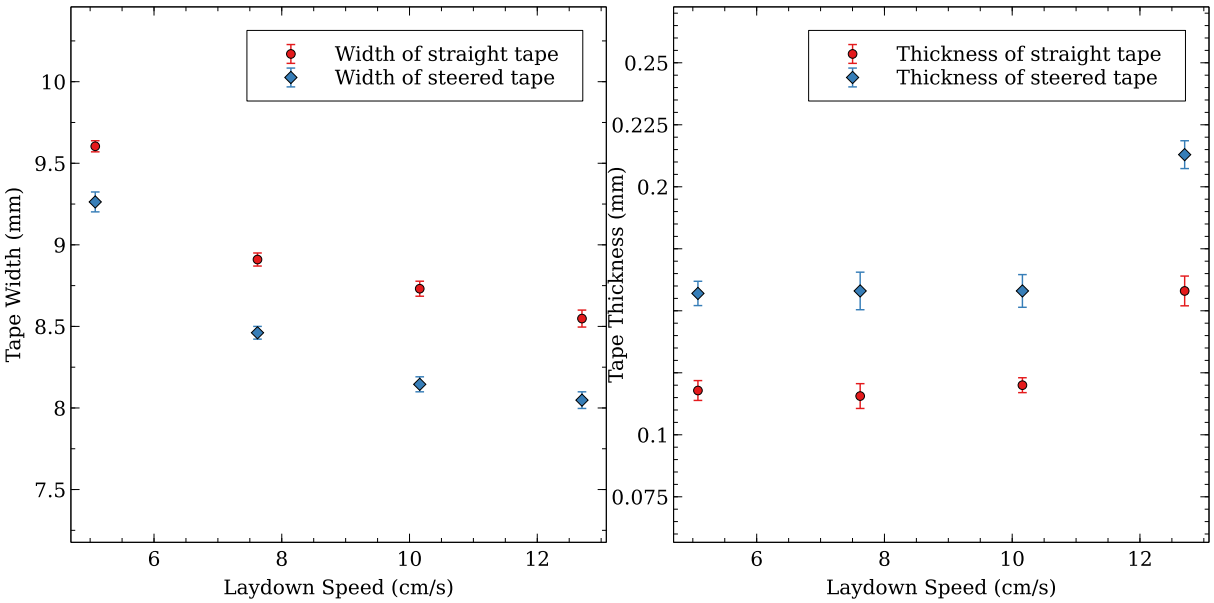

(a) Tape width vs Laydown speed (b) Tape thickness vs Laydown speed

Figure 3.15: Effect of laydown speed on the geometry of the tape at a steering radius of $400mm$

Table 3.4: Effect of repass on the geometry of the tape

Radii (mm)	**No. of Repass**	**Width (mm)**	**SE(±)**	**Thickness (mm)**	**SE(±)**
600	0	9.180	0.039	0.134	0.002
	1	9.734	0.034	0.090	0.001
	2	10.146	0.033	0.089	0.001
400	0	8.945	0.035	0.156	0.002
	1	9.058	0.033	0.104	0.003
	2	9.109	0.030	0.093	0.002
200	0	8.111	0.088	0.200	0.005
	1	8.691	0.049	0.130	0.003
	2	8.788	0.050	0.105	0.002

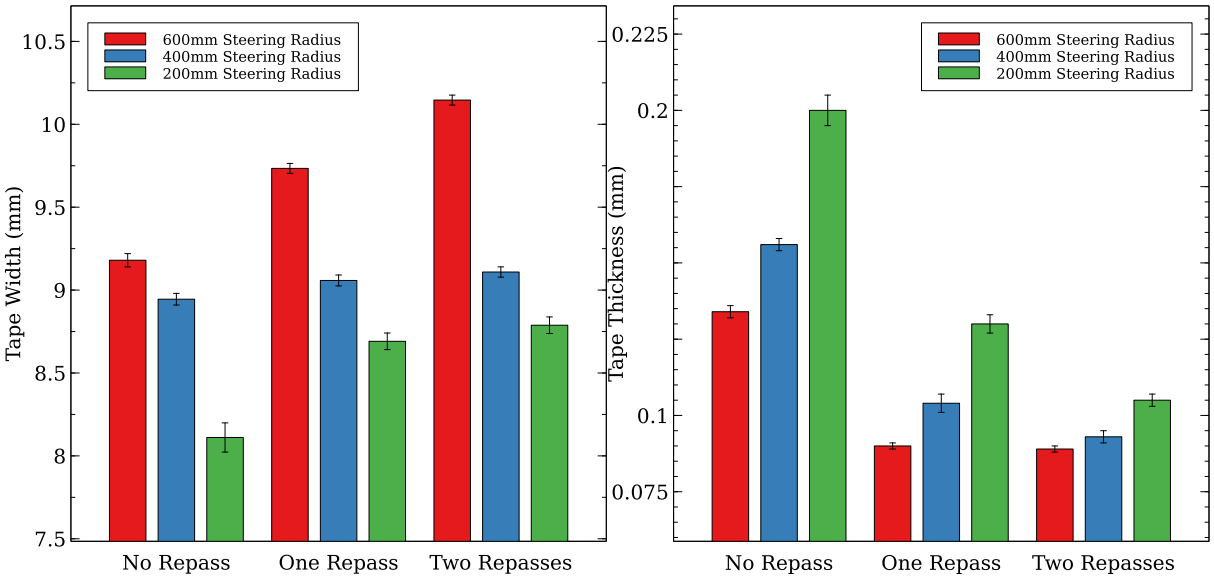

(a) Tape width vs No. of repass

(b) Tape thickness vs No. of repass

Figure 3.16: Effect of repass on the geometry of the tape

the thickness. However, the second repass does not lead to a considerable change in the tape's dimensions in most cases; the change in the width at the steering radius of $600mm$ is the only exception to this trend. These variations are represented in the plots shown in Figure 3.16.

3.5.3 Microscopic Analysis

3.5.3.1 Effect of steering radius

The microscopic analysis was performed on each sample to see how well the bond of the steered layer was consolidated with the substrate and to see how the fibers were distributed. For higher steering radii like $1000mm$ and $800mm$ no buckling or tape folding observed in the visual inspection. This was also reflected in the microscopic analysis showing good consolidation and no voids due to the steering induced defects as shown in Figure 3.17a. However, for smaller steering radii like $400mm$ and $200mm$, there were void formations at the bond line (Figure 3.17b) and in case of the $200mm$ steering radius the tape folding can be clearly observed in Figure 3.17c.

Different types of edge formations were characterized by Lawal *et al.*, [65] and were also observed by M.A. Khan[56], as shown in Figure 3.18a. The study by Khan [56]

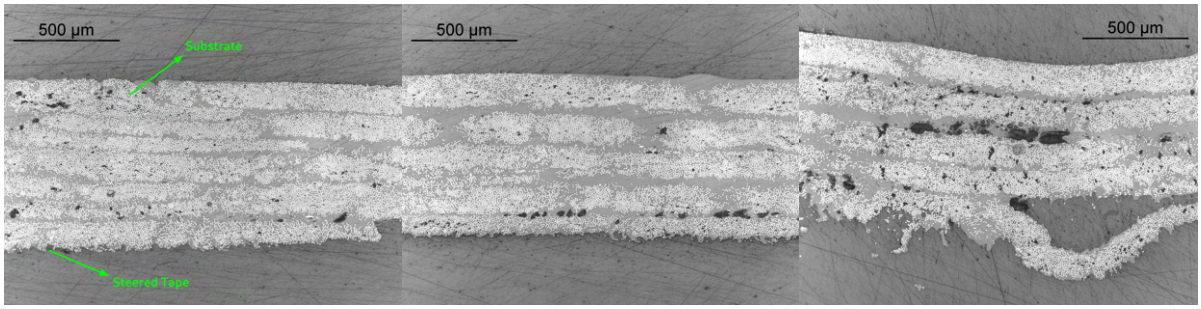

(a) Good bond consolidation at 800mm radius (b) Voids at interface - 400mm radius (c) Tape folding at 200mm radius

Figure 3.17: Effect of steering radius

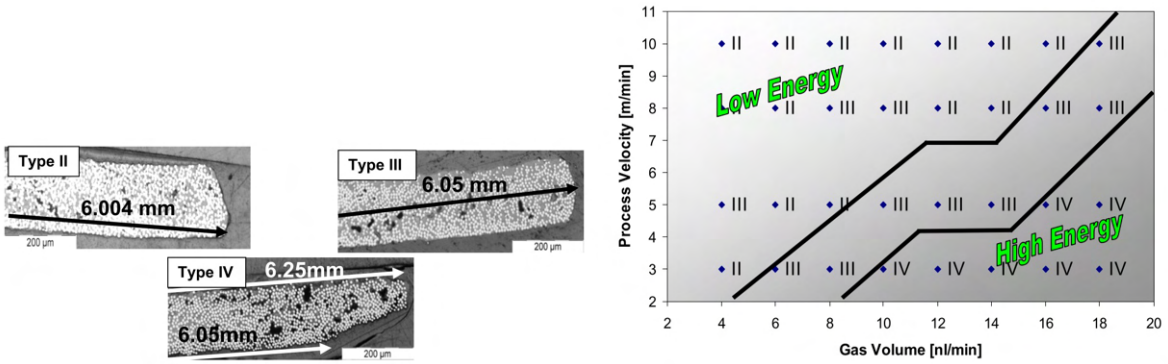

(a) **Types of edges formed** (b) **Edges formed at different energy levels**

Figure 3.18: Thermoplastic tape edge formations at various energy levels[56]

investigated the edge formations of a thermoplastic tape due to the energy imparted by a hot gas torch. The energy imparted was considered to be a function of the laydown speed and the hot gas flow rate. As seen in the graph shown in Figure 3.18b high speed and low gas flow rates resulted in lower energy being imparted and type II edges were formed. In our study, a similar type II edge was observed at a steering radius of $800mm$ and speed of $5.08cm/s$ $(2in/s)$, as shown in Figure 3.17a.

3.5.3.2 Effect of laydown speed

During visual inspection is was seen that for the tape steered at $400mm$ radius at speeds of $10.16cm/s$ $(4in/s)$ and $12.7cm/s$ $(5in/s)$ the defects were no longer continuous along the length of the tape, it was intermittent and defects only occupied a small percentage of the length of the tape. When observed under a microscope the tapes appeared well consolidated and without significant defects at all the speeds tested (Figure 3.19). This is

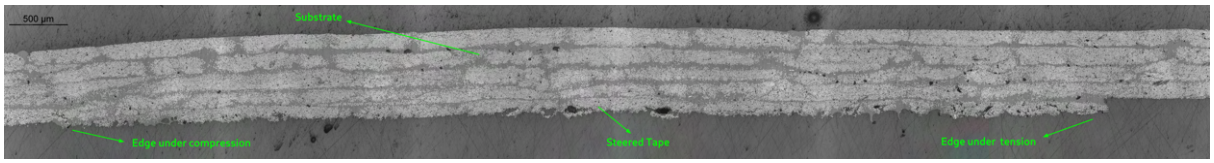

Figure 3.19: Tape steered at $10.16cm/s$ with a radius of $400mm$ (HGT temp $875°C$; Compaction $266.89N$)

consistent with the observation made in the Laser-assisted ATP steering study by Clancy *et al.*, [9]. Only in the case of 2in/s (Figure 3.17b) some void formation was found on the bond line. Clear conclusions regarding the effect of laydown speed on steered tapes cannot be drawn using micorscopic analysis alone, further mechanical testing is required, see section 3.5.4.2.

3.5.3.3 Effect of repass

To see if the defects caused by tape steering can be ameliorated, samples of $600mm$, $400mm$ and $200mm$ were treated with 1 and 2 repasses. The laydown speed was $5.08cm/s$ $(2in/s)$ and HGT temperature and compaction force were $875°C$ and $266.89N(60lbs)$, respectively, as per Table 3.1. Figures 3.20a, 3.20b and 3.20c show the effect of repass on a steered tape. As observed during the visual inspection, the buckling defects are smoothened by repass. However, even after two repass treatment, the tape folding is not rectified by repass and may have caused the folded edge to break (Figure 3.20f).

3.5.4 Mechanical Testing

3.5.4.1 Effect of Steering Radius

Samples of different steering radii ranging from $1000mm$ to $200mm$ were manufactured and tested as described in Section 3.4.3. For each steering radius tested, five samples were manufactured and tested based on the new shear type test as explained in Section 3.4.3. To study the effect of steering radius on the bond strength, all samples were manufactured with a constant laydown speed of $5.08cm/s$ $(2in/s)$, compaction force of $266.89N$ $(60lbs)$, HGT temperature of $875°C$ and HGT flow rate of $0.06m^3/min$. To serve as a reference, two sets of straight samples were also manufactured using the AFP, with the same process

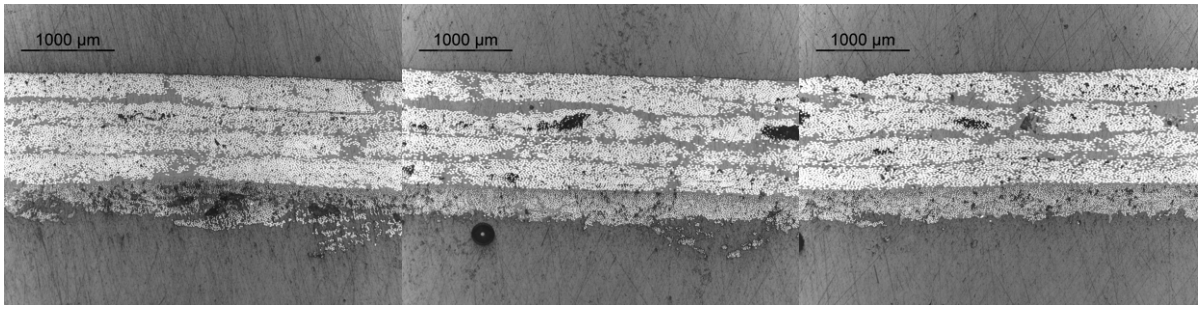

(a) Buckling defects without repass (b) Buckling defects with 1 repass (c) Buckling defects with 2 repasses

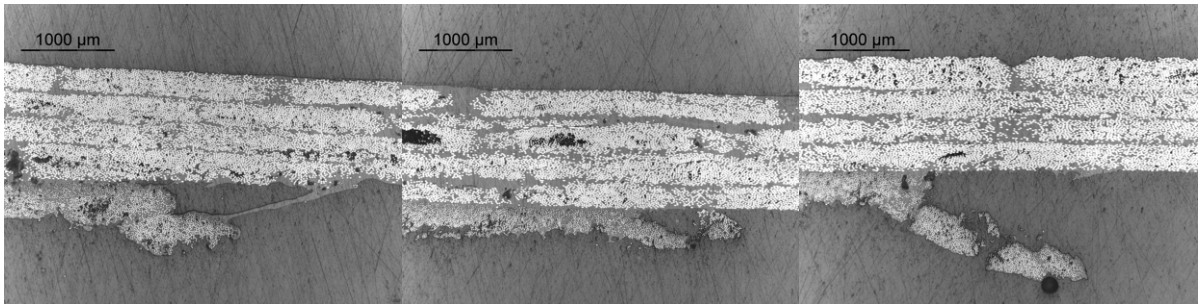

(d) Outer edge under tension without repass (e) Outer edge under tension with 1 repass (f) Outer edge under tension with 2 repasses

Figure 3.20: Effect of repass on a steering radius of 400mm (HGT temp 875°C; Compaction 266.89N)

parameters mentioned above. One set was directly tested using the proposed mechanical test (Section 3.4.3). The other set was post consolidated using an autoclave as per the procedure described in the Section 3.4.3.1 and then tested using the new shear type test. The summary of the mean bond strength obtained from the samples, and their failure modes, are shown in Table 3.5 and represented in graphical form in Figure 3.21.

The results show that, with these process parameters, steering from a radii of 1000mm down to 400mm does not affect the bond strength negatively, and the bond strength of

Table 3.5: Bond strength results for different steering radii

Radius (mm)	**Bond Strength (MPa)**	**SE(±)(MPa)**	**Failure Mode**
1000	21.57	1.12	LFT
800	20.64	1.37	LFT
600	21.15	0.80	LFT
400	21.86	1.25	LFT
200	15.01	0.45	LFT
Straight Tape (In-situ)	21.409	0.77	LFT
Straight Tape (Autoclave)	48.86	1.27	Cohesive

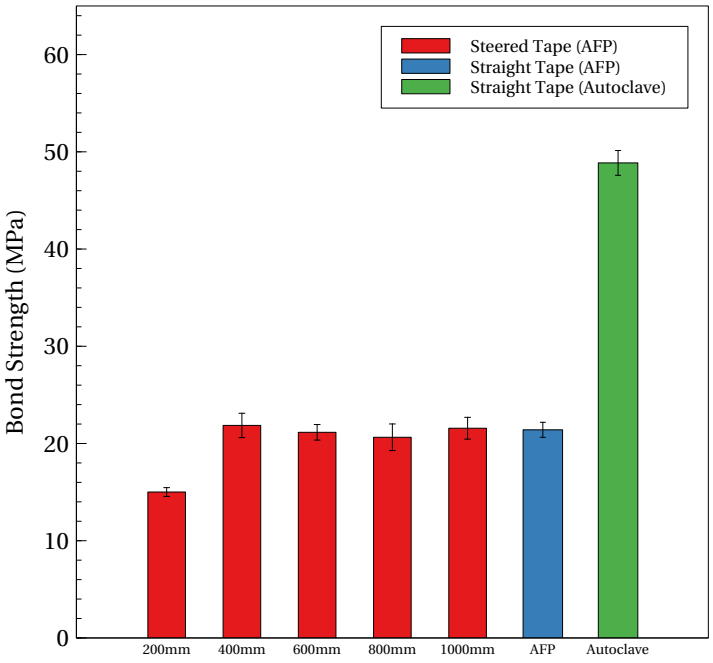

Figure 3.21: Steering Radius vs Bond Strength

the steered tapes are very comparable to the results obtained for a straight tape (without post treatment in autoclave). These results are interesting as it indicates that despite some defects observed in $600mm$ and $400mm$ tapes, the process parameters used are sufficient to provide a bonding as good as the straight tape made by the AFP alone. However, this is only true until a steering radius of $400mm$, after which there is sharp fall in the bond strength at a steering radius of $200mm$. This is mainly due to the prominent tape folding observed at this radius resulting in a poor bond along the outer edge of the tape. Another important observation is that the bond strength of samples post treated in the autoclave ($48.86MPa$) is more than two times of those made by in-situ consolidation of AFP ($21.409MPa$). This large difference is due to the fact that during the in-situ consolidation, the molecules of the thermoplastic matrix do not have enough time to diffuse into the substrate and make a perfect bond as is the case for autoclave treated samples. Figure 3.22 shows a sample of $400mm$ steering radius that failed by the light fiber tear failure mode.

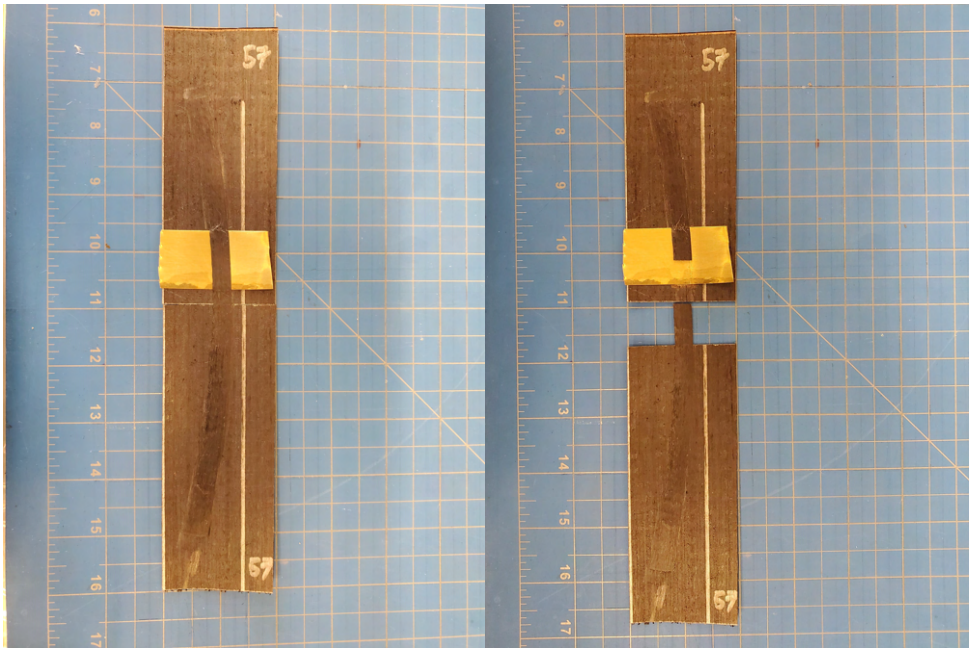

(a) Sample before testing (b) Sample failed by light fiber tear

Figure 3.22: Mechanical Test Samples at 400mm Steering Radius

Table 3.6: Bond strength results for different laydown speeds

Laydown Speed (cm/s)	Bond Strength (MPa)	SE(±)(MPa)	Failure Mode
5.08	21.86	1.25	LFT
7.62	18.88	1.44	LFT
10.16	15.18	0.88	LFT
12.7	10.43	1.26	LFT
Straight Tape (In-situ)	21.409	0.77	LFT
Straight Tape (Autoclave)	48.86	1.27	Cohesive

3.5.4.2 Effect of Laydown Speed

To study the effect of laydown speed on the bond strength a steering radius of $400mm$ was chosen and samples were manufactured as described in Section 3.4.3.

A consolidation force of $266.89N(60lbs)$, HGT temperature of $875°C$ and HGT flow rate of $0.06m^3/min$ were kept constant for all the samples manufactured at different laydown speeds. Five samples for each laydown speed was manufactured and straight tapes laid down at a speed of $5.08cm/s(2in/s)$ and then post consolidated in an autoclave were used as a reference. The summary of the results obtained by testing all the samples of different laydown speeds is shown in Table 3.6 and represented in graphical form in Figure

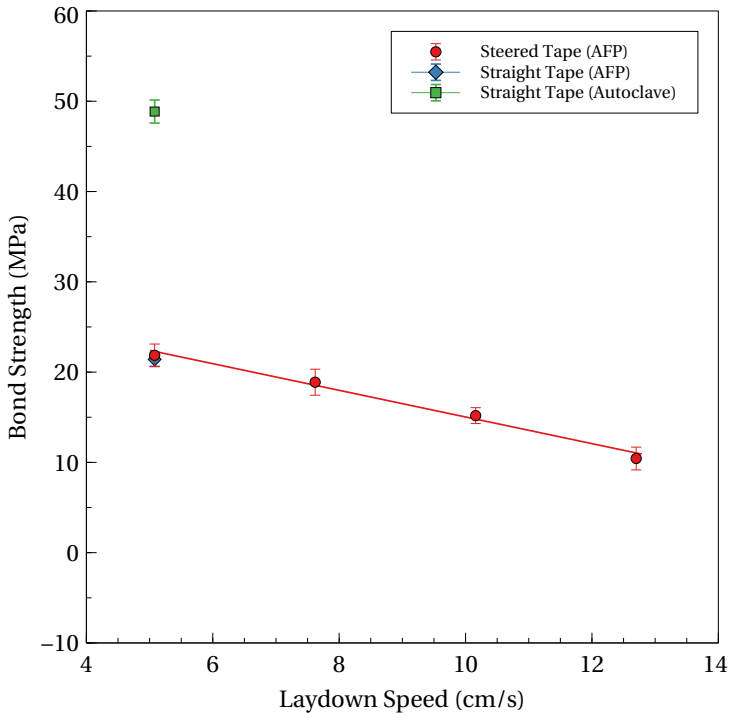

Figure 3.23: Laydown Speed vs Bond Strength

3.23. The test results indicates that the bond strength has an inversely linear relationship with the laydown speed when all the other process parameters are kept constant. This relationship can be observed clearly in Figure 3.23. This is very similar to what is observed in the case of unidirectional tapes [59]. This behaviour of decreasing bond strength with increasing laydown speed was because the incoming thermoplastic tape did not have enough time under the HGT and compaction roller to melt and consolidate with the substrate. This insufficient consolidation resulted in a poor bonding between the incoming tape and the substrate.

3.5.4.3 Effect of Substrate Angle

To investigate the effect of the substrate angle on the bond strength, substrates were made such that the top layer forms the angles of 0°, 30°, 60° and 90° with the gauge area of the tape. To test whether steering affects the bond adversely in such cases samples were made for both straight and steered tapes. Samples were manufactured at a laydown speed of $5.08cm/s(2in/s)$, under $266.89N(60lbs)$of consolidation pressure, $875°C$ of HGT temperature and a HGT flow rate of $0.06m^3/min$. For the steered samples a radius of

Table 3.7: Bond strength results for different substrate angles

Type	Substrate Angle	Bond Strength (MPa)	SE(±)	Failure Mode
Steered	0	20.5015	0.900	LFT
	30	17.8231	0.920	LFT
	60	16.7866	0.657	LFT
	90	13.1901	0.789	LFT
Straight	0	19.4347	1.157	LFT
	30	16.0450	0.760	LFT
	60	14.6370	2.085	LFT
	90	14.6288	1.509	LFT
Straight Tape (Autoclave)	0	48.86	1.27	Cohesive

400mm was chosen as in Section 3.5.4.2.

The test results obtained for steered and straight tapes with different substrate angles have been summarized in Table 3.7 and represented in graphical form in Figure 3.24. The results show a clear inversely linear relationship between the Bond Strength and substrate angle for both the steered and straight tapes. These results agree with another study by Grefe *et al.*, [66] that investigated the effect of fiber orientation on lap shear strength and found that the highest bond strength was at 0° and descended to the lowest at 90°. As it was shown in Section 3.5.4.1, at the radius of $400mm$ and above no appreciable difference in the bond strength between the straight and the steered tapes was observed. This implies that that one can perform fiber steering on any substrate angle without compromising on the bond strength. However, it should be noted that for radii below $400mm$ the effect of the radius will be more dominant due to the tape folding defect causing the bond strength to suffer.

3.6 Conclusion

In this chapter, the ability of HGT-assisted AFP to steer $6.35mm$ ($0.25in$) wide CF/PEEK tapes was investigated experimentally. The effect of different parameters including steering radius, laydown speed, number of repasses and substrate angle on the geometry and bond strength was investigated.

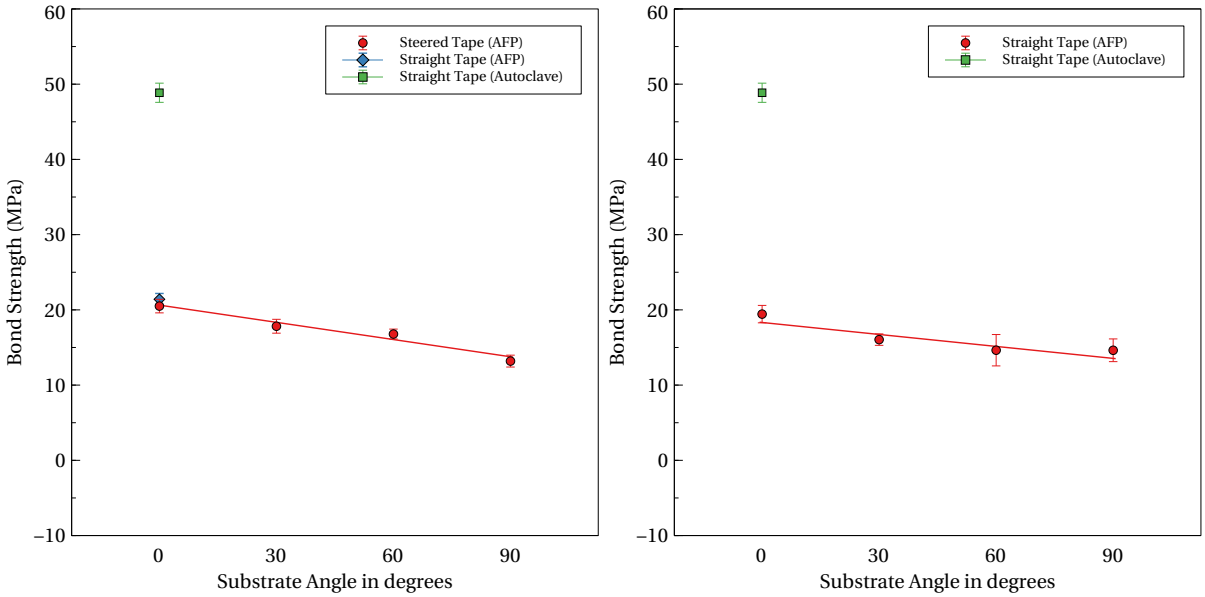

(a) **Steered Tape** (b) **Straight Tape**

Figure 3.24: Substrate Angle vs Bond Strength

The tapes were steered at different radii and no considerable steering induced defects were observed until the radius of $400mm$. At a radius of $400mm$ some tape buckling and some hints of tape folding were observed. The smallest radii of $200mm$ suffered the most defects due to the steering as both tape buckling and tape folding were dominant. It was found that steering induced defects are continuous along the tape when laid down at a speed of $5.08cm/s$ ($2in/s$) and $7.62cm/s$ ($3in/s$). At higher speeds of $10.16cm/s$ ($4in/s$) and $12.7cm/s$ ($5in/s$) the defects were intermittent. Optical microscopy showed that the outer edges of tapes that were steered at $400mm$ and $200mm$ radii were poorly bonded due to the tape folding. These tapes also experienced some fiber pull up due to the tape buckling. Repasses were attempted on these tapes to resolve these defects and it was found that a single repass was sufficient to smoothen most of the fiber pull up. However, the tape folding was not fixed even after two repasses and resulted in the breaking of the folded edge of the tape.

A specially devised mechanical test, which was inspired by the lap shear test, was used to test the bond strength of the steered CF/PEEK tapes with a CF/PEEK substrate that was also manufactured by the HGT-assisted AFP. Some of the AFP-made samples were post consolidated in the autoclave to provide a reference value for the bond strength.

Testing the bond strength of different steering radii and comparing it with straight tapes laid down with identical process parameters yielded interesting results. The test results indicate that bond strength of the steered tapes up to a radius of $400mm$ was as good as the straight tapes. However, at the radius of $200mm$ there was a sharp fall in the bond strength. The severe tape folding prevalent at this radius is believed to be the primary cause of this reduction in the bond strength. Another important observation was that the bond strength of AFP in-situ consolidated samples were roughly less than half those post consolidated in the autoclave.

It was also found that the bond strength decreases linearly with increasing laydown speed by testing four different laydown speeds at a steering radius of $400mm$. The tapes steered at speeds of $10.16cm/s$ ($4in/s$) and $12.7cm/s$ ($5in/s$) showed poor bond strength despite having much lower steering induced defects. This highlighted the importance of choosing proper process parameters to allow sufficient heat transfer to take place to melt the thermoplastic resin completely and bond well with the substrate. The bond strength at higher speeds may be improved by using a higher gas flow rate or higher hot gas temperature. The effect of substrate angle was also investigated and the results showed that the bonding was strongest at the substrate angle of $0°$ and weakest at $90°$.

This work gives us a clear understanding of the ability of the HGT-assisted AFP process to perform fiber steering. However, a more detailed study is required to fully understand the role of substrate fiber angle on a steered tape. Future work in this field would be to tackle other issues in the manufacturing VAT laminates such as gaps and overlaps.

Chapter 4

Analytical Model

In this chapter, the analytical model that was used to predict the critical steering radius at which fiber buckling occurs has been described in detail. First, in Section 4.1 the mechanism by which the fiber buckles during the steering process has been explained. In Section 4.2, Timoshenko's Bar on a Elastic foundation [17] model is described and the derivation of the critical buckling load has been shown. Following that in Section 4.3, Dow and Rosen's analytical model [67] for fiber microbuckling has been described and the expressions for critical buckling stress and strain have been re-derived. In Section 4.4, Campbell's *et al.*, [68] approach to fiber microbuckling has been explained and his derivation of the expressions of critical buckling stress, strain and wavelength have been shown. Following that in section Section 4.5, Wang's *et al.*, [69] approach that combines both Dow-Rosen and Campbell models for microbuckling has been described.

4.1 Mechanism of Fiber Buckling

Buckling is a defect that is inherent in the process of steering a composite prepreg tape whether it is thermoset or thermoplastic. Buckling due to steering can happen in two ways: in-plane and out-of-plane. In the case of thermoset prepreg, the buckling may happen in-plane or out-of-plane depending on the steering radii and process temperature [27]. As the semi-cured thermoset matrix provides good support to the fibers, at smaller steering radii (See Figure 4.1a) it is easier for the tape to overcome the tackiness or

(a) Thermoset tape bucking at $558mm$ [27] (b) Thermoplastic tape buckling at $400mm$

Figure 4.1: Thermoset and thermoplastic tape buckling

adhesion with the substrate and buckle out-of-plane to relieve the bending stress caused by steering. In the case of in-situ consolidated thermoplastic composite tapes, the buckling always occurs in-plane. Once the thermoplastic tape passes under the nip point its temperature begins to fall rapidly [63]. The fiber buckling occurs at this time of rapid cooling where the resin transforms from a melted liquid state to a solid state. The temperature at this time is below the melting point but above glass-transition temperature of the resin, thus, making it 'soft'. This 'soft' resin allows the fibers along the inner-edge of the tape to always buckle in-plane when the tape is steered along a radius.

Timoshenko's bar on an elastic foundation forms the basis for the microbuckling of a fiber that is surrounded by a matrix [17]. In his derivation, Timoshenko focuses on the energy stored in the normal elastic deformation of the springs that represents the elastic foundation. Using the energy method, he derives an expression for the critical load by equating the work done by the compressive force to the energy stored in the buckled bar and in the deformation of the elastic foundation (See Section 4.2). While this is a great starting point, it is insufficient to describe the microbuckling of fibers in a matrix as it only considers a single bar and not a system of bars, which represents a bundle of fibers.

Dow and Rosen [67] expanded on Timoshenko's model for composite materials by considering fibers surrounded by matrix and the two different modes by which the fibers buckle when under compression. Like Timoshenko, Dow and Rosen also used the energy method to arrive at an expression for the critical buckling load. For the fiber matrix

arrangement they followed a unit cell approach where the depth of a unit cell was assumed to be one unit. They also considered two modes of fiber buckling, shear mode (in-phase) and extension mode (out-of-phase). By deriving the expression for the critical stress for both shear and extension modes, they were able to find that for composites with fiber volume fractions higher than 0.6 the shear mode of buckling had a lower critical load making it the most probable mode of buckling for such composites (See Section 4.3).

Campbell *et al.*, [68] drew on Timoshenko and Dow-Rosen's work to derive expressions for the critical stress, strain and wavelength. They investigated the microbuckling of fibers in Elastic Memory Composites (EMC) where the composites are required to be folded and stored in small places until deployment. Unlike Dow and Rosen who investigated the microbuckling of fibers in epoxy composites that were being cured, the resins in EMCs are softer in nature when heated above T_g as they are bent. The wavelengths obtained by using the classical derivations of Timoshenko and Dow-Rosen did not match the wavelength of buckling in EMCs showing that the mechanism involved is slightly different. Campbell's approach to describe the mechanism involved in the microbuckling of fibers can be divided into two parts: 1- to locate the neutral surface once the fibers have microbuckled and 2- to derive the critical loads and wavelength of the buckled fibers. To locate the neutral surface Campbell *et al.*, assumed a material model for the EMC such that the buckled fibers contribute very little to the stiffness beyond a critical strain, thus, moving the neutral surface closer to fiber under tension. Then, they apply the equilibrium condition to the normal stress across the cross-section to find an expression for α which gives the location of the neutral surface in the y-coordinate. To obtain the expression for the critical wavelength Campbell *et al.*, compared the shear strain energy stored in the matrix with the energy stored in the foundation in Timoshenko's bar on an elastic foundation. Then, by using the modulus of the matrix and a simplified expression of Timoshenko's critical load, they derived an expression for the critical load and strain of the fibers (See Section 4.4). A major difference between Dow-Rosen and Campbell is how the describe they shear strain that the matrix experiences. Dow-Rosen assumed the shear strain to be $\left(1 + \frac{d_f}{2c}\right) \frac{du_y}{dx}$ while Campbell *et al.*, considered it to be $\frac{du_y}{dx}$. This

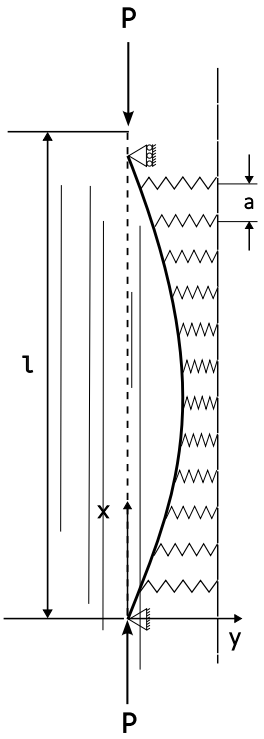

Figure 4.2: Bar on elastic foundation [17]

difference arises because Dow-Rosen considered the effect of the neighbouring fiber on the matrix while Campbell *et al.*, considered the effect of only one fiber.

Wang *et al.*, [69] argued that expression for critical load derived by Campbell *et al.*, [68] cannot be correct, despite its close agreement with the experimental results, as it suggests that the critical load for microbuckling falls with increasing fiber volume fraction. To rectify this Wang *et al.*, considered the effect of the neighbouring fiber like Dow-Rosen when describing the shear strain of the matrix. After that they follow a similar procedure to Campbell *et al.*, to derive expressions for the critical wavelength, load and strain (See Section 4.5).

4.2 Buckling of a bar on elastic foundation - Timoshenko formulation

Timoshenko's buckling of a bar on an elastic foundation (see Figure 4.2) is a good starting point to build an analytical model that describes the buckling of fiber when surrounded by a soft matrix [17]. In this case, the bar would represent the fiber and the elastic

foundation would represent the soft thermoplastic matrix. Timoshenko's[17] derivation of the critical buckling load of a bar on an elastic foundation has been repeated here for reference.

The action of a continuous medium on the bar can be replaced by a series of equally spaced elastic supports.

Let α be the spring constant of each support, a be the distance between the supports, and β be the modulus of the foundation, then,

$$\beta = \frac{\alpha}{a} \tag{4.1}$$

Where β has the dimensions of force/length^2. It tells us how much reaction the bar receives from the foundation for a unit deflection. The deflection curve of the buckled bar with hinged ends can be represented using the Fourier sine series,

$$u_y = a_1 sin\left(\frac{\pi x}{l}\right) + a_2 sin\left(\frac{2\pi x}{l}\right) + a_3 sin\left(\frac{3\pi x}{l}\right) + \dots \tag{4.2}$$

Where, a_1, a_2, a_3... etc. are the amplitudes of the buckled bar, and l is the length of the bar (See Figure 4.2). Each term satisfies the end conditions of the bar and different terms are superimposed to find the true deflection of the bar. The strain energy of the system is stored in the deflected bar and the elastic foundation. First, we consider the strain energy stored in the bar. The strain energy stored in a buckled bar is derived from the expression used for the strain energy stored in a beam under pure bending. For a beam under pure bending (See Figure 4.3a) the angular displacement is given by [70],

$$\phi = \frac{Ml}{EI_z} \tag{4.3}$$

Where, M is the bending moment of the bar, E is the elastic modulus of the bar's material, and I_z is the moment of inertia of the bar's cross-section. The strain energy, U, due to the moment acting on the beam is,

$$\Delta U = M\frac{\phi}{2} \tag{4.4}$$

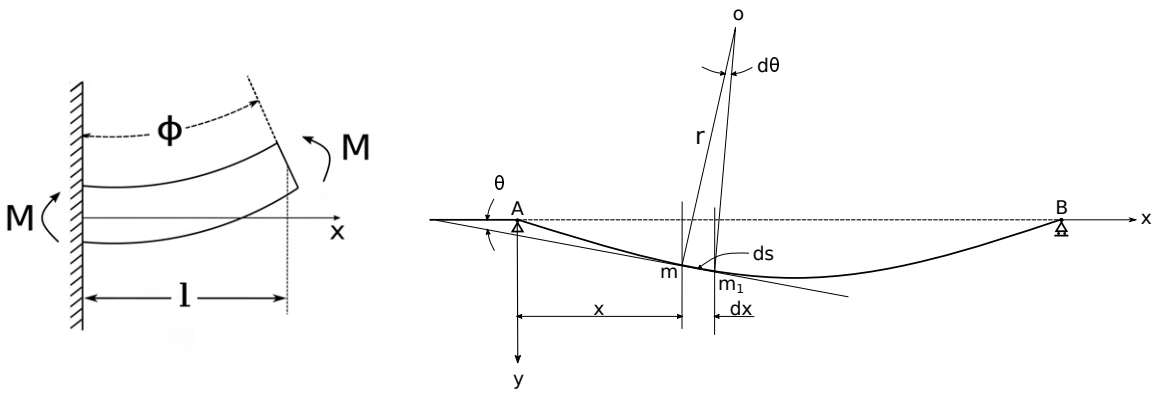

(a) Angular displacement (b) Deflection of a beam

Figure 4.3: Timoshenko's pure bending of a beam [70]

The strain energy can also be written as,

$$\Delta U = \frac{M^2 l}{2EI_z} \quad \text{or} \quad \Delta U = \frac{\phi^2 EI_z}{2l} \tag{4.5}$$

The strain energy stored between two adjacent cross sections is given by,

$$dU = \frac{M^2 dx}{2EI_z} \quad \text{or} \quad dU = \frac{(d\phi)^2 EI_z}{2dx} \tag{4.6}$$

To obtain the strain energy of the bar in terms of dy and dx, consider the geometry of a deflected beam shown in Figure 4.3b. Let m and m_1 be adjacent cross sections on the beam at a distance of ds. If θ is the angle made by the tangent at m, then the angle made by the normals at m and m_1 at the centre of curvature is $d\theta$. The radius of curvature, r, is given by,

$$\left|\frac{d\theta}{ds}\right| = \frac{1}{r} = \frac{M}{EI_z} \tag{4.7}$$

For small beam displacements we can assume that,

$$ds \approx dx \quad \text{and} \quad \theta \approx \tan\theta = \frac{du_y}{dx} \tag{4.8}$$

then the radius of curvature can be written as,

$$\frac{1}{r} = \left|\frac{d\theta}{ds}\right| = \left|\frac{d^2 u_y}{dx^2}\right| \tag{4.9}$$

and the angular displacement between two adjacent cross sections ($d\theta$) of the bar will be,

$$d\theta = \frac{dx}{r} = \left|\frac{d^2u_y}{dx^2}\right| dx \tag{4.10}$$

The total strain energy stored in the bar along its length is,

$$\Delta U = \int_0^l \frac{M^2 dx}{2EI_z} \quad \text{or} \quad \Delta U = \int_0^l \frac{EI_z}{2}\left(\frac{d^2u_y}{dx^2}\right) dx \tag{4.11}$$

Thus, the strain the strain energy stored in the buckled bar is given by,

$$\Delta U_f = \frac{EI_z}{2}\int_0^l \left(\frac{d^2u_y}{dx^2}\right)^2 dx \tag{4.12}$$

The second derivative of the bar's deflection equation is,

$$\frac{d^2u_y}{dx^2} = -a_1\frac{\pi^2}{l^2}sin\left(\frac{\pi x}{l}\right) - 2^2a_2\frac{\pi^2}{l^2}sin\left(\frac{2\pi x}{l}\right) - 3^2a_3\frac{\pi^2}{l^2}sin\left(\frac{3\pi x}{l}\right)\ldots \tag{4.13}$$

If the second derivative in Equation 4.13 is substituted into the strain energy equation (Equation 4.12) it will result in two types of terms inside the integral as,

$$a_n^2\frac{n^4\pi^4}{l^4}sin^2\left(\frac{n\pi x}{l}\right) \quad \text{and} \quad 2a_na_m\frac{n^2m^2\pi^4}{l^4}sin\left(\frac{n\pi x}{l}\right)sin\left(\frac{m\pi x}{l}\right) \tag{4.14}$$

by using direct integration it can be shown that,

$$\int_0^l \sin^2\left(\frac{n\pi x}{l}\right) dx = \frac{l}{2} \tag{4.15}$$

$$\int_0^l \sin\left(\frac{n\pi x}{l}\right)\sin\left(\frac{m\pi x}{l}\right) dx = 0 \tag{4.16}$$

Of the two terms, only the first type with squared coefficients will remain in the strain energy equation after simplification. Now the strain energy equation of the bar becomes,

$$\Delta U_f = \frac{\pi^4 EI}{4l^3}\left(a_1^2 + 2^4a_2^2 + 3^4a_3^2 + \ldots\right) \tag{4.17}$$

$$\implies \Delta U_f = \frac{\pi^4 EI}{4l^3}\sum_{n=1}^{\infty} n^4a_n^2 \tag{4.18}$$

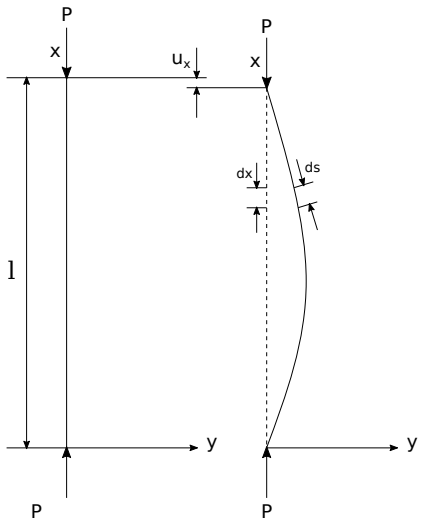

Figure 4.4: Vertical displacement of buckled bar

To calculate the strain energy stored in the elastic foundation we need to find the reaction force the foundation provides to every element dx of the bar. The modulus of the foundation defined in Equation 4.1 can be used for this. The reaction force due to each element dx is $\beta u_y dx$. Thus, the extensional strain energy stored in the foundation is,

$$\Delta U_m = \frac{\beta}{2} \int_0^l u_y^2 \, dx \tag{4.19}$$

Substituting the bar's deflection expression (Equation 4.2) into the strain energy of the foundation (Equation 4.19) and simplifying it using the same technique used in the case of the strain energy of the bar(Equation 4.16), we get,

$$\Delta U_m = \frac{\beta l}{4} \sum_{n=1}^{\infty} a_n^2 \tag{4.20}$$

To find the total work done by the compressing load P, we need to find an expression for the downward displacement (See Figure 4.4), say u_x, it causes in terms of the coordinates and displacement of the bar i.e. du_y and dx. If a single element on the bar is given by ds and dx denotes an element on the chord between the two ends then,

$$ds - dx = \sqrt{dx^2 + du_y^2} - dx \quad \text{(or)} \tag{4.21}$$

$$ds - dx = dx\sqrt{1 + \left(\frac{du_y}{dx}\right)^2} - dx \tag{4.22}$$

This expression for $ds - dx$ can be further simplified by applying the Taylor series of $\sqrt{1+a}$ as,

$$\sqrt{1+a} = 1 + \frac{1}{2}a - \frac{1}{8}a^2 + \dots \tag{4.23}$$

if the higher order terms are ignored and we expand the Taylor series in Equation 4.22 we get,

$$ds - dx \approx \frac{1}{2}\left(\frac{du_y}{dx}\right)^2 dx \tag{4.24}$$

u_x can be found by integrating Equation 4.24 over the length of the bar.

$$u_x = \frac{1}{2}\int_0^l \left(\frac{du_y}{dx}\right)^2 dx \tag{4.25}$$

By squaring the first derivative of the general equation of the bar and substituting it into Equation 4.25 we get two types of terms,

$$\cos^2\frac{n\pi x}{l} \quad \text{and} \quad \cos\frac{n\pi x}{l}\cos\frac{m\pi x}{l} \tag{4.26}$$

by direct integration, it can be shown that,

$$\int_0^l \cos^2\frac{n\pi x}{l}\,dx = \frac{l}{2} \tag{4.27}$$

$$\int_0^l \cos\frac{n\pi x}{l}\cos\frac{m\pi x}{l}\,dx = 0 \tag{4.28}$$

therefore the expression for u_x is,

$$u_x = \frac{\pi^2}{4l}\sum_{n=1}^{\infty} n^2 a_n^2 \tag{4.29}$$

Thus, the total work done by the compressing force P is,

$$\Delta T = \frac{P\pi^2}{4l}\sum_{n=1}^{\infty} n^2 a_n^2 \tag{4.30}$$

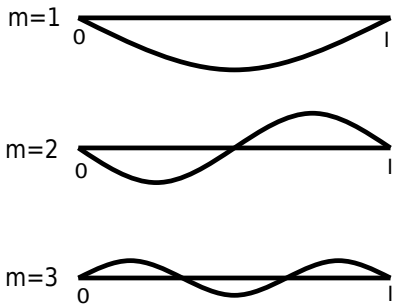

Figure 4.5: Effect of m on the buckling curve

The Energy Method works on the principle that the system is stable if $\Delta U > \Delta T$ and unstable if $\Delta U < \Delta T$. Thus, the critical condition can be evaluated by equating ΔT and ΔU.

$$\Delta T = \Delta U_f + \Delta U_m \tag{4.31}$$

The expression for the load P is found by substituting the expressions for $\Delta T, \Delta U_f$ and ΔU_e into Equation 4.31,

$$P = \frac{\pi^2 EI}{l} \frac{\sum_{n=1}^{\infty} n^2 a_n^2 + \frac{\beta l^4}{\pi^4 EI} \sum_{n=1}^{\infty} a_n^2}{\sum_{n=1}^{\infty} n^2 a_n^2} \tag{4.32}$$

To find the critical load P_{cr} we need find values for the coefficients $a_1, a_2, a_3, \ldots$ such that the expression of the load P becomes minimum. Setting all the coefficients to zero will result in an indeterminate expression. Thus, the critical load can be found by putting all but one coefficient to zero. This implies that the equation of the bar is a simple sine curve with a number of half sine curves. If we let a_m be the co-efficient that is not zero,

$$u_y = a_m \sin \frac{m\pi x}{l} \tag{4.33}$$

becomes the curve equation of the buckled bar. The critical load expression is,

$$P_{cr} = \frac{\pi^2 EI}{l^2} \left(m^2 + \frac{\beta l^4}{m^2 \pi^4 EI} \right) \tag{4.34}$$

Thus, by knowing the material properties of the elastic medium supporting the bar we can find out for which value of m the critical load P_{cr} is minimum. The value of m will tell

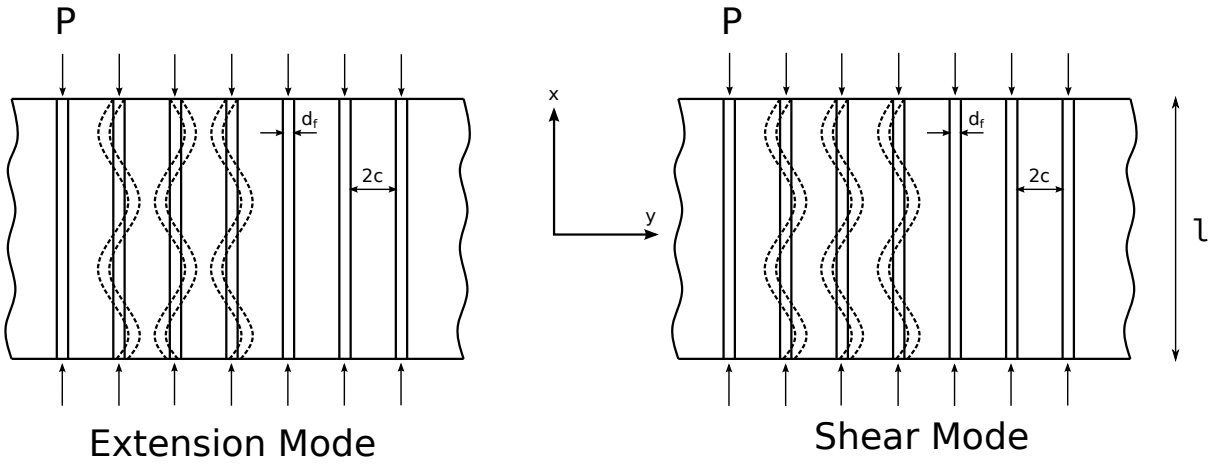

Figure 4.6: Analytical model used by Dow and Rosen[67]

us the number of half sine waves in the buckled bar(See Figure 4.5) and its wavelength (l/m).

4.3 Microbuckling of Fibers Under Compression - Dow and Rosen formulation

Dow and Rosen studied the micro-buckling of glass fibers in an epoxy matrix [67]. They observed the phenomenon of micro-buckling when glass fibers micro-buckled due to the compressing load applied by a shrinking of the epoxy matrix during curing. Fiber of diameters $127\mu m$, $88.9\mu m$ and $12.7\mu m$ all buckled but at different wavelengths and amplitudes. While the epoxy is the same for all three cases, cured at $250°F$. The analytical model of a column on an elastic foundation by Timoshenko indicates that the buckling wavelength of a circular column is proportional to its diameter. They found this to be true as their experimental data matched Timoshenko's analytical prediction, thus, providing justification to consider elastic instability mode as the failure mode for the bucking of the fibers. Two modes of failure are considered in their analysis the extension mode and shear mode as shown in Figure 4.6. The extension mode is when the adjacent fibers buckle out of phase and cause the matrix to extend in the direction perpendicular to the matrix. In the shear mode of failure the fibers buckle in-phase with each other and apply only shear stress on the matrix. The derivations of Dow-Rosen [67] critical stress and

strain for both these modes have been repeated here for reference.

They use the energy method in the analytical analysis to calculate the strain energy stored in the matrix(ΔU_m) and the fiber (ΔU_f), and compare it with the total work done by the compressing force(ΔT) to predict under what conditions the instability (buckling) will occur.

$$\Delta U_f + \Delta U_m = \Delta T \tag{4.35}$$

Each fiber is assumed to buckle in a sinusoidal pattern, then the displacement in the y direction can be represented as,

$$u_y = \sum_n a_n \sin \frac{n\pi x}{l} \tag{4.36}$$

The stress and strain in the y-direction on the matrix is given by,

$$\epsilon_y = \frac{u_y}{c} \tag{4.37}$$

$$\sigma_y = E_m \frac{u_y}{c} \tag{4.38}$$

Where, c is the half-distance between the fibers (See Figure 4.6).

Extension Mode

Let us consider the extension mode of failure first. In this mode, the strain energy stored in the matrix was calculated by substituting Equation 4.38 into Equation 4.39

$$\Delta U_{me} = \frac{1}{2} \int_V \sigma_y \epsilon_y \, dV \tag{4.39}$$

Noting that for unit thickness, $dV = 2c.dx$, this results in,

$$\Delta U_{me} = \frac{E_m}{c} \int_V \left(\sum_n a_n \sin \frac{n\pi x}{l} \right)^2 dx \tag{4.40}$$

To solve this integral they apply a similar technique used in Section 4.2. Thus, the strain energy in the matrix is,

$$\Delta U_{me} = \frac{E_m l}{2c} \sum_{n=1}^{\infty} a_n^2 \tag{4.41}$$

For the strain energy stored in the fiber the expression derived in Timoshenko's Elastic Stability[17] (Equation 4.18) was directly used by substituting for the fiber's moment of inertia $I_z = d_f^3/12$ (Assuming unit thickness).

$$\Delta U_f = \frac{\pi^4 E_f d_f^3}{48 l^3} \sum_{n=1}^{\infty} n^4 \, a_n^2 \tag{4.42}$$

The expression for the work done by the compressing force P was also taken directly from Timoshenko's Elastic Stability[17] (Equation 4.30) and is shown below again,

$$\Delta T = \frac{P\pi^2}{4l} \sum_{n=1}^{\infty} n^2 a_n^2 \tag{4.43}$$

To find an expression for the stress σ_f, the expression for the load P is found by substituting Equation 4.41,4.42 and 4.43 into Equation 4.35 and then divided by d_f. Since, $P = \sigma_f d_f$ (Assuming unit thickness).

$$\sigma_f = \frac{\pi^2 E_f d_f^2}{12 l^2} \frac{\sum_n n^4 \, a_n^2 + \left(\frac{24 l^4 E_m}{\pi^4 c d_f^3 E_f}\right) \sum_n a_n^2}{\sum_n n^2 \, a_n^2} \tag{4.44}$$

The critical stress was found by setting all but one of the coefficients in the series to zero such that the displacement equation becomes a simple sine curve just like in the case of Equation 4.34.

$$\sigma_{fcr} = \frac{\pi^2 E_f d_f^2}{12 l^2} \left(m^2 + \frac{24 l^4 E_m}{\pi^4 c d_f^3 E_f} \frac{1}{m^2} \right) \quad \text{where,} \quad m = 1, 2, 3, 4, \ldots, \infty \tag{4.45}$$

The value m represents the number of half sine waves in the buckled fiber of length l. This critical stress depends directly on the value of m. To obtain the minimum critical stress we can differentiate this expression w.r.t m^2 and put it to zero according to the property of a minima. This can be done because m may be considered continuous as it

runs up to infinity.

$$\frac{\partial \sigma_{fcr}}{\partial m^2} = \frac{\pi^2 E_f d_f^2}{12 l^2}\left[1 - \frac{24 l^4 E_m}{\pi^4 c d_f^3 E_f}\frac{1}{m^4}\right] = 0 \tag{4.46}$$

$$\implies m^2 = \frac{l^2}{\pi^2}\left(\frac{24 E_m}{c d_f^3 E_f}\right)^{\frac{1}{2}} \tag{4.47}$$

putting the expression of m^2 (Equation 4.47) back into Equation 4.45 and simplifying,

$$\sigma_{fcr} = 2\left[\frac{V_f E_m E_f}{3(1-V_f)}\right]^{\frac{1}{2}} \tag{4.48}$$

$$\text{where,} \quad V_f = \frac{d_f}{d_f + 2c} \tag{4.49}$$

The critical strain in the fiber can be calculated as,

$$\epsilon_{fcr} = \sigma_{fcr}\frac{1}{E_f} \tag{4.50}$$

$$\implies \epsilon_{fcr} = 2\left[\frac{V_f}{3(1-V_f)}\right]^{\frac{1}{2}}\left(\frac{E_m}{E_f}\right)^{\frac{1}{2}} \tag{4.51}$$

The critical composite stress (σ_c) in the longitudinal (x - axis) direction is,

$$\sigma_c = V_f \sigma_{fcr} \tag{4.52}$$

$$\implies \sigma_c = 2V_f\left[\frac{V_f E_m E_f}{3(1-V_f)}\right]^{\frac{1}{2}} \tag{4.53}$$

Shear Mode

In the shear mode of failure the fibers buckle in-phase and the matrix only experiences a shear strain. This shear shear strain is given by,

$$\gamma_{xy} = \frac{\partial u_y}{\partial x} + \frac{\partial u_x}{\partial y} \tag{4.54}$$

Dow and Rosen[67] assume that the shear strain in the matrix is independent of the y coordinate and is a function of only the longitudinal x coordinate. This means that the

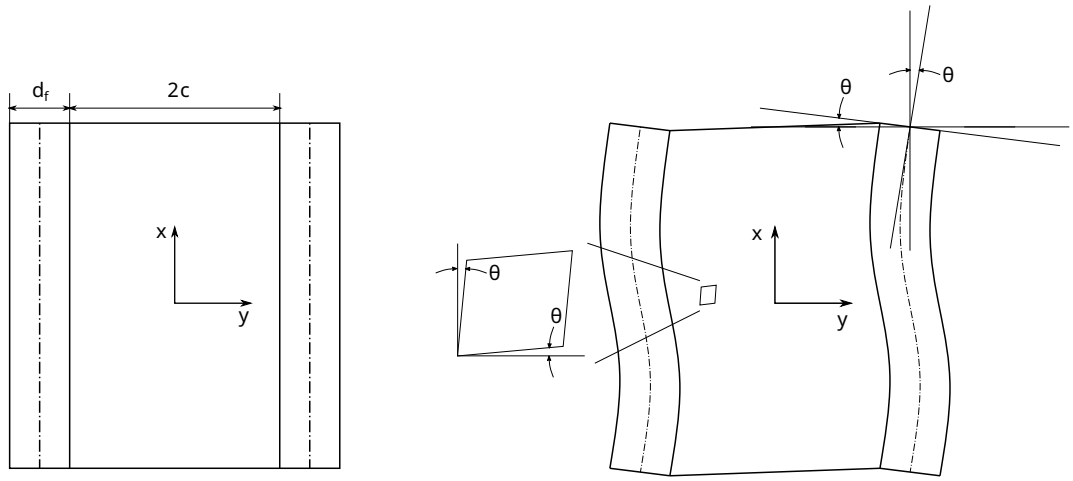

Figure 4.7: Shear mode deformation of fiber and matrix

transverse displacement of the matrix is the same as the transverse displacement (u_y)of the fiber (See Figure 4.7),

$$\left.\frac{\partial u_y}{\partial x}\right|_m = \left.\frac{du_y}{dx}\right|_f \tag{4.55}$$

Since the shear strain does not vary with the y coordinate,

$$\frac{du_x}{dy} = \frac{u_x(c) - u_x(-c)}{2c} \tag{4.56}$$

Dow and Rosen[67] consider the shear deformation of the fiber to be negligible. At c, from Figure 4.7, we have,

$$\tan\theta = \frac{u_x(c)}{d_f/2} \tag{4.57}$$

But, $\theta = du_y/dx$. Since θ is the angle formed by the tangent of the buckled fiber with the x-axis (See Figure 4.7). Thus, the longitudinal displacement ($u_x(c)$) is given by,

$$u_x(c) = \left.\frac{d_f}{2}\frac{du_y}{dx}\right|_f \tag{4.58}$$

Putting Equation 4.58 back into Equation 4.56 and simplifying it, we have,

$$\frac{du_x}{dy} = \left.\frac{d_f}{2c}\frac{du_y}{dx}\right|_f \tag{4.59}$$

Substituting the Equation 4.55 and 4.59 back into the shear strain equation (Equation 4.54) we get,

$$\gamma_{xy} = \left(1 + \frac{d_f}{2c}\right) \left.\frac{du_y}{dx}\right|_f \tag{4.60}$$

Thus, the strain energy stored in the matrix due to shear strain it experiences is given by,

$$\Delta U_{ms} = \frac{1}{2} \int_V \tau_{xy}\gamma_{xy}\, dV = \frac{G_m}{2} \int_V \gamma_{xy}^2\, dV \tag{4.61}$$

Where, G is the shear modulus of the matrix, and V is the volume of the unit cell. Noting that $dV = 2c.dx$ (unit thickness) and substituting for the shear strain (Equation 4.60) we have,

$$\Delta U_{ms} = G_m \left(1 + \frac{d_f}{2c}\right)^2 \int_0^l \left(\frac{du_y}{dx}\right)^2 dx \tag{4.62}$$

This equation is similar to Equation 4.25. Thus, the integral may be simplified using the same technique. Then, the expression for the strain energy stored in the matrix will be,

$$\Delta U_{ms} = G_m c \left(1 + \frac{d_f}{2c}\right)^2 \left(\frac{\pi^2}{2l}\right) \sum_{n=1}^{\infty} a_n^2\, n^2 \tag{4.63}$$

The strain energy stored in the fiber and the work done by the compressing force P remain unchanged in the shear mode too. Thus, by substituting Equation 4.63, 4.42 and 4.43 back into the Equation 4.35 we can find an expression for the load P. Noting that $\sigma_f = P/d_f$ (unit thickness), the expression for the normal fiber stress σ_f is,

$$\sigma_f = \frac{\frac{2G_m c}{d_f}\left(1 + \frac{d_f}{2c}\right)^2 \sum_n n^2\, a_n^2 + \frac{\pi^2 E_f d_f^2}{12l^2} \sum_n n^4\, a_n^2}{\sum_n n^2\, a_n^2} \tag{4.64}$$

To find the critical fiber stress this expression can be minimized by putting all the co-efficients a_n to zero except for one. If a_m was this non-zero co-efficient and noting that $V_f = d_f/2c$, the critical fiber stress is given by,

$$\sigma_{fcr} = \frac{G_m}{V_f(1 - V_f)} + \frac{\pi^2 E_f}{12} \left(\frac{m d_f}{l}\right)^2 \tag{4.65}$$

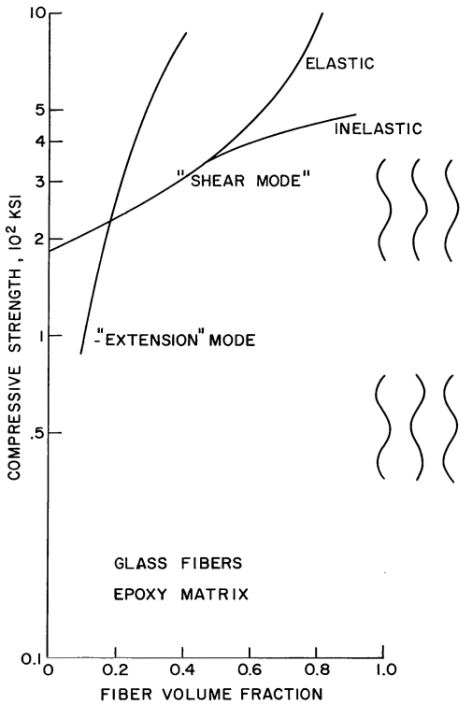

Figure 4.8: Comparing the critical stress of Extension and Shear modes[67]

As L/m is the buckling wavelength, the second term in Equation 4.65 was eliminated since it is small for large wavelengths compared to the fiber diameter d_f. Thus, the critical buckling stress is approximately given by,

$$\sigma_{fcr} = \frac{G_m}{V_f(1 - V_f)} \tag{4.66}$$

The critical strain of the fiber is given by,

$$\epsilon_{fcr} = \frac{G_m}{V_f(1 - V_f)E_f} \tag{4.67}$$

Then, the composite critical stress is given by,

$$\sigma_c = V_f\sigma_{fcr} = \frac{G_m}{(1 - V_f)} \tag{4.68}$$

Dow and Rosen[67] plotted the composite critical stress for the extension mode(Equation 4.53) and shear mode(Equation 4.68) for different fiber volume fractions, shown in Figure 4.8. They concluded that for Epoxy-Glass Fiber composites it for fiber volume fractions

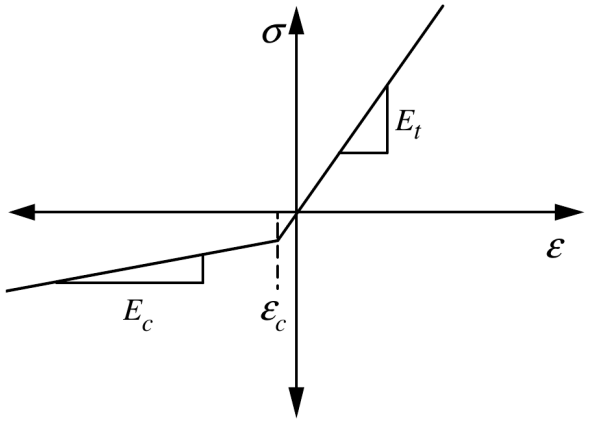

Figure 4.9: Assumed stress-strain response of the EMC material[68]

higher that 0.6 the shear mode of failure has a lower critical stress and is much more likely to occur.

4.4 Bending Mechanics of Elastic Memory Composites - Campbell formulation

Elastic Memory Composites (EMC) uses a completely cured thermoset resin that has an 'elastic memory'. For packaging, the composite is heated to a temperature near or above the glass transition temperature (T_g) of the resin and deformed into the packed shape. It is then cooled while holding the structure in the constrained shape after which the constraint is removed and the composite continues to hold its shape. To revert back to the shape the composite had when it was cured, it is heated to a temperature above the T_g of the resin. Fiber Microbuckling is the mechanism that allows the composite to withstand very high packaging strains without breaking. Campbell et. al [68] analytically described this microbuckling phenomenon and derived expressions for the location of the neutral surface after buckling, and the critical wavelength (λ_{cr}), stress (σ_{cr}) and strain (ϵ_{cr}). These derivations have been repeated in this section for reference.

Campbell et. al [68] assumes a constitutive model, shown in Figure 4.9, in which the tensile modulus (E_t) is given by the classical laminate theory while the compression modulus is reduced drastically beyond the critical strain (ϵ_{cr}) due to the microbuckling

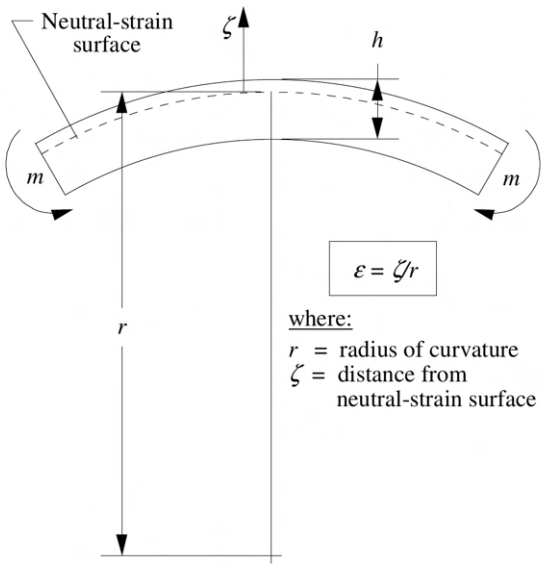

Figure 4.10: Bending of the Elastic Memory Composite

of the fibers. The kinematic assumptions of Euler-beam theory and Kirchoff-Love plate theory is used by Campbell et. al. In particular, they assume that the cross-sections remain flat and perpendicular to the neutral strain surface even under bending strains.

Figure 4.10 shows the front view of the EMC laminate under bending. Due to microbuckling of the fibers under compression the laminate loses stiffness and the neutral surface moves closer to the fibers under tension. Let, ζ be a longitudinal or vertical coordinate that has its origin on the neutral surface (See Figure 4.10). Then, the extensional strain (ϵ) induced through the cross-section is given by,

$$\epsilon = \frac{\zeta}{r} \tag{4.69}$$

where, r is the radius of curvature of the neutral surface. The stress through the cross-section is,

$$\sigma(\zeta) = E_t \frac{\zeta}{r} \quad , \quad \zeta > -\epsilon_{cr} r \tag{4.70}$$

$$\sigma(\zeta) = E_c \left(\frac{\zeta}{r} + \epsilon_{cr} \right) - E_t \epsilon_{cr} \quad , \quad \zeta < -\epsilon_{cr} r \tag{4.71}$$

Figure 4.11 shows the cross-section of the laminate in which the regions of microbuck-

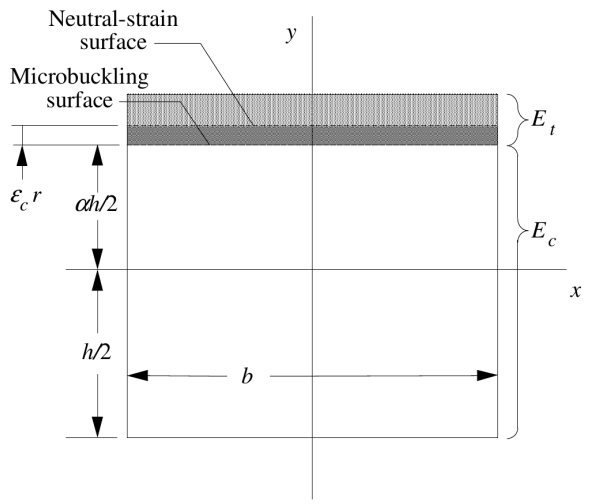

Figure 4.11: Cross section of the EMC laminate

ling and non-microbuckling (shaded) fibers are shown. The non-microbuckling region contains the fibers under tension and the small portion of fibers that experience a strain lesser than the critical strain (ϵ_{cr}). The location of the of neutral surface is shown in the terms of the x-y coordinate system whose origin lies at the centroid of the cross-section. To express the stresses in the x-y coordinate system we need the relationship between ζ and y.

$$\zeta = y - \frac{\alpha h}{2} - r\epsilon_{cr} \tag{4.72}$$

Thus, using the relation in Equation 4.72 we can rewrite the stress equations in terms of the y coordinate,

$$\sigma(y) = E_t\left(\frac{y}{r} - \frac{\alpha h}{2r} - \epsilon_{cr}\right) \qquad , \frac{\alpha h}{2} \leq y \leq \frac{h}{2} \tag{4.73}$$

$$\sigma(y) = E_c\left(\frac{y}{r} - \frac{\alpha h}{2r}\right) - E_t\epsilon_{cr} \qquad , \frac{-h}{2} \leq y \leq \frac{\alpha h}{2} \tag{4.74}$$

To find an expression for α which gives the location of the neutral surface we sum the forces normal to the cross-section,

$$b\int_{\alpha h/2}^{h/2}\sigma(y)dy + b\int_{-h/2}^{\alpha h/2}\sigma(y)dy = 0 \tag{4.75}$$

$$\left[E_t\left(\frac{y^2}{2r} - \frac{\alpha h y}{2r} - \epsilon_{cr} r\right)\right]_{\alpha h/2}^{h/2} + \left[E_c\left(\frac{y^2}{2r} - \frac{\alpha h y}{2r}\right) - E_c\epsilon_{cr} y\right]_{-h/2}^{\alpha h/2} = 0 \tag{4.76}$$

$$\implies \left[E_t\left(\frac{h^2(\alpha^2-1)}{8r} - \frac{\alpha h^2(1-\alpha)}{4r} - \frac{\epsilon_{cr}h(1-\alpha)}{2}\right)\right] + \tag{4.77}$$

$$\left[E_c\left(\frac{h^2(\alpha^2)-1}{8r} - \frac{\alpha h^2(\alpha+1)}{4r}\right) - E_t\epsilon_{cr}\frac{h(\alpha+1)}{2}\right] = 0 \tag{4.78}$$

$$\implies E_t\frac{h^2}{8r}(1-\alpha^2) - \frac{E_t\alpha h^2}{4r}(1-\alpha) - \frac{E_t\epsilon_{cr}h}{2}(1-\alpha) + \tag{4.79}$$

$$E_c\frac{h^2}{8r}(\alpha^2-1) - \frac{E_c\alpha h^2}{4r}(\alpha+1) - \frac{E_t\epsilon_{cr}h}{2}(\alpha+1) = 0 \tag{4.80}$$

$$\implies (1-\alpha^2)\frac{h^2}{8r}(E_t - E_c) - \frac{\alpha h^2}{4r}(E_t - \alpha E_t + \alpha E_c + E_c) - E_t\epsilon_{cr}h = 0 \tag{4.81}$$

$$\implies (1-\alpha^2)\frac{h}{8r}(E_t - E_c) - \frac{\alpha h}{4r}(E_t(1-\alpha) + E_c(1+\alpha)) - E_t\epsilon_{cr} = 0 \tag{4.82}$$

$$\implies (1-\alpha^2)\left(1 - \frac{E_c}{E_t}\right) - 2\alpha\left((1-\alpha) + \frac{E_c}{E_t}(1+\alpha)\right) - \frac{8r\epsilon_{cr}}{h} = 0 \tag{4.83}$$

$$\implies 1 - \frac{E_c}{E_t} - \alpha^2 + \frac{E_c}{E_t}\alpha^2 - 2\alpha + 2\alpha^2 - 2\frac{E_c}{E_t}\alpha - 2\frac{E_c}{E_t}\alpha^2 - \frac{8r\epsilon_{cr}}{h} = 0 \tag{4.84}$$

$$\implies (1-\alpha)^2 - \frac{E_c}{E_t}(1+\alpha)^2 - \frac{8r\epsilon_{cr}}{h} = 0 \tag{4.85}$$

$$\left(1 - \frac{E_c}{E_t}\right)\alpha^2 - 2\left(1 + \frac{E_c}{E_t}\right)\alpha + \left(1 - \frac{E_c}{E_t} - \frac{8r\epsilon_{cr}}{h}\right) = 0 \tag{4.86}$$

Let, $E_c/E_t = \gamma$. Thus, α is given by,

$$\alpha = \frac{2(1+\gamma) \pm \sqrt{(-2(1+\gamma))^2 - 4(1-\gamma)\left(1 - \gamma - \frac{8r\epsilon_{cr}}{h}\right)}}{2(1-\gamma)} \tag{4.87}$$

$$\implies \alpha = \frac{2(1+\gamma) \pm \sqrt{4 + 8r + 4r^2 - 4\left(1 - \gamma - \frac{8r\epsilon_{cr}}{h} - \gamma + \gamma^2 + \frac{8r\epsilon_{cr}\gamma}{h}\right)}}{2(1-\gamma)} \tag{4.88}$$

$$\implies \alpha = \frac{2(1+\gamma) \pm \sqrt{16\gamma - \frac{32r\epsilon_{cr}\gamma}{h} + \frac{32r\epsilon_{cr}}{h}}}{2(1-\gamma)} \tag{4.89}$$

$$\implies \alpha = \frac{2(1+\gamma) \pm \sqrt{16\left(\gamma + \frac{2r\epsilon_{cr}}{h}(1-\gamma)\right)}}{2(1-\gamma)} \tag{4.90}$$

$$\text{Let,} \quad \frac{h}{2r\epsilon_{cr}} = \kappa \tag{4.91}$$

$$\alpha = \frac{2(1+\gamma) \pm \sqrt{16\left(\gamma + \frac{1}{\kappa}(1-\gamma)\right)}}{2(1-\gamma)} \tag{4.92}$$

$$\implies \alpha = \frac{(1+\gamma) - 2\sqrt{\gamma + \frac{1}{\kappa}(1-\gamma)}}{1-\gamma} \quad \text{, for } \alpha < 1 \tag{4.93}$$

Equation 4.93 is valid only for $\kappa > 1$. If $\kappa < 1$ then $E_c = E_t$ which will make the expression indeterminate. Thus, if $\kappa < 1$ there will be no microbuckling.

$$\alpha = -1 \qquad , \kappa < 1 \tag{4.94}$$

$$\alpha = \frac{1}{1 - E_c/E_t}\left(1 + \frac{E_c}{E_t} - 2\sqrt{\frac{E_c}{E_t} + \frac{1}{\kappa}(1 - \frac{E_c}{E_t})}\right) \qquad , \kappa > 1 \tag{4.95}$$

To derive expressions for the critical wavelength and strain Campbell et. al considers a model of single fiber embedded in a finite matrix and subjected to a compressing load, shown in Figure 4.12a. They also assume that the fibers deform in the shear mode (in-phase) which means that the matrix will undergo only shear deformation due to the buckling of the fibers. Campbell et. al obtained an expression for the critical wavelength λ_c by comparing the extensional strain energy used by Timoshenko (See Section 4.2) and matrix shear energy they derived.

Figure 4.12b illustrates the shear deformation in the matrix surrounding the fiber. If the deformation angle γ is small, the matrix shear strain energy is given by,

$$d\Delta U_m = \frac{1}{2}(\tau dA)(\gamma dx) \tag{4.96}$$

Integrating the strain energy for the length of the fiber,

$$\Delta U_{ms} = \int_0^l \frac{1}{2}(\tau dA)(\gamma dx) \tag{4.97}$$

$$\text{Substituting,} \quad \tau = G_m\gamma \quad dA = \delta^2 V_m \tag{4.98}$$

$$\Delta U_{ms} = \frac{1}{2} G_m \delta^2 V_m \int_0^l \gamma^2 dx \tag{4.99}$$

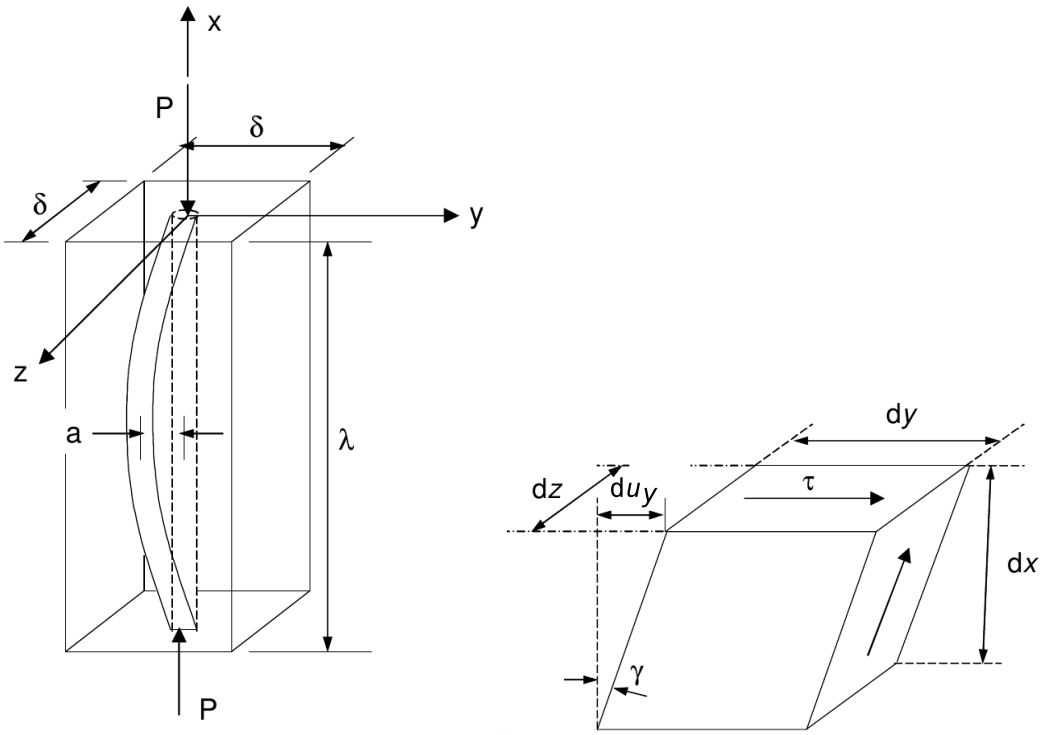

(a) Fiber Embeded in Finite Matrix[68] (b) Matrix Shearing Element[68]

Figure 4.12: Microbuckling model used by Campbell et. al[68]

Campbell *et al.*, assumes shear deformation γ to be,

$$\gamma = \frac{du_y}{dx} \tag{4.100}$$

The buckled shape of the fiber was assumed to be,

$$u_y = a \sin\left(\frac{m\pi x}{l}\right) \tag{4.101}$$

Substituting Equation 4.100 and 4.101 back in to the matrix shear strain energy (Equation 4.99),

$$\Delta U_{ms} = \frac{G_m \delta^2 V_m}{2} \int_0^l \left(\frac{am\pi}{l}\right)^2 \left(\cos\frac{m\pi x}{l}\right)^2 dx \tag{4.102}$$

$$\implies \Delta U_{ms} = \frac{G_m V_m}{2} \left(\frac{am\pi\delta}{l}\right)^2 \int_0^l \cos^2\frac{m\pi x}{l} dx \tag{4.103}$$

$$\implies \Delta U_{ms} = \frac{G_m V_m}{2} \left(\frac{am\pi\delta}{l}\right)^2 \frac{l}{2} \tag{4.104}$$

$$\implies \Delta U_{ms} = \frac{G_m V_m}{4l}(am\pi\delta)^2 \tag{4.105}$$

The extensional matrix strain energy derived by Timoshenko[17](See Section 4.2) is given by,

$$\Delta U_e = \frac{\beta a^2 l}{4} \tag{4.106}$$

By, equating the two matrix strain energies Campbell et. al derived an expression for the foundation stiffness term β.

$$\frac{G_m V_m}{4l}(am\pi\delta)^2 = \frac{\beta a^2 l}{4} \tag{4.107}$$

$$\implies \beta = \frac{G_m V_m (n\pi\delta)^2}{l^2} \tag{4.108}$$

An expression for the foundation modulus can also be derived by minimizing the critical load derived by Timoshenko[17](See Section 4.2),

$$P_{cr} = \frac{\pi^2 E_f I_f}{l^2}\left(m^2 + \frac{\beta l^4}{m^2\pi^4 E_f I_f}\right) \tag{4.109}$$

$$\text{Minimizing,} \quad \frac{dP_{cr}}{dm^2} = 0 \tag{4.110}$$

$$\implies \frac{\pi^2 E_f I_f}{l^2}\left(1 - \frac{\beta l^4}{m^4\pi^4 E_f I_f}\right) = 0 \tag{4.111}$$

$$\implies \beta = \frac{m^4\pi^4 E_f I_f}{l^4} \tag{4.112}$$

To find an expression for the critical wavelength (λ_{cr}) the two expressions for the foundation modulus β are compared,

$$\frac{G_m V_m (m\pi\delta)^2}{l^2} = \frac{m^4\pi^4 E_f I_f}{l^4} \tag{4.113}$$

$$\lambda_c^2 = \left(\frac{l}{m}\right)^2 = \frac{\pi^2 E_f I_f}{G_m V_m \delta^2} \tag{4.114}$$

To express the critical wavelength λ_c only in terms of the material properties, the values for I_f and δ are substituted. To get an expression for δ in terms of the fiber radius it is

assumed that the fibers are square packed in the matrix.

$$I_f = \frac{\pi}{64} d_f^4 \tag{4.115}$$

$$\delta^2 = \frac{\pi}{4} d_f^2 \frac{1}{V_f} \tag{4.116}$$

Substituting Equation 4.116 back into the expression for λ_c (Equation 4.114),

$$\lambda_c = \frac{\pi d_f}{4} \sqrt{\frac{E_f V_f}{G_m V_m}} \tag{4.117}$$

To find the critical strain Campbell et. al used the simplified form of Timoshenko's critical load. This simplified form is obtained by substituting for $(l/m)^2$ from the foundation modulus expression (Equation 4.112) in Timoshenko's critical load expression (Equation 4.34)

$$P_{cr} = \frac{\pi^2 E_f I_f}{l^2} \left(m^2 + \frac{\beta l^4}{m^2 \pi^4 E_f I_f} \right) \tag{4.118}$$

$$\beta = \frac{m^4 \pi^4 E_f I_f}{l^4} \tag{4.119}$$

$$\implies \left(\frac{l}{n} \right)^2 = \pi^2 \sqrt{\frac{E_f I_f}{\beta}} \tag{4.120}$$

Thus, the simplified critical load expression is,

$$P_{cr} = 2\sqrt{\beta E_f I_f} \tag{4.121}$$

To express β in terms of only the composite material properties we substitute the value of $\lambda_c r$ (Equation 4.117) in the expression for the foundation modulus (Equation 4.112).

$$\beta = \frac{256 I_f G_m^2 V_m^2}{d^4 E_f V_f^2} \tag{4.122}$$

$$I_f = \frac{\pi}{64} d_f^4 \tag{4.123}$$

$$\implies \beta = \frac{4\pi G_m^2 V_m^2}{E_f V_f^2} \tag{4.124}$$

Substituting Equation 4.124 back into the reduced critical load expression (Equation 4.121),

$$P_{cr} = \frac{\pi G_m V_m d_f^2}{2V_f} \tag{4.125}$$

Thus, the critical stress expression is,

$$\sigma_{cr} = \frac{2G_m V_m}{V_f} \tag{4.126}$$

And the critical strain expression is,

$$\epsilon_{cr} = \frac{2G_m V_m}{E_f V_f} \tag{4.127}$$

4.5 Microbuckling of Composite laminates under bending - Z.D. Wang formulation

Z.D Wang *et al.*, derived another solution for the in-plane microbuckling of fibers when bending EMC laminates [69]. They use the following assumptions,

1. Fibers buckle sinusoidally with the same mode number.

2. Only in-plane microbuckling considered as no out-of-plane buckling was observed.

3. Only shear mode of buckling considered.

The derivation of Wang *et al.*, [69] for the critical stress, strain, and wavelength expressions have been repeated in this section for reference.

The shear strain energy is given by,

$$\Delta U_{ms} = \frac{1}{2}\int_V \tau_{xy}\gamma_{xy}\, dV = \frac{G_m}{2}\int_V \gamma_{xy}^2\, dV \tag{4.128}$$

Z.D Wang et. al considers the same model used by Dow et. al[67] for the shear mode of

microbuckling(See Section 4.3). Thus, the shear strain is given by,

$$\gamma_{xy} = \left(1 + \frac{d_f}{2c}\right) \frac{du_y}{dx} \tag{4.129}$$

Based on the assumptions made, the shape of the microbuckled fiber is expressed as,

$$u_y = a \sin\left(\frac{m\pi x}{l}\right) \tag{4.130}$$

Thus, substituting Equation 4.130 and Equation 4.129 back in the matrix shear strain energy (Equation 4.128) we get an expression similar to what Dow et. al [67] derived(Equation 4.63) but with only one mode number,

$$\Delta U_{ms} = G_m c \left(1 + \frac{d_f}{2c}\right)^2 \left(\frac{\pi^2}{2l}\right) a^2 m^2 \tag{4.131}$$

Z.D Wang derived an expression for the critical wavelength (λ_c) by comparing the elastic foundation energy derived by Timoshenko (Section 4.2) with the shear strain energy. By comparing these two strain energies we get an expression for the foundation modulus β.

$$\frac{\beta l a^2}{4} = G_m c \left(1 + \frac{d_f}{2c}\right)^2 \left(\frac{\pi^2}{2l}\right) a^2 m^2 \tag{4.132}$$

$$\beta = \frac{2 c d_f G_m \pi^2}{l^2} \left(1 + \frac{d_f}{2c}\right)^2 m^2 \tag{4.133}$$

An expression for the foundation modulus can also be derived by minimizing Timoshenko's critical load expression (Equation 4.112).

$$\beta = \frac{m^4 \pi^4 E_f I_f}{l^4} \tag{4.134}$$

By comparing Equation 4.133 and Equation 4.134 we can get the expression for the critical wavelength (λ_c),

$$\frac{m^4 \pi^4 E_f I_f}{l^4} = \frac{2 c d_f G_m \pi^2}{l^2} \left(1 + \frac{d_f}{2c}\right)^2 m^2 \tag{4.135}$$

$$\frac{l^2}{m^2} = \frac{\pi^2 E_f I_f}{2cd_f \left(1 + \frac{d_f}{2c}\right)^2 G_m} \tag{4.136}$$

$$\text{Recognizing, } \left(1 + \frac{d_f}{2c}\right) = \frac{1}{V_m} \tag{4.137}$$

$$\lambda_c^2 = \left(\frac{l}{m}\right)^2 = \frac{\pi^2 V_m^2 E_f I_f}{2cd_f G_m} \tag{4.138}$$

$$\text{Substituting, } \quad I_f = \frac{bd_f^3}{12} = \frac{d_f^4}{12} \tag{4.139}$$

$$\lambda_c^2 = \left(\frac{l}{m}\right)^2 = \frac{\pi^2 V_m^2 E_f d_f^3}{24cG_m} \tag{4.140}$$

To get an expression for the critical load (P_{cr}) Equation 4.140 and Equation 4.134 are substituted in Timoshenko's expression for critical load Equation 4.34,

$$P_{cr} = \frac{\pi^2 E_f I_f}{l^2}\left(m^2 + \frac{\beta l^4}{m^2 \pi^4 E_f I_f}\right) \tag{4.141}$$

$$\implies P_{cr} = \pi^2 E_f I_f \left(\frac{1}{\lambda_c^2} + \frac{\beta \lambda_c^2}{\pi^4 E_f I_f}\right) \tag{4.142}$$

$$\text{Substituting for } \beta, \tag{4.143}$$

$$\implies P_{cr} = \pi^2 E_f I_f \left(\frac{2}{\lambda_c^2}\right) \tag{4.144}$$

$$\text{Substituting for } \lambda_c, \tag{4.145}$$

$$\implies P_{cr} = \frac{4d_f c G_m}{V_m^2} \tag{4.146}$$

Thus, the critical stress is given by,

$$\sigma_{cr} = \frac{P_{cr}}{d_f(d_f + 2c)} = \frac{4cG_m}{(d_f + 2c)V_m^2} \tag{4.147}$$

$$\implies \sigma_{cr} = \frac{2G_m}{V_m} \tag{4.148}$$

And the critical strain is,

$$\epsilon_{cr} = \frac{2G_m}{V_m E_f} \tag{4.149}$$

Table 4.1: Wavelength measurement results

Steering Radius (mm)	Mean Wavelength (mm)	SD(±)
800	3.313	0.302
600	4.826	0.524
400	4.726	0.309
200	5.224	0.113

4.6 Assumptions and Limitations

Before discussing the results obtained by applying the Campbell and Wang models, it is important to recognize the assumptions and limitations of using these models directly. The steering of a thermoplastic tape by the AFP head is assumed to a problem of pure bending, i.e., any shear force applied by the AFP head is ignored. Since it is the compressive forces that drive the phenomenon of fiber buckling, the fibers under compression are looked at in isolation when trying to solve for the critical buckling stress and strain. In other words, the effect of the fibers and matrix in the tensile region is not considered. These assumptions help simplify the problem and the results of such a model can be used as a first approximation or rule-of-thumb.

4.7 Results and Discussion

4.7.1 Wavelength measurements for experimental samples

The buckling wavelengths of various steered samples were measured to understand how the wavelength varies with the steering radius. These measurements were performed on samples $4 - 15$ listed in Table 3.1. Peak-to-peak measurements were made using a 'Mitutoyo' digital Vernier caliper to determine the wavelength for each sample (See Figure 4.13). Ten such measurements were made for each steering radius from $800mm$ to $200mm$. No fiber buckling was observed in the tapes with a steering radius of $1000mm$, hence, they have not been included in this evaluation. Table 4.1 shows the results of these measurements with the mean wavelength and its standard deviation for each steering radius.

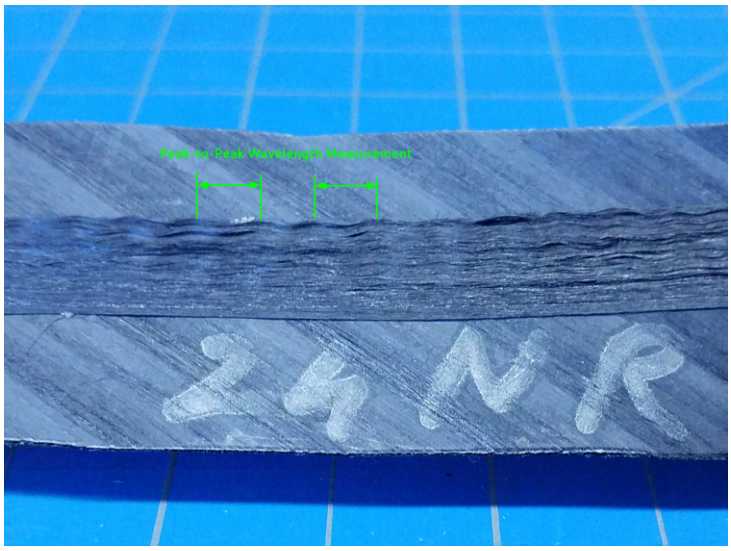

Figure 4.13: Wavelength measurement illustration

If the wavelength expressions in the analytical models (Equations 4.117, 4.140) were considered, the wavelengths would not be a function of the steering radius. However, this is not what is observed from the experimental measurements shown in Table 4.1. This is not a contradiction between the experimental results and the analytical models. It should be noted that the onset of buckling is described by the analytical models and not the post-buckling behaviour of the fibers. Buckling is first observed at the steering radius of $800mm$. This implies that the critical steering radius lies between $1000mm$ and $800mm$ with a critical wavelength that is lesser than $3.313mm$.

4.7.2 Analytical model results

A program was written using C/C++ to calculate the critical buckling wavelength and steering radius. The formulations derived by Campbell *et al.*, [68] and Wang *et al.*, [69] were adopted for this calculation as their problem definitions are very similar to steering of CF/PEEK tapes. They considered a plane stress approach for the bending of an elastic memory composite and the in-plane fiber buckling caused by it. The steering a of CF/PEEK tape using a HGT-assisted AFP is essentially the bending of a plane (the tape) by external moments which causes the fibers along the inner-edge of the tape to buckle under compression. The models of Campbell *et al.*, [68] and Wang *et al.*, [69] encompass the classical approaches of both Timoshenko and Dow-Rosen. The main

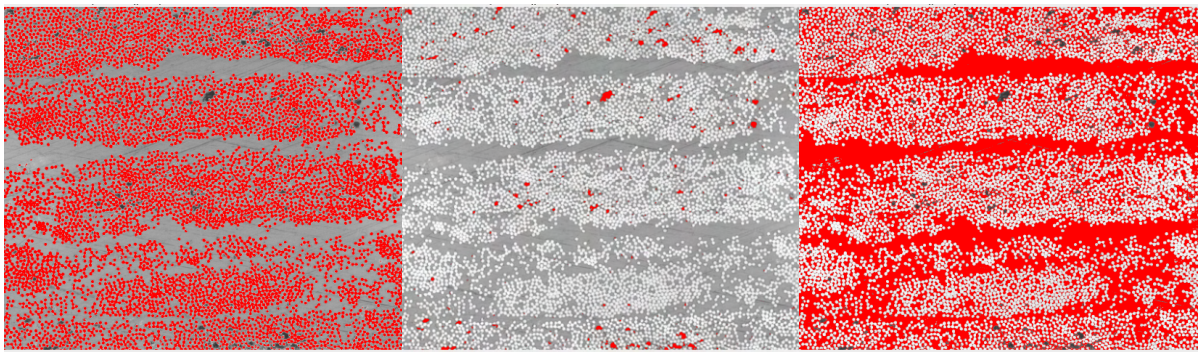

(a) Fiber area (b) Void area (c) Matrix area

Figure 4.14: Fiber volume fraction measurement

difference between the models of Campbell *et al.*, [68] and Wang *et al.*, [69] lies in how they treat the shear forces that act on the matrix due to the buckling of the fibers. Wang *et al.*, [69] considers the effect of the neighbouring fibers on the matrix while Campbell *et al.*, [68] does not (See Sections 4.4 and 4.5).

The values for the variables were either measured from experimental samples or taken from the data sheet provided by the vendor. The exception to this is the matrix shear modulus G_m. The nature of in-situ consolidation where the temperature falls sharply beyond the nip point makes it difficult to predict at what temperature fiber buckling takes place. The values for G_m were taken from a book on Thermoplastic aromatic composites by Cogswell[71]. To make a close approximation the G_{23} was taken as the shear modulus of the matrix. This is because the influence of fibers in this direction is negligible making G_{23} a matrix dominant property.

The fiber volume fraction (V_f) and fiber diameter (d_f) were measured using the microscopy images of the steered tape and substrate. The fiber diameter (d_f) was calculated by measuring the perimeter of the individual fibers. To measure the fiber volume fraction the thresholding technique in ImageJ software was used. The global scale for the measurement was first set and the area measurement was limited to only the highlighted threshold range. The image threshold was then adjusted to first highlight only the fibers, and then area of all the fibers (A_f) were measured. Then the area of voids (A_v), if any, were measured by again adjusting the threshold to highlight only the voids. The area of the matrix (A_m) was measured by highlighting the rest of area excluding the fibers and

Table 4.2: Parameters used to predict critical steering radius

Variables	**Symbol**	**Values**		
Temperature (C)	T	240	290	300
Matrix shear modulus (Pa)	G_m	$7.61E{+}08$	$4.25E{+}08$	$1.86E{+}08$
Fiber volume fraction	V_f	0.63		
Matrix volume fraction	V_m	0.37		
Fiber elastic modulus (Pa)	E_f	$2.27E{+}11$		
Fiber diameter (m)	d_f	$6.74E{-}06$		
Width of steered tape (m)	h	0.008		
Half length of matrix (m)	c	$1.98E{-}06$		

voids. This procedure has been shown in Figure 4.14. The fiber volume fraction was then calculated as,

$$V_f = \frac{A_f}{A_m + A_v} \tag{4.150}$$

The parameters used for the calculation of critical strain have been summarised in Table 4.2.

From Campbell's model the equations used to calculate the critical strain, steering radius and wavelength are,

$$\epsilon_c = \frac{2G_m V_m}{E_f V_f} \tag{4.151}$$

$$\lambda_c = \frac{\pi d_f}{4}\sqrt{\frac{E_f V_f}{G_m V_m}} \tag{4.152}$$

$$r_c = \frac{h}{2\epsilon_c} \tag{4.153}$$

For Wang's model the equations for ϵ_c and λ_c differ due their treatment of the shear strain. The equation for calculating the critical steering radius comes from beam theory, hence, it remains the same. The equations adopted from Wang's model are,

$$\epsilon_c = \frac{2G_m}{V_m E_f} \tag{4.154}$$

$$\lambda_c^2 = \left(\frac{l}{m}\right)^2 = \frac{\pi^2 V_m^2 E_f d_f^3}{24 c G_m} \tag{4.155}$$

$$r_c = \frac{h}{2\epsilon_c} \tag{4.156}$$

Table 4.3: Analytical model results

	Temperature ($^{\circ}C$)	T	240	290	300
	Matrix shear modulus (Pa)	G_m	$7.61E{+}08$	$4.25E{+}08$	$1.86E{+}08$
Campbell model	Critical Strain	ϵ_c	$3.94E{-}03$	$2.20E{-}03$	$9.62E{-}04$
	Critical steering radius (mm)	r_c	1015.80	1818.89	4156.06
	Critical Wavelength (mm)	λ_c	0.1193	0.1597	0.2414
Wang model	Critical Strain	ϵ_c	$1.81E{-}02$	$1.01E{-}02$	$4.43E{-}03$
	Critical steering radius (mm)	r_c	220.74	395.25	903.12
	Critical Wavelength (mm)	λ_c	0.0510	0.0682	0.1031

The results of the analytical model calculated using a C program is shown in Table 4.3. To have a good agreement with the experimental measurements shown in Table 4.1 the analytical models should predict a critical steering radius between $1000mm$ and $800mm$ with a critical wavelength less than $3.13mm$. From the Table 4.3, at a temperature of $300^{\circ}C$, Wang's model predicts a critical steering steering radius of $903.12mm$ and a wavelength of $0.1031mm$ This satisfies the previously stated conditions to be in good agreement with the experimental results. From experimental observation it was seen that at a radius of $800mm$ only the fibers right at the inner-edge of the tape buckle, this indicates that the critical steering radius is likely closer to $800mm$. Of the two models, Wang's model provides a critical steering radius closer to $800mm$ making it more suitable for predicting the critical steering radius. The difference in results between the two models is because of the extra term $\left(\frac{d_f}{2c}\frac{du_y}{dx}\right)$ in the shear strain expression which occurs because of the influence of the surrounding fibers.

From experimental observation we know that the fiber buckling occurs right after the tape is consolidated on to the substrate by the roller, after which it experiences the bending strain applied by the AFP head at it follows the defined curved path. At this stage, the temperature will put the PEEK matrix in its rubbery state, close to the melting point. This is also reflected in the prediction using the Wang model where the critical steering radius is predicted to be $903.12mm$ at a temperature of $300^{\circ}C$ which is close to the melting point of PEEK at $343^{\circ}C$.

Another interesting observation from the analytical results is that the critical steering radius tends to decrease with decreasing temperature (See Table 4.3). Visual inspection

of the tapes that were steered at the higher speeds of $10.16-12.7cm/s(4-5in/s)$ indicate that this is true (See Section 3.5.1.2). Since the buckling observed at these speeds were much less when compared to lower speeds of $5.08-7.62cm/s(2-3in/s)$. It can be inferred that the critical steering radius at higher speeds is closer to $400mm$. Such a correlation can be made because the increase in laydown speed is, in effect, a decrease in the temperature of the tape. This means, by increasing the laydown speed one can steer at tighter radii with minimal steering induced defects. However, it must be kept in mind that a higher laydown speed can adversely affect the strength of the bond with the substrate.

4.8 Conclusion

In this chapter, first the mechanism by which fiber buckling occurs was discussed. Then, four models that could help mathematically define this mechanism were presented. Out of the four, the models of Campbell *et al.*, [68] and Wang *et al.*, [69] were adopted to predict the critical steering radius for a steered tape beyond which fiber buckling can be expected.

Using parameters that were measured from experimental samples or taken from literature, the critical steering radii was calculated for three different temperatures of $230°C$, $290°C$ and $300°C$. The Wang model predicted a critical steering radius of $903.12mm$ at a temperature of $300°C$, which falls squarely in the experimentally observed range of $1000-800mm$. The Wang model also showed a correlation between critical steering radius and the temperature ie., it predicted that as the temperature of the composite tape decreases, its critical steering radius will also decrease. This phenomenon was also observed experimentally. These results showed that the Wang model was more successful in predicting the critical steering radius. Thus, we were able to propose a suitable analytical model that can be used to easily predict the critical steering radius after which fiber buckling can be expected. Buckled fibers can decrease the stiffness and strength of a laminate. The results of this model will aid in the design of VAT laminates by helping the designer to anticipate the radius at which fiber buckling will occur.

Chapter 5

Conclusion

The objective of this thesis is *to investigate the ability of the Hot Gas Torch-assisted Automated Fiber Placement process to steer Carbon Fiber/PEEK composite prepreg tapes, and analytically predict the onset of fiber buckling.* To achieve the first part of this objective various experiments were conducted to evaluate the effects of different process parameters on fiber steering. The process parameters chosen to be evaluated were steering radius, laydown speed, number of repass and substrate angle. To understand the effects of these process parameters the samples prepared were evaluated using; 1. Visual inspection, 2. Geometrical analysis, 3. Microscopic analysis and 4. Mechanical testing

Visual inspection was performed for samples with different steering radii, laydown speed and number of repass. From this we found that defects such as fiber buckling begin from a steering radius of $800mm$ where very slight fiber buckling was found along the very edge of the steered tape. From the radius of $600mm$ fiber buckling was more clearly observable and at the radius of $400mm$ there were also some signs of minor tape folding. At the radius of $200mm$ it was found that the buckling and tape folding were quite severe. For samples with laydown speeds of $10.16cm/s$ and $12.7cm/s$ the fiber buckling was found to be intermittent and not continuous. Such a behaviour was likely due to the lower heat transfer from the HGT to the tape at higher speeds. This would mean that the viscosity of PEEK would be higher and it could provide better support to the fibers and prevent them from buckling continuously. Repass was performed on tapes steered at $600mm$,

400mm and 200mm radii. It was found that even a single repass can help smooth out some of the fiber buckling. Tape folding, however, could not be smoothed out and often resulted in the tape edge breaking. Multiple repasses did not have a marked difference on the quality of the steered tapes, thus, in most cases a single repass would be sufficient. Tape folding, however, could not be fixed by performing repass. In some cases, the folded edge of the tape was found to be broken by the repass. Optical microscopy complemented the visual observations and showed that the bond between the steered tape and substrate was very good until the radius of 400mm. For the tapes steered at 400mm and 200mm, there was a clear separation from the substrate at the edges and more voids at the bond line.

A specially devised mechanical test, inspired by the lap shear test, was proposed to fill the knowledge gap identified in the literature review regarding bond strength evaluation of steered tapes. The proposed test was then used to test the bond strength of the steered CF/PEEK tapes with a CF/PEEK substrate that was also manufactured by the HGT-assisted AFP. These tests were performed for samples with different steering radii, laydown speed and substrate angle. The test results indicate that bond strength of the steered tapes up to a radius of 400mm was as good as the straight tapes. However, at the radius of 200mm there was a sharp fall in the bond strength. The severe tape folding prevalent at this radius is believed to be the primary cause of this reduction in the bond strength. Another important observation was that the bond strength of AFP in-situ consolidated samples were roughly less than half those post consolidated in the autoclave.

It was also found that the bond strength decreases linearly with increasing laydown speed by testing four different laydown speeds at a steering radius of 400mm. The tapes steered at speeds of 10.16cm/s (4in/s) and 12.7cm/s (5in/s) showed poor bond strength despite having much lower steering induced defects. This highlighted the importance of choosing proper process parameters to allow sufficient heat transfer to take place to melt the thermoplastic resin completely and bond well with the substrate. The bond strength at higher speeds may be improved by using a higher gas flow rate or higher hot gas

temperature. The effect of substrate angle was also investigated and the results showed that the bonding was strongest at the substrate angle of 0° and weakest at 90°.

To analytically predict the onset of the fiber buckling, various analytical models that were derived from Timoshenko's *Bar on an elastic foundation* were studied and the most suitable models that drew a parallel with the problem of fiber buckling due to steering were adopted. These models considered a plane stress approach for the bending of an elastic memory composite and the in-plane fiber buckling caused by it. The steering a of CF/PEEK tape using a HGT-assisted AFP is essentially the bending of a plane (the tape) by external moments which causes the fibers along the inner-edge of the tape to buckle under compression. The models of Campbell *et al.*, [68] and Wang *et al.*, [69] were adopted to calculate the critical steering radius and wavelength were calculated. Of the two models, the model of Wang *et al.*, showed a closer agreement with the experimental observation by predicting a critical steering radius of $903mm$. Moreover, the Wang model also showed a trend of decreased critical steering radius with decreasing temperature.

From the various experiments we understand that the tapes can be steered up to a radius of $400mm$ without the bond strength being affected. The use of single repass to smooth out fiber buckling will prove helpful when VAT laminates are manufactured using this process, as buckled fibers can reduce the stiffness of such laminates. This work also showed the effect of substrate angle on the steered tape, this is very important because fiber steering cannot be performed without the substrate angle varying. The effect on laydown speed on tapes is well known and this work also verified that and highlighted the need to choose the right process parameters so that there is adequate heat transfer to the CF/PEEK tape. Finally, a simple analytical technique was shown to predict the onset of fiber buckling with good correlation with experimental results.

5.1 Contributions

This thesis provides a solid first step in understanding the ability of the Hot Gas Torch-assisted Automated Fiber Placement process to steer CF/PEEK tapes. Its main contri-

butions include,

- Studying the effects of different AFP parameters on steering of thermoplastic composite tape.
- Developing a new mechanical test to study the bond strength of a steered tape with its substrate.
- Analytically predicting the critical buckling radius using available models and finding it to be in good correlation with experimental results.

5.2 Future Work

This work dealt only with single steered tapes and the defects that occur in these tapes due to fiber steering. Future work will involve building on this understanding and expanding it to be used with VAT laminates. There are other steering induced defects such as, gaps and overlaps, that need to be studied to gain a complete understanding of fiber steering using HGT-assisted AFP process. With this understanding, VAT laminates can be designed and tested for various applications like reducing stress concentration, tailoring stiffness along the stress field etc.

References

1. Lewis, A. Making Composite Repairs to the 787. **Aero Quarterly,** 05–14. https://www.boeing.com/commercial/aeromagazine/articles/2015_q1/archive.html (2014).

2. Hale, J. Boeing 787 from the Ground Up. **Aero Quarterly,** 17–24. https://www.boeing.com/commercial/aeromagazine/articles/qtr_4_06/index.html (2006).

3. Hyer, M. W. *Stress Analysis of Fiber-reinforced Composite Materials* 718 pp. (DEStech Publications, Inc, 2009).

4. Setoodeh, S., Gürdal, Z. & Watson, L. T. Design of variable-stiffness composite layers using cellular automata. *Computer Methods in Applied Mechanics and Engineering* **195,** 836–851. http://www.sciencedirect.com/science/article/pii/S0045782505001325 (Feb. 1, 2006).

5. Gürdal, Z., Tatting, B. F. & Wu, C. K. Variable stiffness composite panels: Effects of stiffness variation on the in-plane and buckling response. *Composites Part A: Applied Science and Manufacturing* **39,** 911–922. http://www.sciencedirect.com/science/article/pii/S1359835X07002643 (May 1, 2008).

6. Lopes, C. S., Gürdal, Z. & Camanho, P. P. Variable-stiffness composite panels: Buckling and first-ply failure improvements over straight-fibre laminates. *Computers & Structures. Composites* **86,** 897–907. http://www.sciencedirect.com/science/article/pii/S0045794907001654 (May 1, 2008).

7. Rouhi, M., Ghayoor, H., Hoa, S. V., Hojjati, M. & Weaver, P. M. Stiffness tailoring of elliptical composite cylinders for axial buckling performance. *Composite Structures* **150,** 115–123. http://www.sciencedirect.com/science/article/pii/S0263822316304639 (Aug. 15, 2016).

8. Wu, K. *et al. Design and Manufacturing of Tow-Steered Composite Shells Using Fiber Placement* in *50th AIAA/ASME/ASCE/AHS/ASC Structures, Structural Dynamics, and Materials Conference* 50th AIAA/ASME/ASCE/AHS/ASC Structures, Structural Dynamics, and Materials Conference (American Institute of Aeronautics and Astronautics, Palm Springs, California, May 4, 2009). http://arc.aiaa.org/doi/10.2514/6.2009-2700.

9. Clancy, G. *et al.* A study of the influence of processing parameters on steering of carbon Fibre/PEEK tapes using laser-assisted tape placement. *Composites Part B: Engineering* **163,** 243–251. https://linkinghub.elsevier.com/retrieve/pii/S135983681832300X (Apr. 2019).

10. Blom, A. W. *Structural Performance of Fiber-Placed, Variable-Stiffness Composite Conical and Cylindrical Shells* PhD thesis (2010). https://repository.tudelft.nl/islandora/object/uuid%3A46f2e44b-1a68-44f8-9633-79490a54e087.

11. Marouene, A., Boukhili, R., Chen, J. & Yousefpour, A. Effects of gaps and overlaps on the buckling behavior of an optimally designed variable-stiffness composite laminates – A numerical and experimental study. *Composite Structures* **140,** 556–566. https://www.sciencedirect.com/science/article/pii/S0263822316000258 (Apr. 15, 2016).

12. Croft, K. *et al.* Experimental study of the effect of automated fiber placement induced defects on performance of composite laminates. *Composites Part A: Applied Science and Manufacturing* **42,** 484–491. https://www.sciencedirect.com/science/article/pii/S1359835X11000224 (May 1, 2011).

13. Woigk, W. *et al.* Experimental investigation of the effect of defects in Automated Fibre Placement produced composite laminates. *Composite Structures* **201,** 1004–

1017. https://www.sciencedirect.com/science/article/pii/S0263822317339946 (Oct. 1, 2018).

14. Bakhshi, N. & Hojjati, M. An experimental and simulative study on the defects appeared during tow steering in automated fiber placement. *Composites Part A: Applied Science and Manufacturing* **113,** 122–131. https://www.sciencedirect.com/science/article/pii/S1359835X1830280X (Oct. 1, 2018).

15. Peeters, D. M. J. *Design Optimisation of Practical Variable Stiffness and Thickness Laminates* PhD thesis (2017). https://repository.tudelft.nl/islandora/object/uuid%3Aa07ea6a4-be73-42a6-89b5-e92d99bb6256.

16. Lamontia, M. A. *et al.* Manufacturing flat and cylindrical laminates and built up structure using automated thermoplastic tape laying, fiber placement, and filament winding. *Sampe Journal* **39,** 30–43 (2003).

17. Timoshenko, S. P. & Gere, J. M. *Theory of Elastic Stability* 562 pp. (Courier Corporation, June 22, 2009).

18. Hoa, S. V. *Principles of the manufacturing of composite materials* Second edition. 437 pp. (DEStech Publications, Inc, Lancaster, Pennsylvania, 2018).

19. MTorres. *Automatic taping machine - TORRESLAYUP* https://mtorres.es/en/equipment/manufacturing-systems/lamination/automatic-wrapping-machine-torreslayup.

20. MTorres. *Automatic Fiberplacement Machine - TORRESFIBERLAYUP* https://mtorres.es/en/equipment/manufacturing-systems/lamination/automatic-machine-of-fiberplacement-torresfiberlayup.

21. Moddeman, W. E., Bowling, W. C., Tibbitts, E. E. & Whitaker, R. B. Thermal stability and compatibility of polyetheretherketone (PEEK) with an oxidizer and pyrotechnic blend. *Polymer Engineering & Science* **26,** 1469–1477. https://onlinelibrary.wiley.com/doi/abs/10.1002/pen.760262102 (1986).

22. Day, M., Cooney, J. D. & Wiles, D. M. The thermal stability of poly(aryl-ether–ether-ketone) as assessed by thermogravimetry. *Journal of Applied Polymer Science* **38,** 323–337. https://onlinelibrary.wiley.com/doi/abs/10.1002/app.1989.070380214 (1989).

23. Cai, X. *Determination of Process Parameters for the Manufacturing of Thermoplastic Composite Cones Using Automated Fiber Placement* masters (Concordia University, June 18, 2012). 105 pp. https://spectrum.library.concordia.ca/id/eprint/974158/.

24. Zacchia, T. T., Shadmehri, F., Fortin-Simpson, J. & Hoa, S. V. Design Of Hard Compaction Rollers For Automated Fiber Placement On Complex Mandrel Geometries. https://yorkspace.library.yorku.ca/xmlui/handle/10315/35245.

25. IJsselmuiden, S. T. *Optimal Design of Variable Stiffness Composite Structures using Lamination Parameters* PhD thesis (2011). https://repository.tudelft.nl/islandora/object/uuid%3A973a564b-5734-42c4-a67c-1044f1e25f1c.

26. Weaver, P., Potter, K., Hazra, K., Saverymuthapulle, M. & Hawthorne, M. *Buckling of Variable Angle Tow Plates: From Concept to Experiment* in *50th AIAA/ASME/ASCE/AHS/ASC Structures, Structural Dynamics, and Materials Conference* 50th AIAA/ASME/ASCE/AHS/ASC Structures, Structural Dynamics, and Materials Conference (American Institute of Aeronautics and Astronautics, Palm Springs, California, May 4, 2009). http://arc.aiaa.org/doi/10.2514/6.2009-2509.

27. Bakhshi, N. *Process-Induced Defects during Tow Steering in Automated Fiber Placement: Experiment, Modeling and Simulation* masters (Concordia University, Nov. 27, 2018). 153 pp. https://spectrum.library.concordia.ca/984730/.

28. Rajan, G. & Prusty, B. G. *Structural Health Monitoring of Composite Structures Using Fiber Optic Methods* 508 pp. (CRC Press, Oct. 3, 2016).

29. Kim, B. C., Hazra, K., Weaver, P. & Potter, K. *Limitations of fibre placement techniques for variable angle tow composites and their process-induced defects* in *Pro-*

ceedings of the 18th International Conference on Composite Materials (ICMM18), Jeju, Korea (2011), 21–26.

30. Kim, B. C., Potter, K. & Weaver, P. M. Continuous tow shearing for manufacturing variable angle tow composites. *Composites Part A: Applied Science and Manufacturing* **43,** 1347–1356. http://www.sciencedirect.com/science/article/pii/S1359835X12000929 (Aug. 1, 2012).

31. Stokes-Griffin, C. *A combined optical-thermal model for laser-assisted fibre placement of thermoplastic composite materials* PhD thesis (2015). https://openresearch-repository.anu.edu.au/handle/1885/150750.

32. *Mechanical testing of advanced fibre composites* (ed Hodgkinson, J. M.) (CRC Press ; Woodhead, Boca Raton, FL : Cambridge, England, 2000). 362 pp.

33. ASTM D30 Committee. *Test Method for Mixed Mode I-Mode II Interlaminar Fracture Toughness of Unidirectional Fiber Reinforced Polymer Matrix Composites* (ASTM International). http://www.astm.org/cgi-bin/resolver.cgi?D6671D6671M-19.

34. ASTM D30 Committee. *Test Method for Mode I Interlaminar Fracture Toughness of Unidirectional Fiber-Reinforced Polymer Matrix Composites* (ASTM International). http://www.astm.org/cgi-bin/resolver.cgi?D5528-13.

35. Bhashyam, S. & Davidson, B. D. Evaluation of Data Reduction Methods. *AIAA Journal* **35,** 546–552. https://doi.org/10.2514/2.129 (1997).

36. RUSSEL, A. J. Factors Affecting the Interlaminar Fracture Energy of Graphite/Epoxy Laminates. *Proc. 4th Int. Conf. on Composite Materials,* 279–286. https://ci.nii.ac.jp/naid/10007205992/ (1982).

37. Nicholls, D. & Gallagher, J. Determination of GIC in Angle Ply Composites Using a Cantilever Beam Test Method. *Journal of Reinforced Plastics and Composites* **2,** 2–17. https://doi.org/10.1177/073168448300200101 (Jan. 1, 1983).

38. Chai, H. The characterization of Mode I delamination failure in non-woven, multidirectional laminates. *Composites* **15,** 277–290. https://www.sciencedirect.com/science/article/pii/0010436184907080 (Oct. 1, 1984).

39. Bradley, W. L., Corleto, C. R. & Goetz, D. P. *Fracture Physics of Delamination of Composite Materials.* (Texas A&M University, college station mechanics and materials center, Oct. 1, 1987). https://apps.dtic.mil/sti/citations/ADA192021.

40. Laksimi, A., Benzeggagh, M. L., Jing, G., Hecini, M. & Roelandt, J. M. Mode I interlaminar fracture of symmetrical cross-ply composites. *Composites Science and Technology* **41,** 147–164. https://www.sciencedirect.com/science/article/pii/026635389190025K (Jan. 1, 1991).

41. Robinson, P. & Song, D. A Modified DCB Specimen for Mode I Testing of Multidirectional Laminates. *Journal of Composite Materials* **26,** 1554–1577. https://doi.org/10.1177/002199839202601101 (Nov. 1, 1992).

42. Foster, S., Robinson, P. & Hodgkinson, J. Interlaminar fracture toughness testing of $0/\theta$ interfaces in carbon-epoxy laminates using edge delamination strategy. *Plastics rubber and composites processing and applications* **26,** 430–437 (1997).

43. Hiley, M. J. in *European Structural Integrity Society* (eds Williams, J. G. & Pavan, A.) 61–72 (Elsevier, Jan. 1, 2000). https://www.sciencedirect.com/science/article/pii/S1566136900800084.

44. Kim, B. W. & Mayer, A. H. Influence of fiber direction and mixed-mode ratio on delamination fracture toughness of carbon/epoxy laminates. *Composites Science and Technology* **63,** 695–713. http://www.sciencedirect.com/science/article/pii/S0266353802002580 (Apr. 1, 2003).

45. *Delamination behaviour of composites* (ed Sridharan, S.) (Woodhead Pub, Cambridge, 2008). 1 p.

46. De Gracia, J., Boyano, A., Arrese, A. & Mujika, F. Analysis of DCB test of angle-ply laminates including bending-twisting coupling. *Composite Structures* **190,** 169–178. http://www.sciencedirect.com/science/article/pii/S026382231733622X (Apr. 15, 2018).

47. Belhaj, M. M. *Theoretical and Experimental Investigation of out-of-plane Wrinkle Formation during Steering in Automated Fiber Placement* PhD thesis (Concordia University, Nov. 23, 2020). 112 pp. https://spectrum.library.concordia.ca/id/eprint/987975/.

48. De Freitas, S. T. & Sinke, J. Test method to assess interface adhesion in composite bonding. *Applied Adhesion Science* **3,** 9. https://doi.org/10.1186/s40563-015-0033-5 (Mar. 24, 2015).

49. ASTM D14 Committee. *Test Method for 90 Degree Peel Resistance of Adhesives* (ASTM International). http://www.astm.org/cgi-bin/resolver.cgi?D6862-11R16.

50. ASTM D14 Committee. *Test Method for Peel Resistance of Adhesives (T-Peel Test)* (ASTM International). http://www.astm.org/cgi-bin/resolver.cgi?D1876-08R15E1.

51. ASTM D14 Committee. *Test Method for Lap Shear Adhesion for Fiber Reinforced Plastic (FRP) Bonding* (ASTM International). http://www.astm.org/cgi-bin/resolver.cgi?D5868-01R14.

52. Imada. *90 Degree Peel Tester - Imada Inc.* https://imada.com/products/90-degree-peel-tester/.

53. De Freitas, S. T. & Sinke, J. Adhesion Properties of Bonded Composite-to-Aluminium Joints Using Peel Tests. *The Journal of Adhesion* **90,** 511–525. https://doi.org/10.1080/00218464.2013.850424 (June 3, 2014).

54. Hulcher, A. B., Marchello, J. M. & Hinkley, J. A. Wedge peel testing for Automated fiber placement. *Wedge peel testing for Automated fiber placement* **31,** 37–43 (1999).

55. Comer, A. *et al.* Wedge peel interlaminar toughness of Carbon-Fibre/PEEK thermoplastic laminates manufactured by laser-assisted automated-tape-placement (LATP). http://rgdoi.net/10.13140/2.1.1305.9847 (2014).

56. Khan, M. A. Experimental and Simulative Description of the Thermoplastic Tape Placement Process with Online Consolidation. `https://kluedo.ub.uni-kl.de/frontdoor/index/index/docId/4729` (2010).

57. International, A. *ASTM D2344-16: Standard Test Method for Short-Beam Strength of Polymer Matrix Composite Materials* (ASTM, 2016).

58. D3846-02, A. s. *Standard Test Method for In-Plane Shear Strength of Reinforced Plastics* (ASTM West Conshohocken, PA., 2002).

59. Qureshi, Z., Swait, T., Scaife, R. & El-Dessouky, H. M. In situ consolidation of thermoplastic prepreg tape using automated tape placement technology: Potential and possibilities. *Composites Part B: Engineering* **66,** 255–267. `http://www.sciencedirect.com/science/article/pii/S1359836814002388` (Nov. 1, 2014).

60. Rajasekaran, A. & Shadmehri, F. Steering of carbon fiber/PEEK tapes using Hot Gas Torch-assisted automated fiber placement. *Journal of Thermoplastic Composite Materials,* 08927057211067962. `https://doi.org/10.1177/08927057211067962` (Feb. 14, 2022).

61. Shadmehri, F., Hoa, S. V., Fortin-Simpson, J. & Ghayoor, H. Effect of in situ treatment on the quality of flat thermoplastic composite plates made by automated fiber placement (AFP). *Advanced Manufacturing: Polymer & Composites Science* **4,** 41–47. `https://doi.org/10.1080/20550340.2018.1444535` (Apr. 3, 2018).

62. Hoang, M. D. *Procedure for making flat thermoplastic composite plates by Automated Fiber Placement and their mechanical properties* masters (Concordia University, Apr. 2015). 82 pp. `https://spectrum.library.concordia.ca/979994/`.

63. Aghababaei Tafreshi, O. *Heat Transfer Study of the In-situ Automated Fiber Placement (AFP) for Thermoplastic Composites* masters (Concordia University, Dec. 1, 2019). 146 pp. `https://spectrum.library.concordia.ca/id/eprint/986269/`.

64. Rajasekaran, A. & Shadmehri, F. Modified Lap Shear Test for Automated Fiber Placement (AFP) of Steered Thermoplastic Composite Tape. *Proceedings of the*

American Society for Composites — Thirty-fifth Technical Conference **0.** https://www.dpi-proceedings.com/index.php/asc35/article/view/34869 (2020).

65. Lawal, A. & Kalyon, D. M. Squeezing flow of viscoplastic fluids subject to wall slip. *Polymer Engineering & Science* **38,** 1793–1804 (1998).

66. Grefe, H., Kandula, M. W. & Dilger, K. Influence of the fibre orientation on the lap shear strength and fracture behaviour of adhesively bonded composite metal joints at high strain rates. *International Journal of Adhesion and Adhesives. Special issue on Joint design* **97,** 102486. https://www.sciencedirect.com/science/article/pii/S0143749619302350 (Mar. 1, 2020).

67. Dow, N. F. & Rosen, B. W. *Evaluations of Filament-Reinforced Composites for Aerospace Structural Applications.* (GENERAL ELECTRIC CO PHILADELPHIA PA, 1965).

68. Campbell, D., Mallick, K. & Lake, M. in *45th AIAA/ASME/ASCE/AHS/ASC Structures, Structural Dynamics & Materials Conference* (American Institute of Aeronautics and Astronautics). https://arc.aiaa.org/doi/abs/10.2514/6.2004-1636.

69. Wang, Z. D., Li, Z. F. & Wang, Y. S. Microbuckling Solution of Elastic Memory Laminates under Bending: *Journal of Intelligent Material Systems and Structures.* https://journals-sagepub-com.lib-ezproxy.concordia.ca/doi/10.1177/1045389X09102558 (June 12, 2009).

70. Timoshenko, S. 1.-1. *Strength of materials* Third edition. (D. Van Nostrand Company, New York, 1955).

71. Cogswell, F. N. *Thermoplastic Aromatic Polymer Composites: A Study of the Structure, Processing and Properties of Carbon Fibre Reinforced Polyetheretherketone and Related Materials* 288 pp. (Elsevier, Oct. 22, 2013).

Appendix A

Appendix

The following is a C++ program used to calculate the critical strain, critical radius and wavelength using the Campbell and Wang fourmulations. The parameters used here have been shown in Table 4.2. The calculations are repeated for three different temperatures using a for loop.

A.1 Analytical.c

```
#include <stdio.h>
#include <math.h>
#include <gsl/gsl_math.h>

int main()
{
  //All variables are in SI units: Pa, m etc.
  //Constant Declarations
  //Taking G_m values for 232, 288 and 315C respectively.
  const double G_m[3] = {7.61*pow(10.0,8.0), 4.25*pow(10.0,8.0), 1.86*
   pow(10.0,8.0)};
  const int T[3] = {240, 290, 300};
  //const double V_f = 0.616344198; //Volumetric fraction of fiber -
   calculated from micrographs
  const double V_f = 0.63;
```

```
14  const double V_m = 1.0 - V_f; //Volumetric fraction of matrix
15  const double E_f = 2.27 * pow(10.0,11.0); //Young's Modulus of fiber
     in Pa obtained form data sheet fot AS4 carbon fiber
16  //const double d_f = 6.742 * pow(10.0,-6.0); //Diameter of fiber in m
      - Calculated from micrographs
17  const double d_f = 6.74 * pow(10.0,-6.0); //Diameter of fiber in m -
     Calculated from micrographs
18  const double c = ((d_f/V_f) - d_f)/2; //from the definition of V_f
     for a unit cell
19  const double h = 0.008; //Width of steered tape in m
20
21  //Variable Declarations
22  double strain = 0;
23  double strain_w = 0;
24  double r = 0; //Steering radius or radius of curvature
25  double r_w = 0; //Steering radius or radius of curvature
26  double wlen = 0; //Wavelength of buckled fibers
27  double wlen_w = 0; //Wavelength of buckled fibers
28
29  printf("Temperature(C) \tMatrix shear mod(Pa) \tCampbell Wavelength(
     mm) \tCampbell Radius(mm) \tWang Wavelength(mm) \tWang Radius(mm)\n"
     );
30  for (int i=0; i<3 ; i++)
31    {
32      //Campbell's formulation
33      strain = ( 2 * G_m[i] * V_m ) / (E_f * V_f);
34      r = h / (2 * strain);
35      //Re-derived Campbell wavelength for hex packed, it turns out to
     be the same as square packed
36      wlen = ( (M_PI*d_f)/(4) ) * sqrt( (E_f * V_f)/(G_m[i] * V_m) );
37
38      //Wang's formulation
39      wlen_w = sqrt( (pow(M_PI,2) * pow(V_m,2) * E_f * pow(d_f,3)) /
     (24 * c * G_m[i]) );
40      strain_w = (2 * G_m[i]) / (V_m * E_f) ;
```

```
41        r_w = h / (2 * strain_w);
42
43        //Printing results
44        printf("%d\t\t%.3e\t\t%.3f\t\t\t\t%.3f\t\t%.3f\t\t\t%.3f\n",T[i],
    G_m[i],wlen*1000,r*1000,wlen_w*1000,r_w*1000);
45     }
46
47 return 0;
48 }
```